METALLIC NANOSTRUCTURES AND PLASMONIC DEVICES FOR SURFACE PLASMON RESONANCE BIOSENSING

A DISSERTATION

SUBMITTED TO THE FACULTY OF THE GRADUATE SCHOOL

OF THE UNIVERSITY OF MINNESOTA

BY

HYUNGSOON IM

IN PARTIAL FULFILLMENT OF THE REQUIREMENTS

FOR THE DEGREE OF

DOCTOR OF PHILOSOPHY

PROF. SANG-HYUN OH, ADVISOR

AUGUST, 2011

Acknowledgements

I would like to thank my advisor, Professor Sang-Hyun Oh, for his guidance in my research with insight during my Ph.D study. I am grateful for having the opportunity to work on several different research projects with many talented collaborators and am deeply satisfied with the research experience I have obtained in his lab.

I would also like to thank all the current and former members of the Oh group for their support during the past years. First, I'd like to thank Antoine Lesuffleur and Nate Lindquist. As the first members in this group, we have supported each other for conducting much of our initial work and published several papers together. Also as the best friends of mine, I have enjoyed the time we have shared together. I wish to thank Nate Wittenberg for his endless support on several biosensing projects and many things that I have learned from him. Other group members, Si-Hoon Lee, Tim Johnson, Xiaoshu Chen, Luke Jordan, Shailabh Kumar, Jincy Jose, Sudhir Cherukulappurath, as well as my young REU students have earned my gratitude and I believe they will lead the Oh group to a world-class research lab.

I would like to also thank my committee members of my dissertation, Professors Stephen Campbell, Christy Haynes, Jian-Ping Wang and their group members Min-woo Jang, Sangho Song, Kyle Bantz, Audrey Meyer, Donghyuk Kim, and Yuanpeng Li. I should also thank many collaborators, Dr. Moses Rodriguez and Dr. Arthur Warrington at Mayo clinic, Professor Jennifer Maynard and her group members, Jennifer Sutherland and Jen Pai at the University of Texas, Austin, Professor David Norris and his students

Prashant Nagpal, William Tisdale, Jong-Hyuk Park, and Sriharsha Jayanti, and Dr. Mattew Pelton at the Argonne national lab. My research presented in this dissertation could not be achieved without the help and support of these many collaborators. My gratitude also extends to the helpful staffs at nanofabrication center and characterizing facility at the University of Minnesota for their support.

I thank many good friends I met here, Gichul Chun, Jaehoon Chung, Sangho Kim, Seongmin Sohn, Jaehyuk Kim, Boram Lee and many others. I also wish to thank Professor Yang-Kyu Choi and NOBELAB members, and Professor Eui-Sik Yoon and IML members. Their guidance during my bachelor and master study have made me possible to finish my PhD research successfully.

At the end, I would like to thank my wife, Joomi, who deserves very special thanks for her patience, support and understanding during the years of my study.

Dedication

This dissertation is dedicated to my wife, Joo Mi, for her love and support during my study.

Metallic Nanostructures and Plasmonic Devices
for Surface Plasmon Resonance Biosensing
by Hyungssoon Im

Abstract

High-throughput real-time sensing of molecular binding kinetics is important for drug discovery, basic biology, and the emerging field of proteomics. In particular, label-free *surface plasmon resonance* (SPR) sensing, which harnesses electromagnetic surface waves excited on metallic nanostructures, has been widely used in pharmaceutical development. Despite successful commercialization, the reflection-based configuration of traditional SPR instruments suffer from high cost, low sensing throughput, and incompatibility of studying molecules in cell membranes. In this dissertation, a new SPR biosensor based on plasmonic nanohole arrays made in metallic films is demonstrated. These biosensors are used for multiplexed sensing of molecular interactions in a quantitative manner. The nanohole-based SPR devices measure transmission of normally-incident light and the co-linear optical transmission setup offers simple optical setup and high-resolution imaging capability, leading to high-throughput multiplex kinetic assays for protein microarray applications. Additionally, the nanoholes can readily incorporate lipid membranes to study antibody binding to lipids and membrane-bound proteins. Newly developed nanofabrication methods enable production of large-area nanohole- and nanogap arrays in an inexpensive and high-throughput fashion. These methods may facilitate wide dissemination of nanohole SPR sensing as well as chemical sensing *via surface-enhanced Raman spectroscopy* (SERS) for biomedical applications.

Contents

List of Tables

List of Figures

List of Publications

1. N. J. Wittenberg, H. Im, T. W. Johnson, X. Xu, A. E. Warrington, M. Rodriguez, and S. H. Oh, "Facile assembly of micro- and nanoarrays for sensing with natural cell membranes." *ACS Nano*, *Article ASAP* **DOI:** 10.1021/nn202554t

2. H. Im, S. H. Lee, N. J. Wittenberg, T. W. Johnson, N. C. Lindquist, P. Nagpal, D. J. Norris, and S. H. Oh, "Template-stripped smooth Ag nanohole arrays with silica shells for surface plasmon resonance biosensing." *ACS Nano* **5**, 6244–6253 (2011)

3. K. C. Bantz, A. F. Meyer, N. J. Wittenberg, H. Im, O. Kurtulus, S. H. Lee, N. C. Lindquist, S. H. Oh, and C. L. Haynes, "Recent progress in SERS for biosensing." *Physical Chemistry Chemical Physics* **13**, 11551–11567 (2011)

4. H. Im, N. J. Wittenberg, A. Lesuffleur, N. C. Lindquist, and S. H. Oh, "Membrane protein biosensing with plasmonic nanopore arrays and pore-spanning lipid membranes." *Chemical Science* **1**, 688–696 (2010)

5. H. Im, K. C. Bantz, N. C. Lindquist, C. L. Haynes, and S. H. Oh, "Vertically oriented sub-10 nm plasmonic nanogap arrays." *Nano Letter* **10**, 2231–2236 (2010)

6. H. Im, N. C. Lindquist, A. Lesuffleur, and S. H. Oh, "Atomic layer deposition of dielectric overlayers for enhancing light transmission and chemical stability of plasmonic nanoholes." *ACS Nano* **4**, 947–954 (2010)

7. M. Mansuripur, A. R. Zakharian, A. Lesuffleur, S. H. Oh, R. J. Jones, N. C. Lindquist, H. Im, A. Kobyakov, and J. V. Moloney, "Plasmonic nano-structures for optical data storage" *Optics Express* **17**, 14001–14014 (2009)

8. H. Im, A. Lesuffleur, N. C. Lindquist, and S. H. Oh, "Plasmonic nanoholes in a multi-channel microarray format for parallel kinetic assays and differential sensing." *Analytical Chemistry* **81**, 2854–2859 (2009)

9. N. C. Lindquist, A. Lesuffleur, H. Im, and S. H. Oh, "Sub-micron resolution surface plasmon resonance imaging enabled by nanohole arrays with surrounding bragg mirrors for enhanced sensitivity and isolation." *Lab on a Chip* **9**, 382–387 (2009)

10. A. Lesuffleur, H. Im, N. C. Lindquist, K. S. Lim, and S. H. Oh, "Laser-illuminated nanohole arrays as a multiplex plasmonic microarray sensor." *Optics Express* **16**, 219–224 (2008)

11. A. Lesuffleur, H. Im, N. C. Lindquist, and S. H. Oh, "Periodic nanohole arrays with shape-enhanced plasmon resonance as real-time biosensors." *Applied Physics Letter* **91**, 243110 (2007)

Chapter 1

Introduction

With continuous growth the life science and healthcare segments make up a large proportion of recent research in science and technology. Recent advances in nano- and bionanotechnology have lead to rapidly growing multidisciplinary research in *biosensors*, which detects and recognizes specific biomaterials. Biosensors can provide crucial information to significantly improve, diagnosis and treatment of many diseases. Developing faster, cheaper, and more efficient biosensing technology is of great importance for both researchers and patients. For researchers working in the life sciences or clinical research, it is crucial to bring new drugs to the market faster. Therefore, development of new techniques that can accelerate the drug candidate screening process is highly desired. For patients, inexpensive point-of-care diagnostic devices could provide the opportunity to self-monitor their conditions without visiting the clinic frequently. Developing new biosensors that fulfill specific needs of both researchers and customers in the market would be a significant advance in biomedical research. In this dissertation, new strategies are demonstrated to make nanostructured materials and biosensors for high-throughput screening. This work has mainly focused on affinity biosensors that can measure binding kinetics of molecular interactions in a real-time, label-free manner. Precise measurements of binding rates and affinities of molecular systems are essential

for determining the potency of a drug molecule and the required dose for therapeutic action. The nanostructures and devices described in this thesis are miniaturized into a densely packed microarray of sensing elements for high-throughput screening similar to existing DNA or protein microarrays, which were developed for studying thousands of protein-protein interactions simultaneously in a "lab-on-a-chip" system.[1] Among various detection schemes based on electrical, mechanical, or optical methods, this work focuses on optical detection methods, which is highly sensitive, non-destructive, and nearly unlimited in types of detectable molecules. In particular, surface plasmon resonance (SPR) devices, which utilize electromagnetic surface waves generated by metallic nanostructures, are attractive because of their high sensitivity and label-free, real-time detection capabilities. In this dissertation, a new type of SPR biosensor based on nanohole arrays made in metallic films is demonstrated for multiplex sensing of molecular binding interactions. Key advantages of the new SPR sensor based on metallic nanoholes include studying membrane-associated molecules in a platform that mimics natural cell membranes. Novel nanofabrication methods are also presented to produce nanohole- and nanogap-based SPR sensors in an inexpensive and high-throughput fashion for wide dissemination of SPR sensing for biomedical research and applications.

1.1 Optical Biosensing

Molecular interactions can be detected by monitoring parameters such as electrical, magnetic, electrochemical, mechanical, or optical properties. Among these methods, optical detection has been widely used in biomedical research. Optical detection methods are sensitive, non-destructive, simple, and less limited in types of molecules that can be detected than other biosensing methods. Fluorescence microscopy[2] and enzyme-linked immonusorbent assays (ELISA)[3] are core optical techniques that can detect molecular interactions because of their high sensitivity and accuracy. There is, however, a critical disadvantage in these optical methods — a labeling or additional reaction steps

are required to detect the sensing signal. This labeling requirement often necessitates development of specific chemistry to attach a dye or linker to a target molecule without causing adverse effects. This difficulty leads to a demand for a label-free optical biosensing system, which can directly measure molecular interactions with a similar level of efficiency, sensitivity, and accuracy.

1.1.1 Surface plasmon resonance biosensing

Surface plasmons (SPs) are collective oscillations of free electrons in metals excited by an external electromagnetic field, *i.e.* light.[4] Because the SPs can be tightly confined at the interface between a metal and a surrounding medium, it is very sensitive to local changes including the presence of molecules on the surface. *Surface plasmon resonance* (SPR) sensors utilize this property of SPs to detect molecular binding to target molecules immobilized on the sensing surface.[5] SPR sensors are able to directly detect the molecualr binding event without any labeling process and provide crucial information of molecular binding interactions

1.1.2 The limit of current technology

The real-time, label-free sensing capability of SPR sensors has lead to successful commercialization of the SPR instruments, which are now widely used in pharmaceutical development, proteomics, and basic research.[6,7] Despite successful commercialization, conventional SPR instruments are bulky in size, very expensive ($>$ \$200,000), low throughput, and cannot easily incorporate membrane-bound proteins. Therefore, it is desirable to develop new SPR instruments that can overcome these limitations and provide unique features that cannot be incorporated into conventional SPR instruments.

1.2 Scope of the Dissertation

Research presented in this dissertation focuses on the development of new surface plasmon resonance (SPR) devices and nanostructured materials that can overcome the limits of conventional SPR techniques and open up new avenues of real-time, label-free kinetic biosensing. A large portion of this dissertation is about SPR biosensing with plasmonic nanohole arrays. The plasmonic nanohole array utilizes the *extraordinary optical transmission* (EOT) effect through an array of sub-wavelength sized nanoholes in metallic films. Molecular binding to the nanohole array induces changes in the optical properties of the sensing surface, leading to a shift in the transmission spectrum. Real-time, label-free kinetic sensing is possible by tracking the spectral shift due to the molecular binding as a function of time. Compared to conventional SPR instruments, nanohole-based SPR sensors can provide unique advantages for high-resolution, high-throughput multiplexed molecular sensing. Furthermore, they can enable studies of molecular interactions on lipid membranes that mimic natural cell membranes. New high-throughput fabrication methods are developed for inexpensive, but high quality SPR devices with improved sensitivity for both SPR real-time sensing and *surface-enhanced Raman spectroscopy* (SERS). SERS is used to detect and identify molecules on nanostructured surfaces. Additionally, future directions with preliminary results are presented.

1.2.1 Outline of chapters

This dissertation is organized into following chapters and each chapter outlines original research performed during the course of graduate study.

- **Chapter 2** describes background theory of *surface plasmon resonance* (SPR) and the effect of *extraordinary optical transmission* (EOT) through a periodic nanohole array made in metallic films. In addition, strategies for analysis of molecular binding kinetics to obtain binding rates and affinities are presented.

- **Chapter 3** describes the sensing principle of conventional SPR instruments along with limits of traditional SPR techniques. Additionally, fabrication of a new SPR sensor based on a plasmonic nanohole array as well as its label-free real-time sensing capability is demonstrated.

- **Chapter 4** presents a SPR imaging technique that is designed for high-resolution, high-throughput sensing of multiple binding kinetics simultaneously. Using the SPR imaging, multiplex and differential sensing for various concentrations of streptavidin binding to biotin immobilized on the sensing surface is demonstrated. Additionally, the potential use of the SPR imaging with densely packed nanohole arrays for protein microarray is presented.

- **Chapter 5** presents integration of plasmonic nanopore arrays with lipid membranes, major components in cell membranes. Because proteins residing in the lipid membranes mediate many important cellular activities, studying antibody binding to those membrane-bound proteins and receptors is of great importance in new drug discovery. Label-free measurements of binding kinetics of antibodies to surface antigens and transmembrane proteins incorporated in supported and suspended lipid membranes are demonstrated.

- **Chapter 6** presents strategies to improve the sensitivity of the plasmonic nanohole arrays and to fabricate them in a low-cost, high-throughput manner for wide dissemination of the platform to other researchers. It is also demonstrated a new fabrication method, called template stripping, allows producing high-quality plasmonic nanostructures from simple deposition and peeling off processes without using expensive lithography tools.

- **Chapter 7** describes another useful sensing technique, *surface-enhanced Raman spectroscopy* (SERS), which can identify molecules. With the introduction of widely used SERS substrates and fabrication methods, a new fabrication method

designed for producing sub-10-nm nanogap arrays with precise control of gap's size, shape, position, and orientation is demonstrated. Additionally, a strategy to fabricate the nanogap arrays in a large area inexpensively is presented.

- **Chapter 8** summarizes the research works presented in the dissertation and suggests the direction of on-going and future research along with preliminary data.

Chapter 2

Background Theory

In this chapter, fundamental theories of surface plasmon resonance (SPR) and the extraordinary optical transmission (EOT) effect are described. Also methods to analyze molecular binding kinetics to determine kinetic parameters, binding rates and binding affinity, are described.

2.1 Surface Plasmon Resonance

SPs are collective oscillation of the conduction electron plasma in metals[4] and the excitation of SPR can be understood from the optical properties of metals.

2.1.1 Optical properties of metals

The optical properties of metals can be understood and described by a simple plasma model, where the metals consist of a gas of free electrons that oscillate in response to an applied electromagnetic field, *i.e.* incident light.[8] The position of free-electrons $\mathbf{x}(t)$ under the external electric field $\mathbf{E}$ can be described as:

$$m\ddot{\mathbf{x}} + m\gamma\dot{\mathbf{x}} = -e\mathbf{E} \tag{2.1}$$

where m is the effective optical mass of each electron and γ is a characteristic collision frequency defined as an inverse of the relaxation time (τ) of free electron gas ($\gamma \equiv 1/\gamma$). For a time-varying electric field $\mathbf{E}(t) = \mathbf{E_0}e^{-i\omega t}$, the solution of Equation (2.1) then becomes:

$$\mathbf{x}(t) = \frac{e\mathbf{E}(t)}{m(\omega^2 + i\gamma\omega)} \ . \tag{2.2}$$

And the macroscopic polarization contributed from the motion of electrons is then given by:

$$\mathbf{P} = -me\mathbf{x} = -\frac{ne^2}{m(\omega^2 + i\gamma\omega)}\mathbf{E}(t) \ . \tag{2.3}$$

Now the dielectric displacement $\mathbf{D}$ is given by:

$$\mathbf{D} = \epsilon_r\epsilon_0\mathbf{E} = \epsilon_0\mathbf{E} + \mathbf{P} = \epsilon_0(1 - \frac{\omega_p^2}{\omega^2 + i\gamma\omega})\mathbf{E} \tag{2.4}$$

where the plasma frequency ω_p is defined as:

$$\omega_p^2 \equiv \frac{ne^2}{\epsilon_0 m} \ . \tag{2.5}$$

From Equation (2.4), the dielectric function of the free electron gas is derived as:

$$\epsilon_r(\omega) = 1 - \frac{\omega_p^2}{\omega^2 + i\gamma\omega} = \epsilon_1(\omega) + i\epsilon_2(\omega) \ , \tag{2.6}$$

where the real and imaginary components of the dielectric function are given by:

$$\epsilon_1(\omega) = 1 - \frac{\omega_p^2\tau^2}{1 + \omega^2\tau^2} \ , \tag{2.7a}$$

$$\epsilon_2(\omega) = \frac{\omega_p^2\tau^2}{\omega(1 + \omega^2\tau^2)} \ . \tag{2.7b}$$

Equation (2.6) is called the *Drude* model. In the visible and near-infrared frequencies, where $\omega \gg \gamma$ ($\omega\tau \gg 1$), the imaginary part is negligible and $\epsilon_\gamma(\omega)$ is predominantly real and is approximately:

$$\epsilon_r(\omega) = 1 - \frac{\omega_p^2}{\omega^2} \ . \tag{2.8}$$

Therefore, the dispersion of free electron gas and thus optical properties of metals are determined by the oscillation frequency of free electrons compared to the plasma

frequency (ω_p). To understand the optical properties of metals, one should also consider the *wave equation* of electromagnetic field, solved by using Maxwell's equation and given by:

$$\nabla \times \nabla \times \mathbf{E} = -\mu_0 \frac{\partial^2 \mathbf{D}}{\partial t} \tag{2.9a}$$

$$\mathbf{K}(\mathbf{K} \cdot \mathbf{E}) - K^2 \mathbf{E} = -\epsilon(\mathbf{K}, \omega) \frac{\omega^2}{c^2} \mathbf{E} \tag{2.9b}$$

where $\mathbf{K}$ is the wavevector of the plane wave and c is the speed of light given by $c = \frac{1}{\sqrt{\mu_0 \epsilon_0}}$. For transverse waves, $\mathbf{K} \cdot \mathbf{E} = 0$, yielding the generic dispersion relation:

$$K^2 = \epsilon(\mathbf{K}, \omega) \frac{\omega^2}{c^2} \ . \tag{2.10}$$

For longitudinal waves, $\mathbf{K}(\mathbf{K} \cdot \mathbf{E}) = K^2 E = 0$, implying:

$$\epsilon(\mathbf{K}, \omega) = 0 \ . \tag{2.11}$$

From Equation (2.8), for $\omega > \omega_p$, the dielectric function of metal $\epsilon_r(\omega) > 0$, and thus, the wavenumber K becomes a real value, meaning that the transverse waves propagate through the metal similar to a dielectric material. For $\omega < \omega_p$, $\epsilon_r(\omega) < 0$, and thus, K becomes a complex value, meaning that the propagation of transverse electromagnetic waves is forbidden inside the metal, and decays exponentially into the metal. This exponentially decaying field is called *evanescent* field. For $\omega = \omega_p$, $\epsilon_r(\omega) = 0$, indicating that the longitudinal waves can only occurs at this freqency as described in Equation 2.11. In this case, all electrons are collectively oscillating in phase across the metal at the oscillation frequency of ω_p. This is called *volume plasmon*. If the metal is semi-infinite to the direction of oscillation, the resonant frequency of surface plasmon becomes $\omega_{sp} = \frac{\omega_p}{\sqrt{2}}$.[9]

2.1.2 Surface plasmon polaritons

While the volume plasmon is a collective longitudinal oscillation of the free electron gas in the material volume, the *surface plasmon* (SP) is a collective oscillation lying at the

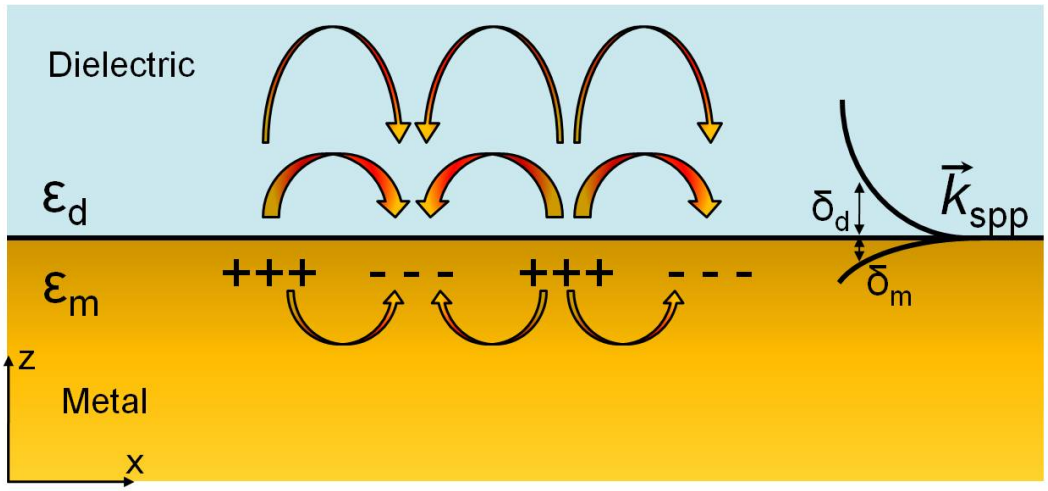

Figure 2.1: **Surface plasmon polaritons (SPPs).** Surface plasmon polaritons are electromagnetic waves propagating along the interface between a metal and a dielectric medium. The energy of the wave is evanescently confined both into the metal and dielectric medium with the decay length, denoted as δ_m and δ_d.

interface between a metal and a dielectric medium. *Surface plasmon polaritons* (SPPs) are electromagnetic surface waves that are generated from coupling of a photon with the oscillating free electrons and propagate along the interface between the metal and dielectric, evanescently confined in the perpendicular direction.[10] To understand the properties of SPPs, the wave equation described in Equation (2.9a) is used. Assuming a harmonic time dependence, an electric field $\mathbf{E}$ simplifies the equation to:

$$\nabla^2\mathbf{E} + \left(\frac{\omega}{c}\right)^2 \epsilon\mathbf{E} = 0 \tag{2.12}$$

For a simple case that the electromagnetic waves propagate along a flat xy plane at $z = 0$ between a dielectric medium ($z > 0$) and a metal ($z < 0$) as depicted in Figure 2.1, for $\omega < \omega_p$, $\mathrm{Re}[\epsilon_m(\omega)]$ is negative and $k(z)$ is complex, meaning the wave evanescently decays into the metal. For transverse-magnetic (TM) waves, wherein the electric field has x and z components and the magnetic field has only a y component, the boundary

conditions for the continuity of H_y and ϵE_z at the interface yield:

$$\frac{k_{z,m}}{\epsilon_m} = -\frac{k_{z,d}}{\epsilon_d} \tag{2.13a}$$

$$k_{x,m} = k_{x,d} = k_x \tag{2.13b}$$

where k_x and k_z are the x- and z-components of wavevector $\mathbf{K}$, ϵ is the dielectric constant, and m and d denote metal and dielectric, respectively. It should be noted that the negative sign in Equation (2.13a) indicates that the surface waves only exist at the interface of materials with opposite signs of dielectric permittivities, *e.g.* an interface between a metal ($\mathrm{Re}[\epsilon_m] < 0$) and a dielectric medium ($\epsilon_d > 0$). Equation (2.10) can be express as:

$$k_{x,m}^2 + k_{z,m}^2 = \epsilon_m(\tfrac{\omega}{c})^2 \tag{2.14a}$$

$$k_{x,d}^2 + k_{z,d}^2 = \epsilon_d(\tfrac{\omega}{c})^2 \ . \tag{2.14b}$$

Solving Equation (2.14) with Equation (2.13) gives the dispersion relation of SPP:

$$k_{spp} = k_x = \frac{\omega}{c}\sqrt{\frac{\epsilon_d\epsilon_m}{\epsilon_d + \epsilon_m}} \tag{2.15}$$

For transverse-electric (TE) waves, however, the boundary conditions for the continuity of H_x and ϵE_y at the interface yield leads to $k_{x,m} + k_{x,d} = 0$. Since confinement to the surface requires both $\mathrm{Re}[k_{x,m}]$ and $\mathrm{Re}[k_{x,d}]$ are positive, this leads to a conclusion that SPPs only exist for TM polarization. When ϵ_d and ω are real, $\epsilon_m = \epsilon_m' + i\epsilon_m''$, $|\epsilon_m'| \gg \epsilon_m''$, and $|\epsilon_m'| > \epsilon_d$ at optical frequency, and thus, the wave-vector becomes $k_{spp} = k_{spp}' + ik_{spp}''$ where

$$k_{spp}' = \frac{\omega}{c}\sqrt{\frac{\epsilon_d\epsilon_m'}{\epsilon_d + \epsilon_m'}} \tag{2.16a}$$

$$k_{spp}'' = \frac{\omega}{c}\left(\sqrt{\frac{\epsilon_d\epsilon_m'}{\epsilon_d + \epsilon_m'}}\right)^3 \frac{\epsilon_m''}{2\epsilon_m'^2} \tag{2.16b}$$

The propagation length of SPP along the interface is given by $L = (2k''_{spp})^{-1}$ and the decay length to the perpendicular direction is given by $\delta = 1/k_z$, leading to:

$$\delta_d = \frac{\lambda}{2\pi}\sqrt{\frac{\epsilon'_m + \epsilon_d}{-\epsilon_d^2}}\,, \tag{2.17a}$$

$$\delta_m = \frac{\lambda}{2\pi}\sqrt{\frac{\epsilon'_m + \epsilon_d}{-\epsilon_m^2}}\,. \tag{2.17b}$$

Equation 2.17 indicates that for noble metals such as Cu, Ag, and Au in the visible range the field decays more abruptly in the metal than in a free space because $|\epsilon_m| > \epsilon_d$ in the range.[11]

2.1.3 Surface plasmon resonance

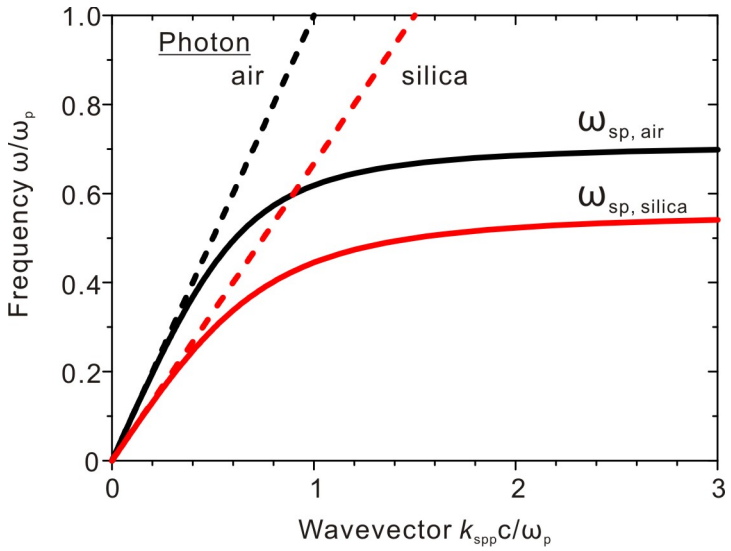

Figure 2.2: **Dispersion relation of SPPs.** The solid lines represent the dispersion curves of SPPs at the interfaces between Au and dielectric media (air and silica) and the dashed lines presents light lines in the dielectric media.

Figure 2.2 presents the dispersion relation of SPPs at the interfaces between Au and dielectric media (air, silica). It is seen that the dispersion curves of SPPs always lie to

the right of the respective light lines of the dielectrics given by $\omega = ck$. This implies the SPP cannot be excited directly by light on the flat Au surface. This is due to the mismatch of momentums ($k_{spp} > k_x = k\ sin\theta$) between SPP and incident light at any incidence angle.

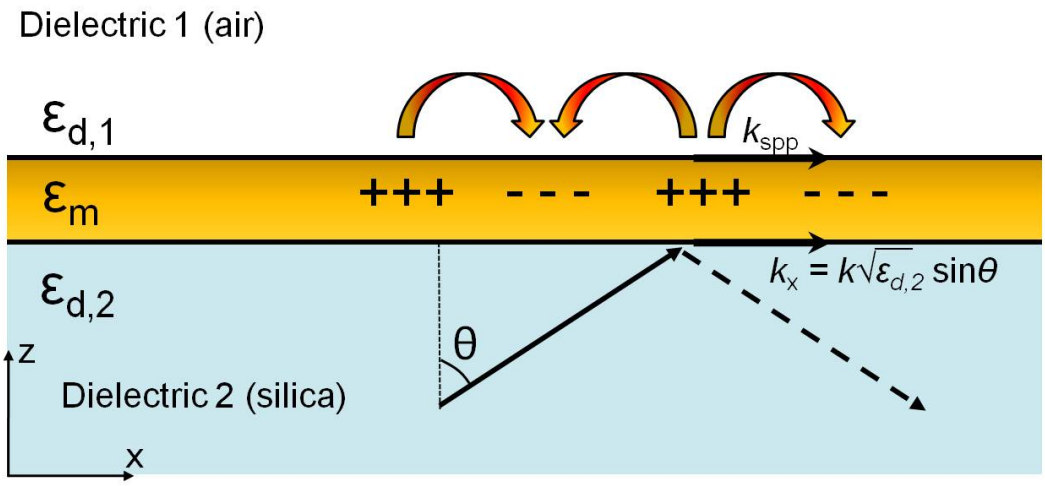

Figure 2.3: **Kretschmann configuration.** In the Kretschmann configuration, a thin metal film is sandwiched between two dielectric materials with different dielectric constants. At a certain incidence angle, incident light through a medium with higher dielectric constant can excite SPPs at the interface between metal and the other medium with lower dielectric constant.

Matching of the momentum, however, could be achieved by prism or grating coupling. In the prism coupling, a thin metal film is sandwiched between two dielectric materials with different dielectric constants, *e.g.* air and silica as presented in Figure 2.3. When light is reflected at the interface between Au and silica, it has the in-plane momentum of $k_x = k\sqrt{\epsilon_{silica}}\ sin\theta$, which is now sufficient to match and excite SPPs at the interface between Au and air at a certain angle at which the dispersion curve of SPP at metal/air interface cross the light line of silica as shown in Figure 2.2. The excitation of SPPs results in a sharp dip in reflected intensity at the angle of incidence as shown in Figure 2.4. The minimum dip in the intensity of the reflected light is due to destructive

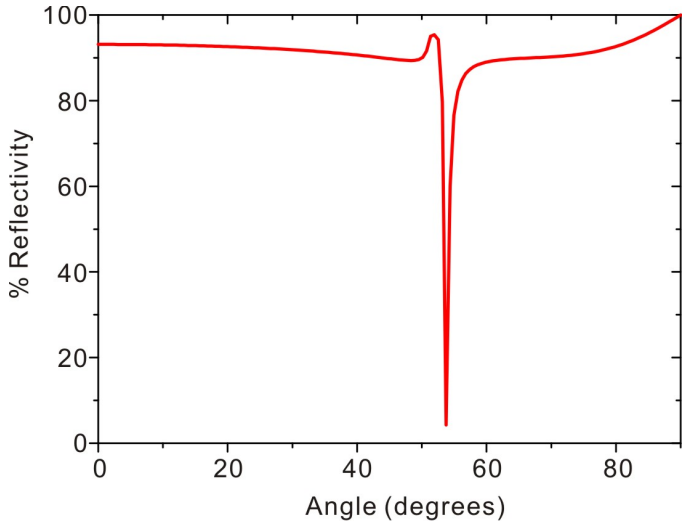

Figure 2.4: **Reflectance vs. the incident angle in the Kretschmann configuration.** The excitation of SPPs at a certain angle results in a sharp dip in the reflected light intensity due to excitation of SPPs in a metal film. In this example, $\epsilon_{d,1}$ and $\epsilon_{d,2}$ are 1.33 and 1.71, respectively and 45 nm thick Au is used with incident light at the wavelength of 814 nm.

interference between SPPs and the reflected light. This is called *Kretschmann* configuration.[12] Similarly, in the grating coupling, the mismatch of wave vectors is overcome by adding a reciprocal vector (k_g) from periodic grating so that

$$k_{spp} = ksin\theta + k_g = ksin\theta + \frac{2\pi m}{p} \tag{2.18}$$

where m is the grating order and p is the periodicity of grating.

2.2 Extraordinary Optical Transmission

When light passes through a single aperture in an opaque film, its transmission through the aperture is accompanied by *diffraction*. In the classical diffraction theory, an analytical solution for light transmission through a sub-wavelength circular aperture or nanohole with a radius r in a perfectly conducting, infinitely thin film is described by

assuming the hole as a magnetic dipole. This is called *Bethe's aperture theory.*[13] In this approximation, the transmission efficiency, transmission normalized by the aperture area, for an incident plane wave is given by:

$$T = \frac{64}{27\pi^2}(kr)^4 \tag{2.19}$$

where $k = 2\pi/\lambda$ is the wavevector of incident light. Therefore, the transmission is proportional to the fourth power of r/λ, indicating very weak transmission through a hole with a size smaller than the wavelength of incident light. As mentioned earlier, this analytical solution is based on the assumption of infinitely thin, perfectly conducting opaque film. If the finite thickness of perfect conduction film is considered, the transmission coefficient, T, further decreases exponentially with the thickness.[14]

In 1998, Ebbesen and co-workers reported that when a periodic array of these subwavelength holes are made in an opaque "real" metal film, the light transmission through the hole array is dramatically enhanced compared to what one would expect from Bethe's theory. Surprisingly, the transmission efficiency normalized by the hole area was larger than unity.[15] This is the so-called *extraordinary optical transmission* (EOT) effect.[15,16] While there is still a debate on the mechanism of the EOT effect, the SPP excited by the periodic nanohole grating plays a major role in the enhanced optical transmission.[17–19] For a nanohole array in a period a_0, the wavevector of SPP is then expressed as:

$$k_{spp} = k_x + k_{gx} + k_{gy} = k_0 \, sin\theta + n\frac{2\pi}{a_0} + m\frac{2\pi}{a_0} \tag{2.20}$$

where n and m are the scattering orders of the array. For normally incident light, Equation (2.20) becomes:

$$\lambda_{spp}(n,m) = \frac{a_0}{\sqrt{n^2+m^2}}\sqrt{\frac{\epsilon_d\epsilon_m}{\epsilon_d+\epsilon_m}} \, . \tag{2.21}$$

Therefore, the resonance condition is sensitive to the refractive index of medium, the main principle of SPR biosensing using the nanohole array.[15,20] Figure 2.5 shows a

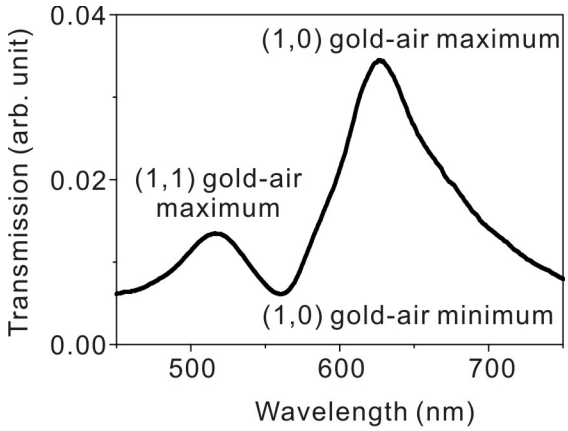

Figure 2.5: **An EOT spectrum through a periodic nanohole array.** The nanohole array is made in an optically thick ($\sim$ 200 nm) Au film. The hole size and the periodicity are 200 and 500 nm, respectively. Maximum and miminum peaks corresponding to (1,0) and (1,1) reosnances at the gold-air interface are labeled.

transmission spectrum through a periodic nanohole array made in an Au film. The geometrical properties of nanohole array such as periodicity,[15] hole size and shape,[20–22] and the film thickness[23] play a critical role to determine the resonance condition. Depending on destructive or constructive interference with SPP excited by the nanohole array, the maximum or minimum transmission peaks are observed. The minimum transmission peak position is close to the wavelength of λ_{spp} predicted using Equation (2.20) and the maximum transmission peak is located a bit longer wavelength than the position of the minimum transmission peak.[24]

2.3 Analysis of Molecular Binding Kinetics

The simplest molecular interaction model is binary interaction where one analyte molecule interacts with one ligand at a single binding site. Many practical interactions often approximate to this 1:1 binding model as depicted in Figure 2.6. For reversible interaction,

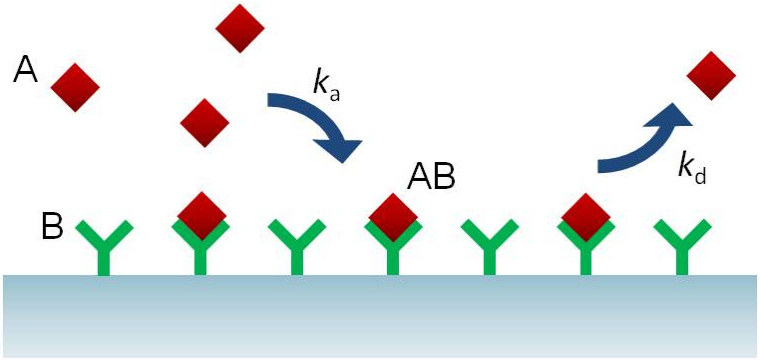

Figure 2.6: **1:1 molecular binding model.** An analyte molecule ('A') binds to a ligand ('B') immobilized on the surface to form a complex ('AB') with an association rate constant (k_a). The complex reversibly dissociates with a dissociation constant (k_d).

it is represented in a reaction scheme as:

$$\mathrm{A} + \mathrm{B} \underset{\mathrm{k_d}}{\overset{\mathrm{k_a}}{\rightleftharpoons}} \mathrm{C} \tag{2.22}$$

where k_a and k_d are association and dissociation rate constants of complex, AB, respectively. Then, the rate of formation of the complex at time t can be written as:

$$\frac{d[\mathrm{AB}]}{dt} = k_a[\mathrm{A}][\mathrm{B}] - k_d[\mathrm{AB}] \tag{2.23}$$

where the first notation in the right side represents the association of analyte and ligand to be the complex, and the later one represents the dissociation of the complex. After some reaction time, $[\mathrm{B}] = [\mathrm{B}]_0 - [\mathrm{AB}]$. Substituting this into Equation (2.23) gives:

$$\frac{d[\mathrm{AB}]}{dt} = k_a[\mathrm{A}]([\mathrm{B}]_0 - [\mathrm{AB}]) - k_d[\mathrm{AB}] \tag{2.24}$$

where $[\mathrm{B}]_0$ is the concentration of B at $t = 0$. In often cases for solid-state biosensors, a ligand ('B') is immobilized on the sensing surface and a soluble analyte ('A') with the constant concentration, C, is introduced for the interaction. In a linear response regime, binding of the analyte to the ligand induces a response signal, R, proportional

to the amount of 'AB' complexes. The maximum response signal, R_{max}, observed when all binding sites are occupied, is thus proportional to the initial surface concentration of ligand, $[B]_0$. Therefore, Equation (2.24) can be re-written as:

$$\frac{dR}{dt} = k_a C(R_{max} - R) - k_d R \tag{2.25}$$

where dR/dt is the rate of complex formation, and C is the concentration of analyte. Rearranging Equation (2.25) gives:

$$\frac{dR}{dt} = k_a C R_{max} - (k_a C + k_d)\, R \tag{2.26}$$

2.3.1 Equilibrium binding assays

In equilibrium binding assays, after the analyte is introduced to the active ligand, the response signal is continuously recorded until the reaction reaches the equilibrium state, *i.e.* until the rate of association is equal to the rate of dissociation. Thus, in the equilibrium state, $dR/dt = 0$ and Equation (2.26) reduces to:

$$0 = k_a C R_{max} - (k_a C + k_d)\, R_{eq} \tag{2.27}$$

where R_{eq} is the response signal at the equilibrium state. Rearranging Equation (2.27) gives:

$$\frac{1}{R_{eq}} = \frac{1}{R_{max}} + \frac{1}{K_A R_{max}} \cdot \frac{1}{C} \tag{2.28}$$

where K_A is the association constant defined by k_a/k_d. A plot of $1/R_{eq}$ against $1/C$ thus fits into a straight line from which R_{max} and K_A can be calculated from the slope and intercept of the fitted line. In another approach, the association constant is defined as:

$$K_A = \frac{[AB]}{[A][B]} = \frac{R_{eq}}{C \cdot (R_{max} - R_{eq})}\ . \tag{2.29}$$

This equation is called as the *Langmuir isotherm* or *Langmuir adsorption equation.*[25] Equation (2.28) can be obtained by rearranging Equation (2.29).

	$k_d(s^{-1})$				
Concentrations	10^{-1}	10^{-2}	10^{-3}	10^{-4}	10^{-5}
$100 \cdot K_D$	0.7 s	6.8 s	68 s	11.4 min	114 min
$10 \cdot K_D$	6.3 s	63 s	10.5 min	105 min	17.4 hr
K_D	35 s	5.8 min	57.6 min	9.6 hr	96 hr
$0.1 \cdot K_D$	63 s	10.5 min	105 min	17.4 hr	174 hr
$0.01 \cdot K_D$	68 s	11.4 min	114 min	19 hr	190 hr

Table 2.1: **Reaction times required to reach the steady state.** Approximately calculated times to reach 99.9 % of the equilibrium response signal at various concentrations and dissociation rate constants values.

Indeed, this approach is useful for low-affinity interaction with a k_d value of around 10^{-3} or larger, but impractical for strong binders ($k_d < 10^{-}3$) due to the length of reaction time in order to reach to the steady state. Table 2.1 summarizes times required to reach to 99.9 % of the equilibrium response signal at various concentrations and dissociation rate constants values. This equilibrium assays and Langmuir isotherm model are often used for labeled detection methods such as fluorescence microscopy[2] and ELISA.[3] In these methods, the end-point responses are obtained when the reaction reaches to the equilibrium state and the obtained values at various concentrations are used to calculate the dissociation constant. A drawback of the method is that it could calculate K_A value, but not individual k_d and k_a values unless the dissociation rate constant is accurately measured, which is not trivial in equilibrium assays.

2.3.2 Real-time kinetic assays

Measuring k_d and k_a values provide more detailed information on molecular interactions, especially to determine the dose and potency duration of drug molecules. Because the dissociation constant is determined by the ratio of those two rate constants, the same dissociation constant can be obtained from different k_d and k_a values. Figure 2.7 shows

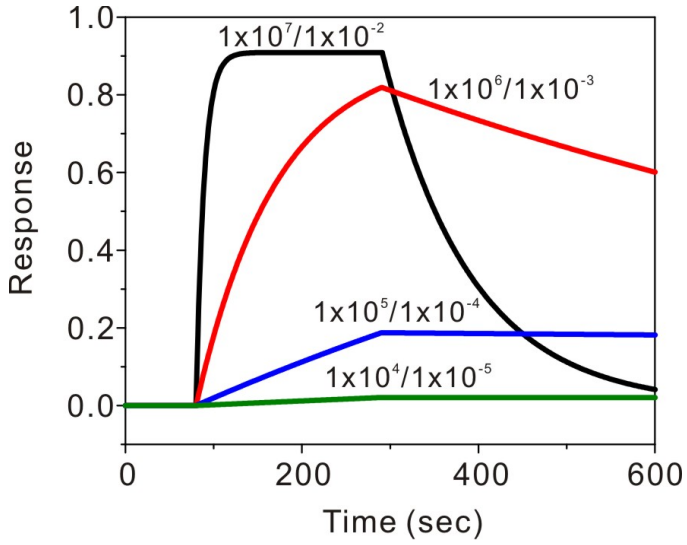

Figure 2.7: **Binding kinetic curves with the same association constant.** Binding behaviors of molecule pairs with the same association constant ($K_A = 1 \times 10^9$) can be different depending on the association and dissociation rate constants (k_a, k_d).

binding kinetic curves from the same dissociation constant, but different sets of k_d and k_a values. Depending on the rate constants, the binding kinetics may be different even with the same dissociation constant. Therefore, it is important to know the individual k_d and k_a values to better understand the chemical reaction. To measure individual k_d and k_a values, the kinetic responses need to be recorded in real-time. In Equation (2.26), a plot of dR/dt versus R yields a linear slope, k_{obs}, defined as:

$$k_{obs} = k_a C + k_d \ . \tag{2.30}$$

Measuring k_{obs} values at various concentrations allows plotting k_{obs} versus C. From this plot the k_a and k_d values are obtained *via* the slope and y-intercept, respectively. This is called a linear transform method. In this method, kinetics curves measured at various concentrations are analyzed to calculate a single value for k_a and k_d. Despite the linear transform method provides information of k_a and k_d values, because a single value of the parameter is derived from multiple kinetic curves, it also transforms the

errors in the primary data.[26] Therefore, errors in the derived parameters no longer directly reflect the errors in the primary data. For examples, errors occurred during k_{obs} calculation also affect to determine the k_a and k_d values. Also it requires kinetic curve at least two or three different concentrations in order to obtain the linear slope, k_{obs}. For these reasons, it is advantageous to analyze the kinetics data directly using an integrated form of the rate equation expressed as:[26]

$$R_t = \frac{C\,k_a\,R_{max}[1 - e^{-(Ck_a + k_d)\,t}]}{C\,k_a + k_d} + R_i \tag{2.31}$$

where R_t is a response signal at time t and R_i is an initial signal at the point of analyte is introduced at time $t = 0$. In this rate equation form, errors in the derived parameters, k_a and k_d directly reflect errors in the primary data. Additionally, in the real-time kinetic measurement, the dissociation process of the complexes, 'AB', is observed directly when the analyte solution is placed by a buffer solution, *i.e.* [A] = 0. Therefore, the rate of dissociation is now described by:

$$\frac{dR}{dt} = -k_d R \tag{2.32}$$

and this can be also expressed in a form of integrated equation as:

$$R_t = R_a e^{-k_d t} + R_{t\to\infty} \tag{2.33}$$

where R_a is the amplitude of the dissociation process, often the response value just before dissociation process starts, and $R_{t\to\infty}$ is the response signal when dissociation process completed. After baseline correction where R_i is defined as 0, $R_{t\to\infty}$ is also regarded as 0. In the calculation of k_d and k_a values, first the dissociation kinetic curve is analyzed to calculate the k_d value obtained from a linear slope in a plot of $\ln(R_a/R_t)$ versus time. The k_a value is then calculated by obtaining the time constant, $Ck_a + k_d$, from a linear slope in the plot of $\ln(R_a/R_t)$ versus time. In this approach, k_a and k_d are determined for every single kinetic curve. Therefore it provides a statistical data set of k_a and k_d to determine reproducibility or certainty in the derived parameters.

While colorimetric detection methods such as fluorescence microscopy[2] and ELISA[3] provide the end-point response values, SPR sensors can records response signals in a real-time manner.[5] Details of the difference between SPR and other detection methods will be described in Chapter 3. Therefore, using the real-time kinetic analysis, SPR sensors can measure the dissociation constant as well as k_d and k_a values from each single kinetic curve. Unlike the equilibrium measurements, which measures response signals at the equilibrium state, the real-time SPR sensing allows measuring kinetic parameters precisely with shorter time and smaller reagent consumption compared to the colorimetric detection.

Chapter 3

Surface Plasmon Resonance Biosensing

Real-time kinetic measurement of molecular interaction provides essential information for new drug discovery and proteomics research. Surface plasmon resonance (SPR) techniques enable the real-time measurements of molecular binding kinetics in a label-free manner and hence have been extensively used both in academia and industry to characterize various types of molecular interactions between nucleic acids, proteins, viruses, and enzymes. This chapter describes an overview of SPR biosensing and introduces a new type of SPR biosensor based on periodic nanohole arrays, which utilize the effect of extraordinary optical transmission (EOT) described in Chapter 2. The result shown in this chapter is mainly derived from the following presentation and publication:

1. H. Im, A. Lesuffleur, N. C. Lindquist, K. S. Lim, S. H. Oh, *Frontiers in Nanophotonics and Plasmonics*, Guaruja, Sao Paulo, Brazil (2007).[27]

2. A. Lesuffleur, H. Im, N. C. Lindquist, S.H. Oh, *Applied Physics Letter* **91**243110 (2007).[28]

3.1 Surface Plasmon Resonance Biosensing

As presented in the Chapter 2, the resonance condition to excite SPR relates to the dielectric properties of both metal and surrounding medium. Thus, SPR devices become sensitive to the refractive index change. Because SPR devices are based on evanescent fields with a decay length of only 100 – 300 nm in the visible wavelength range for sensing, it is more sensitive to the the refractive index chance near the surface. For SPR biosensing, molecular binding to the sensing surface or to target molecules immobilized on the surface induces the "local" refractive index change near the surface if the bound molecule has a different refractive index from the "bulk" refractive index of the medium, typically water or buffer solution. The change in the local refractive index due to molecular binding affects the resonance condition of surface plasmons (SPs), resulting in shifts of the excitation angle or wavelength.

BIAcore^{TM} from GE healthcare is one of most successful commercialized SPR instruments and has been widely used in biomedical and proteomics research. It consists of a transparent prism coated with a thin ($\sim$ 50 nm) gold film. A light illuminates a detection spot on the gold film through the prism with an incidence angle greater than the critical angle and the monitors the reflected light intensity. This is called the Kretschmann configuration. In the Kretschmann configuration, as shown in Figure 3.1, in the case of using monochromatic light, it monitors intensity versus the angle of incidence, and in case of using a white light source, it monitors intensity versus the wavelength at a fixed angle. At certain incident angles or wavelengths, part of the incident light energy couples with free electrons and converts to SPs. The angular distribution of the reflected light intensity is measured by a photodiode array in real-time, scanning for a steep attenuation of reflectivity caused by the loss of the energy, which indicates the resonant excitation of SPs. The response of the SPR sensor characterized by a shift in resonance angle ($\Delta\theta$) or wavelength ($\Delta\lambda$) is induced by refractive index change (Δn) of the medium. In a narrow sensing window, the response (R) to changes in refractive

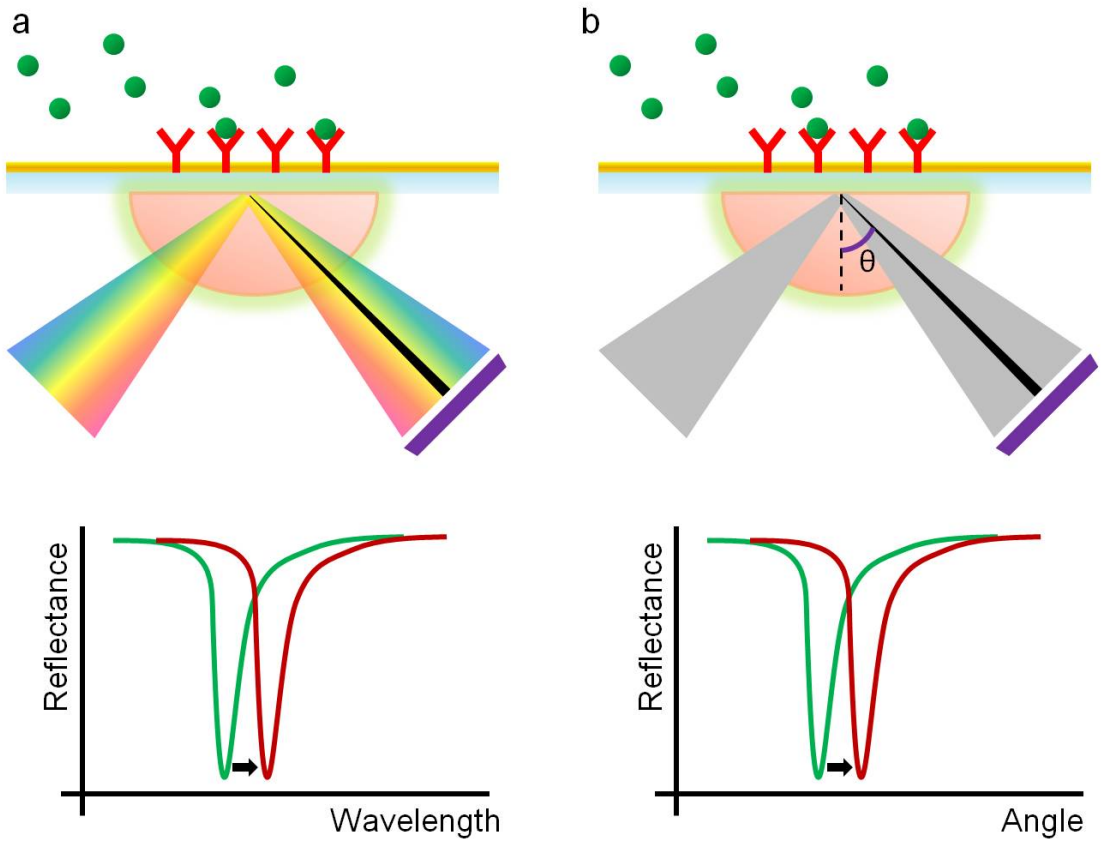

Figure 3.1: **Principle of SPR sensing in the Kretschmann configuration.** Depending on experimental setup, the SPR condition can be measured as a dip in the reflected light intensity versus either (a) the wavelength in which a broadband white light source at a fixed angle is used or (b) the angle of incidence in which a monochromatic light source at a fixed wavelength is used. Molecular binding on the metal surface shifts the dip position.

index can be approximated as linear:[29]

$$R = m\Delta n \tag{3.1}$$

where m is the refractive index sensitivity of the sensor which is usually expressed as deg/RIU (RIU = refractive index unit) or nm/RIU. In other words, the sensitivity of SPR sensor can be characterized by measuring the shift of resonant angle or wavelength corresponding to a bulk refractive index change. Because SPR is based on evanescent electromagnetic fields exponentially decaying from the sensing surface with a decay length, l_d, a proper weighting factor should be considered when the local refractive index change occurs only near the surface wherein the thickness is shorter than the decay length, *e.g.* adsorption of molecules on the sensor surface. The proper weighting factor would be proportional to the intensity of light,[29] which is a square of the field strength at each point. Thus, the effective refractive index can be express as a weighted average with the depth integral:

$$n_{eff} = \frac{2}{l_d}\int_0^\infty n(z)exp(-2z/l_d)\mathrm{d}z \tag{3.2}$$

where $n(z)$ is the refractive index at height z. For the simple case of a molecular layer adsorbed on the sensing surface with a thickness, d_{mol}, and a refractive index, n_{mol}, the equation (3.2) can be simplified to:

$$n_{eff} = n_{bulk} + (n_{mol} - n_{bulk})[1 - exp(-2d_{mol}/l_d)] \tag{3.3}$$

where n_{bulk} is the bulk refractive index of the dielectric medium. For many of biomolecules, the refractive index of molecule is proportional to the mass of molecule.[30] Therefore, the SPR response can be converted to the surface density of molecule bound on the surface.[31] For example, in the BIAcore system with a sensor chip functionalized with a dextran layer, a SPR response of 1,000 RU (RU = response unit, 1 RU = 10^{-4} deg) corresponds approximately to 1 ng/mm^2.[31,32] According to Homola *et al.*,[5] the BIAcore system shows a refractive index sensitivity of about 100 deg/RIU, corresponding

to a minimum resolution of 10^{-6} RIU. Another class of SPR sensor utilizes the localized surface plasmon resonance (LSPR) wherein the electromagnetic fields are even more tightly confined at the surface with a decay length on the order of 10 nm.[33–35] For example, metallic nanoparticles and randomly arranged nanohole arrays in thin ($<$ 50 nm) metallic films can act as the LSPR sensors. The short decay length makes the LSPR sensors very sensitive to the binding of small molecules. It has been demonstrated that the LSPR sensors can even detect zeptomoles of molecules,[34] protein conformation changes,[36] and inert gases.[37] A drawback of an LSPR sensing scheme is its short probing range, especially when the surface needs to be functionalized by multi-layers or large molecules. Unlike other optical detection methods such as ELISA or fluorescence microscopy, SPR sensing does not require labeling of target analytes. In addition, because there is no photobleaching of fluorescent dyes, SPR sensors can continuously monitor molecular binding interactions in a real-time manner, allowing rate-based measurements, while ELISA or fluorescence methods measure only the end-point response signal. This real-time label-free sensing capability provides a number of advantages compared to label-based detection methods. First, SPR sensors do not require any additional labeling process for characterizing molecular interactions, whereas ELISA requires a step to react with secondary reagent to be able to measure the amount of complex formed, and fluorescence-based assays require attaching fluorescence dyes to molecules. This labeling process is costly and time-consuming. Also, the added fluorophores may interfere with binding interactions. Second, assays using labels involve a number of washing steps where analyte that dissociates from target molecules can be lost. Therefore, while only high-affinity molecular interactions are suitable for the label-based assays, SPR is not limited by the strength of the molecular interactions. Because of its capability of characterizing a wide range of molecular interactions in a label-free real-time manner with high sensitivity, SPR biosensors have been widely used in both academia and industry for pharmaceutical development of new drug molecules as well as fundamental proteomics research. Despite the commercial success of BIAcore$^{\text{TM}}$

instruments, there are still several disadvantages in the system. For example, in the prism-based SPR setup in BIAcore^{TM} is bulky and difficult to align in order to precisely measure the angle of excitation. Also, the high-cost of the SPR ($\sim \$250,000$) is prohibitive to most individual researchers. More importantly, despite many practical applications requiring high-throughput screening capability to study hundreds or thousands of molecular interactions simultaneously as is done with protein microarrays, the current BIAcore systems only have 4 channels that can be monitored simultaneously. This is mainly due to the limited spatial resolution in the prism-coupling configuration. Prism coupling with an angled incident light results in a tilted image plane with a narrow field of view and a wide range of focal depths. This limits the maximum capacity of sensing spots and prohibits the use of high numerical aperture (NA) optics, leading to the limited spatial resolution. Given these limitations, a new class of SPR instrument which is suitable for miniaturization, high-resolution, low-cost, and high-throughput is clearly needed.

3.2 SPR Biosensing with Plasmonic Nanohole Arrays

In contrast to SPR sensors based on the Kretchmann and grating configurations, which detect reflected light from the sensing surface, a new SPR sensor made by periodic nanohole arrays utilizes the transmitted light through sub-wavelength sized nanoholes. As described in Chapter 2.2, light transmission through periodically arranged nanoholes in metallic films is enhanced at specific wavelengths, mediated by SPs excited on both sides of the metal surfaces. Similar to other SPR biosensing instruments, for periodic nanohole arrays, molecular binding to the sensing surface induces changes in local refractive index of medium, shifting the wavelengths of light transmission as shown in Figure 3.2. In contrast with the bulky prism coupling used in the Kretschmann setup, the nanohole array can provide (1) a collinear, transmission measurement setup that greatly simplifies and miniaturizes optical design, alignment, and imaging and (2) a

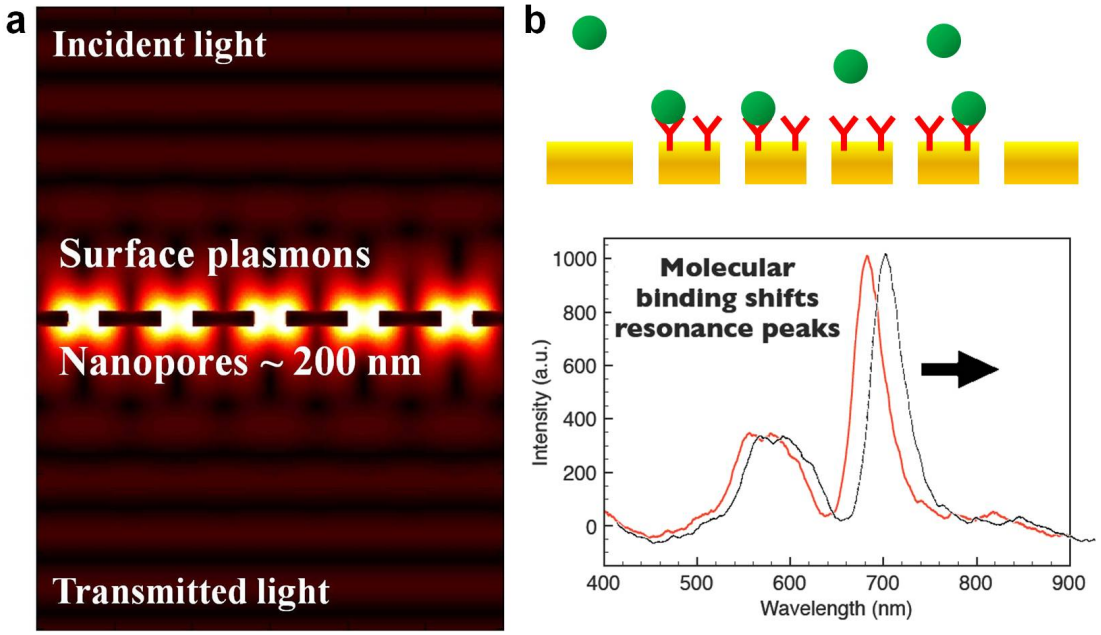

Figure 3.2: **Concept of nanohole-based SPR biosensing with EOT.** (a) Finite-difference time-domain (FDTD) computer simulation[38] shows that incident light excites surface plasmons (SPs) around sub-wavelength nanoholes and light transmission at specific wavelengths is greatly enhanced. This is so-called extraordinary optical transmission (EOT). (b) Similar to other SPR biosensors, molecular binding to the sensing surface induces a local refractive index change, red-shifting the optical transmission spectrum.

small-footprint sensing probe ($\sim 10\ \mu m \times 10\ \mu m$), which enables a high packing density for multiplex array sensing. Brolo *et al.* first demonstrated the concept of using periodic nanohole arrays for biosensing by measuring spectral shifts of a transmission peak after modifying a Au nanohole surface with a thiolated self-assembled monolayer (SAM) and subsequently bound bovine serum albumin (BSA).[39] Beyond detection of molecules after binding, measuring their binding kinetics is important to obtain key biophysical parameters such as association and dissociation rates and the corresponding affinity of molecules. In this work, new SPR devices based on periodic nanohole arrays are

also used for label-free, real-time kinetic biosensing by monitoring the spectral shifts of transmission peaks as biomolecules are adsorbed on the gold sensing surface. Unique advantages of nanohole-based SPR sensing for high-throughput SPR imaging (Chapter 4), biosensing with lipid membranes (Chapter 5), and low-cost instrumentation (Chapter 6) will be also described in following chapters.

3.2.1 Experimental details

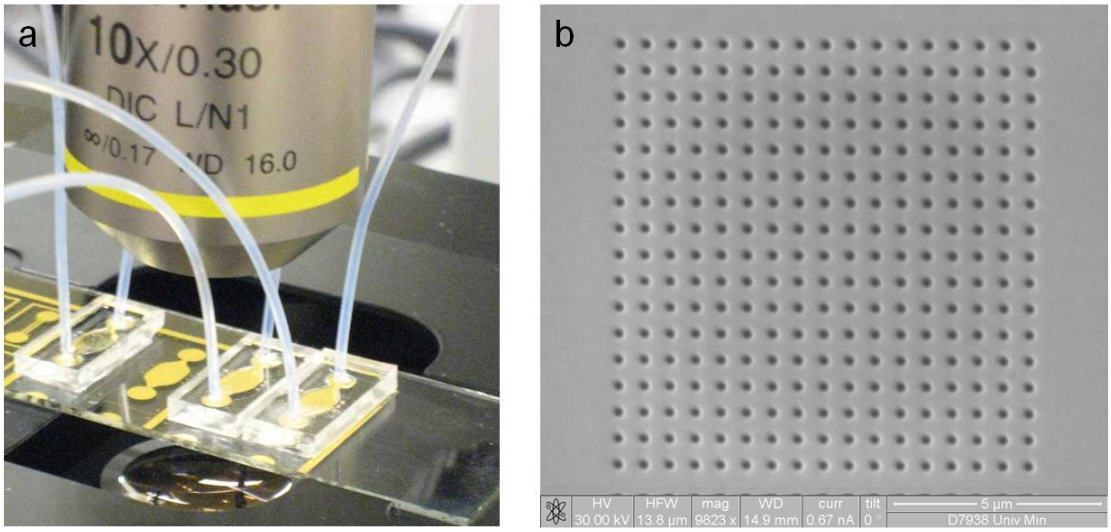

Figure 3.3: **A nanohole array sensor with a PDMS microfluidic chip.** (a) Photograph a PDMS microfluidic chip assembled with a patterned Au film with nanoholes on a glass substrate. (b) A SEM image of the fabricated nanohole array using FIB.

In this work, a patterned Au nanohole array sensor assembled with a microfluidic flow cell was used for real-time kinetic measurements. Figure 3.3 shows the Au nanohole biosensing chip assembled with the microfluidic flow cell. The Au slide was patterned by a lift-off process where a 200 nm-thick Au film with a 5 nm-thick Cr adhesion layer was deposited by evaporation on patterned photoresist, and the metal films deposited

on the photoresist were removed while dissolving the photoresist in acetone. The patterned gold slide was first thoroughly cleaned by acetone, methanol, isopropyl alcohol (IPA), and water for 10 min each with sonication followed by 10 minutes of UV ozone treatment. Focused ion beam (FIB) milling (30 kV, 30 pA) was used to make nanohole arrays with 200 nm hole diameter and 400 nm hole periodicity. Figure 3.3b shows a scanning electron microscope (SEM) image of the fabricated nanohole array using FIB. Soft lithography[40] with polydimethylsiloxane (PDMS) was used to fabricate the microfluidic flow cell. The single-channel PDMS flow cell shown in Figure 3.3a has a height of 100 μm and a maximum width of 3.75 mm. Refer to Appendix B for detailed fabrication and processing techniques. The PDMS microfluidic cell is permanently bonded with the patterned Au nanohole chip. The PDMS flow cell is then connected to a syringe via polytetrafluoroethylene (PTFE) microbore tubing. Analytes and washing buffer solutions were introduced to the sensing area through the microfluidic channel. A syringe pump was used to inject sample solutions at a flow rate ranging from 2 μl/hr to 100 μl/min. For kinetic experiments, the Au chip assembled with PDMS flow cell is mounted on a standard upright optical microscope. The nanohole chip is illuminated by a white light source through a 50$\times$ microscope objective (NA = 0.55) and the transmission spectra are continuously collected with a fiber optic spectrometer. Figure 3.4a presents a typical transmission spectrum of periodic nanohole arrays with the 400 nm periodicity used in the kinetic measurements of SAM formation, biotin immobilization and subsequent binding of streptavidin to the biotin as depicted in Figure 3.4b. Figure 3.4c shows real-time binding kinetic curves during the procedures by tracking the position of minimum transmission around 600 nm. First, the gold surface was soaked with ethanol for 10 min and then functionalized with a self-assembled monolayer (SAM) solution of 4 mM 11-amino-1-undecanethiol hydrochloride. After 2 hrs incubation of the thiolated SAM solution with a flow rate of 4 μl/min, the surface was washed with ethanol and then bicarbonate buffer solutions. Sudden changes in the spectral sensing data during washing steps are due to bulk refractive index changes between different solutions. After

washing with the bicarbonate buffer solution, a 3 mM NHS-LC biotin solution diluted in a bicarbonate buffer solution was injected for another 2 hrs at a flow rate of 4 μl/min to covalently bind biotin to the SAM layer. After the biotin immobilization, the surface was washed by the bicarbonate buffer and then phosphate buffered saline (PBS, pH = 7.4) solutions. Finally, a 750 nM streptavidin solution was injected and incubated at a flow rate of 4 μl/hr for 2 hrs in order to make specific binding of streptavidin to biotin immobilized on the surface. In the kinetic response of streptavidin binding, a sudden change right after injecting the streptavidin solution is due to the bulk index change from PBS to the streptavidin solution, but the rest of kinetics of increasing response is due to the specific binding of streptavidin to biotin immobilized on the surface.[41]

3.2.2 Shape-enhanced plasmon resonance and EOT

One of important parameters for a biosensor is its sensitivity to molecular detection. A strategy to improve the sensitivity of nanohole array is coupling with LSPR which has shorter decay length than propagating SPs and thus shows better sensitivity to detection of small molecules. Previously, Lesuffleur *et al.* demonstrated that the presence of sharp apexes in nanoscale double-hole structure can boost the local field intensity, transmission efficiency, and polarization selectivity compared to circular nanohole arrays due to the LSPR at the sharp apexes.[42] In this work, the improved sensitivity of double-hole array is demonstrated along with the real-time, label-free detection for the biomolecular adsorption. Figure 3.5a shows a SEM image of a double-hole array, which was milled using FIB through a 100-nm-thick Au film with a 5 nm Cr adhesion layer on a glass substrate. The double-hole structure is made by overlapping two circular holes with a 200 nm diameter and a 190 nm center spacing to produce two sharp apexes in between. Each array consists of 40 $\times$ 40 double-holes with a 600 nm periodicity. The refractive index sensitivity of the double-hole array was measured with air ($n = 1.00$), water ($n = 1.33$), and acetone ($n = 1.36$) using a 150 μm height flow cell attached to the gold surface. As shown in Figure 3.5b, the $\lambda_{sp(0,1)}$ peak was shifted by about 200

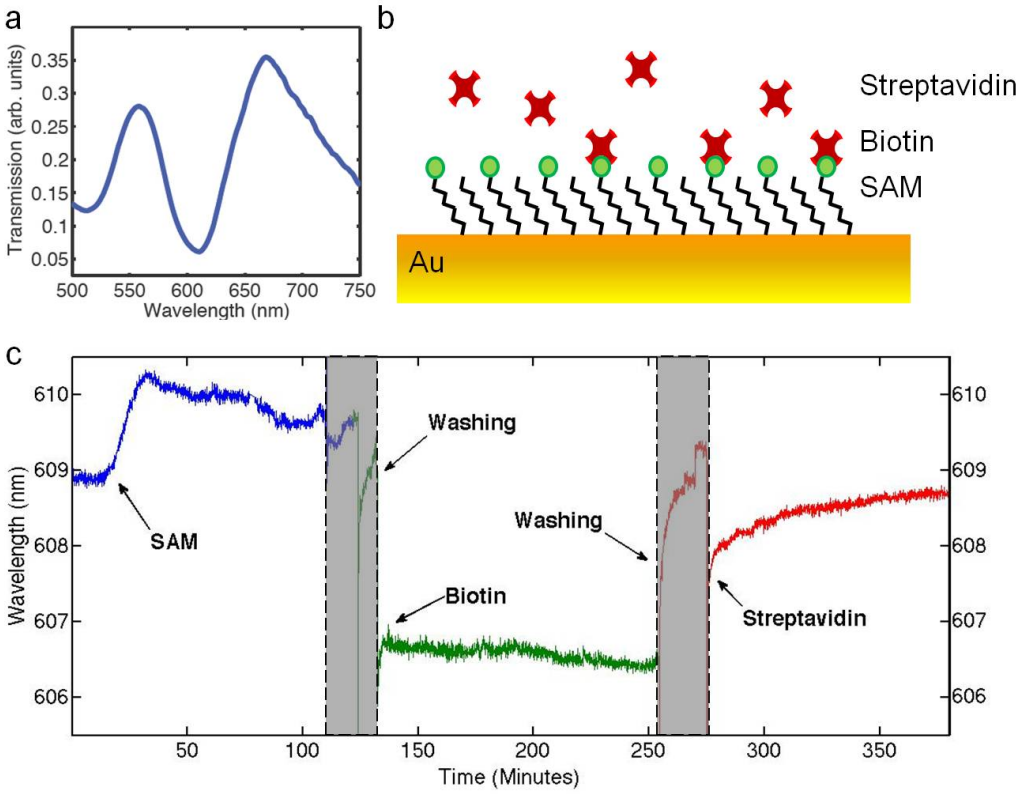

Figure 3.4: **Real-time biosensing of biotin and streptavidin with a nanohole-based SPR sensor.** (a) A representative transmission spectrum of a nanohole array used for the SPR spectral sensing. (b) A schematic showing the molecules used for biosensing. (c) Real-time binding kinetics starting from SAM formation to biotin and streptavidin binding. The grayed-out areas correspond to washing and buffer exchange periods. Figure is adapted from Im *et al.*[27]

nm in water, which corresponds to a bulk refractive index sensitivity of 600 nm/RIU, whereas $\lambda_{sp(1,1)}$ shows a smaller shift of 270 nm/RIU. The bulk refractive index sensitivity of 600 nm/RIU with the double-hole array is larger than the previously reported circular nanohole arrays (400 nm/RIU).[39] The local refractive index sensitivity of the double-hole array for molecular detection was characterized using a SAM of 11-amino-1-undecanethiol, which is about 1.6 nm in thickness with the refractive index of 1.45.[43] After recording the initial transmission spectrum, the double-hole array was incubated in the 4 mM SAM solution for 3 hrs. Another transmission spectrum was measured after the surface was washed by water and dried. Figure 3.5c shows the transmission spectra before and after the SAM formation. With the SAM formed on the Au surface, shifts of $\Delta\lambda_{sp(0,1)} = 6 \pm 1$ nm and $\Delta\lambda_{sp(1,1)} = 3 \pm 1$ nm were measured. In comparison, circular nanohole arrays showed $\Delta\lambda_{sp(0,1)} = 4 \pm 1$ nm from the formation of a monolayer of 11-mercaptoundecanoic acid, which has almost the same thickness as 11-amino-1-undecanethiol.[39] The larger spectral shift indicates that the double-hole array combines attributes of both propagating SPR and LSPR and it improves the sensitivity for both local and bulk refractive index change. Figure 3.5d shows the real-time response of the double-hole sensor exposed to a 0.2 % bovine serum albumin (BSA) solution injected through the flow cell. A transmission spectrum was recorded every 15 s over the course of 1 hr. The response of $\Delta\lambda_{sp(0,1)} = 3$ nm was observed after 1000 sec, when the response nearly saturates. This experiment demonstrates the potential use of the nanohole array in a transmission optical setup to perform real-time, label-free sensing of protein interactions with improved sensitivity. The co-linear transmission optical setup greatly simplifies and miniaturizes optical design and alignment, enabling high-resolution imaging, which is explored in the next chapter.

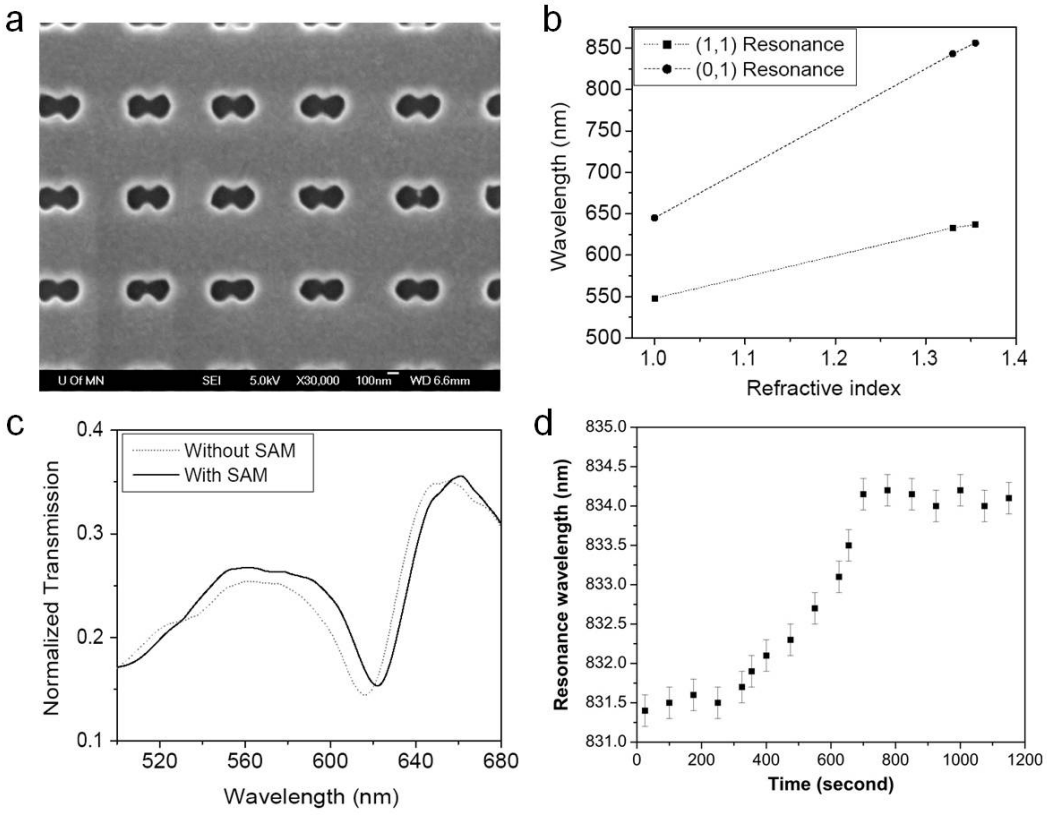

Figure 3.5: **A periodic double-hole array for shape-enhanced plasmon resonance and EOT.** (a) A SEM image of double-hole array with 600 nm periodicity made in a 100 nm-thick gold film. The individual circular holes have a diameter of 200 nm and the center-to-center spacing is 190 nm. (b) Resonance wavelength vs. refractive index of dielectric medium for the (1,1) and (0,1) Bragg resonances. (c) Spectra of the double-hole array with a 600 nm periodicity measured before and after formation of a self-assembled monolayer of molecules on the surface in the air. (d) Real-time sensing of 0.2% bovine serum albumin (BSA) on the gold surface. Figure is adapted from Lesuffleur *et al.*[28]

Chapter 4

SPR Imaging for High-Throughput Biosensing

The SPR technique is a useful tool to study molecular interactions, but SPR sensing that monitors spectral shift of individual areas can only measure a limited number of sensing spots simultaneously. Therefore, development of a new instrumental technique that can characterize multiple interactions simultaneously is desired. Characterizing unknown samples or new drug candidates requires studies of cross-reaction with multiple ligand-receptor pairs. Like a protein microarray which is built to screen thousands of protein-protein interactions using colorimetric detection methods, a high-throughput screening technique becomes essential for many practical applications. This chapter describes a SPR imaging technique that is designed for high-throughput parallel detection of molecular binding in a label-free manner. Combining the SPR imaging with plasmonic nanohole arrays provides multiplexing capability aimed at achieving massively parallel kinetic assays using densely packed sensing elements. The results of nanohole-based SPR imaging described in this chapter are mainly derived from the following publications:

1. H. Im, A. Lesuffleur, N. C. Lindquist, and S. H. Oh, *Analytical Chemistry* **81**, 2854 (2009).[44]

2. N. C. Lindquist, A. Lesuffleur, H. Im, and S. H. Oh, *Lab on a Chip* **9**, 382 (2009).[45]

3. A. Lesuffleur, H. Im, N. C. Lindquist, K.-S. Lim, and S. H. Oh, (invited paper) in *Proceedings of SPIE* **7035**, 703504 (2008).[46]

4. A. Lesuffleur, H. Im, N. C. Lindquist, and S. H. Oh, *Optics Express* **16**, 219 (2008).[47]

4.1 High-Throughput Screening

Recent advances in protein microarray technology show promise for high-throughput studies of thousands of protein-protein interactions with high spatial density.[48,49] Existing protein microarray technology has mostly relied on uorescent or radioactively labeled molecules. As described in Chapter 3, avoiding the use of labels is highly desired since it is a time-consuming process and often affects a molecules binding properties. Therefore, it is a logical step to develop label-free kinetic SPR sensing in a microarray format. Furthermore, the high density microarray-type SPR technology can dramatically accelerate the accumulation of binding information about protein-protein and protein-nucleic acid interactions. As described in Chapter 3, the Kretschmann setup has been used successfully in the commercial BIAcore^{TM} instruments for relatively low-throughput experiments. However, the bulky coupling prism sharply tilts the detection plane from the sample plane. If the Kretschmann setup is coupled with an imaging sensor for high-throughput experiments, the image of the sample surface is projected on the sensor surface with a large tilt angle, leading to defocusing and optical aberrations, prohibiting the use of high numerical aperture (NA) imaging lenses and limiting the available field-of-view.[50] This limits the size of a microarray that can be imaged with high quality. Another commercial instrument, Flexchip^{TM} also from GE healthcare,[51] instead utilizes a higher order diffracted mode of a grating coupler for SPR excitation and can measure binding kinetics from 400 sample spots simultaneously. However, the

issues associated with a tilted image plane still persist, and its high cost is a barrier to widespread use. To achieve the ambitious goal of proteome-scale label-free kinetic assays, a new class of SPR instrument is needed that combines (1) high imaging resolution to collect kinetics data from individual spots on high density microarrays; (2) massively parallel multiplexing capability with a large field-of-view; and (3) a simple and robust optical design.

4.2 SPR Imaging with Plasmonic Nanohole Arrays

In contrast to conventional SPR instruments based on a reflection mode, the nanohole array-based SPR sensor operates in transmission mode based on the EOT effect through the sub-wavelength apertures in a gold film from normal incident light. This co-linear optical transmission setup offers several key benefits in cost and simplicity in the optical setup. Especially important are that the signal can be measured with normally incident optical geometry, enabling high imaging resolution, easy optical alignment, and a large field-of-view, all of which are critical for high-density protein microarray applications.

4.2.1 Principle of SPR imaging

In spectrum-based SPR sensing, as described in Chapter 3, molecular binding to the sensing surface induces a spectral shift of the resonance peak, and real-time binding kinetics are measured by monitoring the spectral shifts. When the spectrum shifts the transmitted light intensity at a fixed wavelength changes, as depicted in Figure 4.1. While the spectrum measurement setup uses a broadband light source and a spectrometer to record a transmission spectrum of transmitted light through the nanohole array, SPR imaging uses a laser source at a fixed wavelength and a CCD detector to monitor the intensity change at the wavelength of the laser. (Figure 4.1b) In Chapter 3.1, the variation of the effective refractive index due to the presence of a thin film on the SPR sensing surface was theoretically obtained using a weighted average in the evanescent

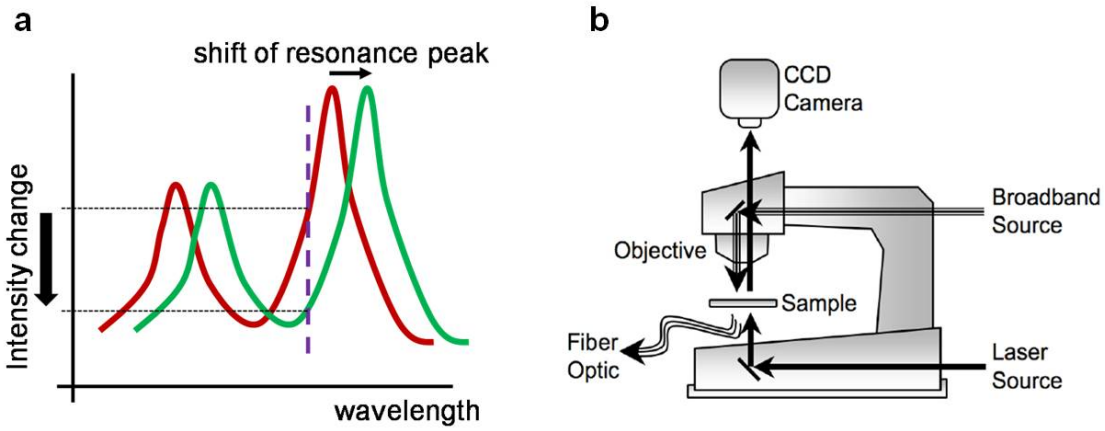

Figure 4.1: **Principle of SPR imaging and its optical setup.** (a) A diagram showing the principle of SPR sensing with the SPR imaging technique. Molecular binding to the sensing surface induces a spectral shift of resonance peak, which changes the transmitted light intensity at a fixed wavelength. Therefore, molecular binding events can be measured from multiple arrays simultaneously by monitoring the intensity changes rather than spectral shifts. (b) Optical setup for SPR imaging with a standard upright microscope. For a spectral measurement, a broadband white light source is used to illuminate a nanohole array through a microscope objective and the transmitted light is collected by a fiber optic cable connected to a spectrometer. In SPR imaging, a laser source is used to illuminate multiple nanohole arrays with a constant light intensity at a fixed wavelength and the transmitted light is collected by a microscope objective and imaged on a CCD camera. Figure is adapted from Im *et al.*[44]

field (Equation (3.3)). From the equation (3.1), the SPR response of nanohole array is then given by the spectral shift of transmission peak, which is proportional to the spectral sensitivity (m) and the refractive index change (Δn_{eff}). For SPR imaging the variation of the transmitted intensity (I_T) at a fixed detection wavelength is given by:[47]

$$\Delta I_T = -\frac{dI_T}{d\lambda} \cdot m(\Delta n_{eff}) \, . \tag{4.1}$$

The Equation (4.1) indicates the sensitivity for laser-based SPR imaging not only depends on the spectral sensitivity, but also on the slope $dI_T/d\lambda$, which corresponds to the sharpness of the resonance peak. The negative sign in Equation (4.1) means that

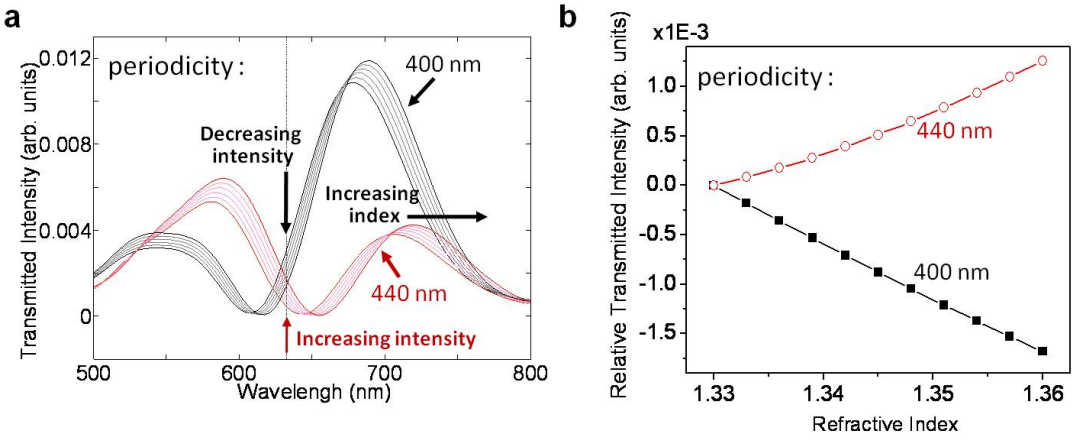

Figure 4.2: **Computer simulations of SPR imaging with EOT.** (a) The transmission spectra of nanohole arrays with 400 nm (black lines) and 440 nm (red lines) periodicities incubated in various media with refractive indices varying from 1.33 to 1.36. (b) Depending on the sign of the slope of the transmitted spectra at the illumination wavelength used, in this case 633 nm for a HeNe laser, the intensity either decreases for 400 nm periodicity (black lines) or increases for 440 nm periodicity (red lines) as the refractive index increases. The intensities for both periodicities at $n = 1.33$ are shifted to zero for comparison. Figure is adapted from Im *et al.*[44]

the transmitted intensity decreases with a red-shift of the peak when the laser wavelength is on the left side of a peak where the slope is positive as shown in Figure 4.1a. Figure 4.2 shows 3-D FDTD computer simulations of transmission spectra from two nanohole arrays with periodicities of 400 and 440 nm as the refractive index of the surrounding medium changes from 1.33 to 1.36 with a step of 0.01. As the refractive index increases, the transmission peak red-shifts, per equation 3.1, and the transmitted intensities of nanohole arrays changes at the fixed wavelength of laser, per the Equation (4.1). Depending on the periodicity of nanohole array and the laser wavelength, the transmitted intensity can either linearly decrease (400 nm periodicity) or increase (440 nm periodicity) at a fixed illumination wavelength, in this case 633 nm for a HeNe laser,

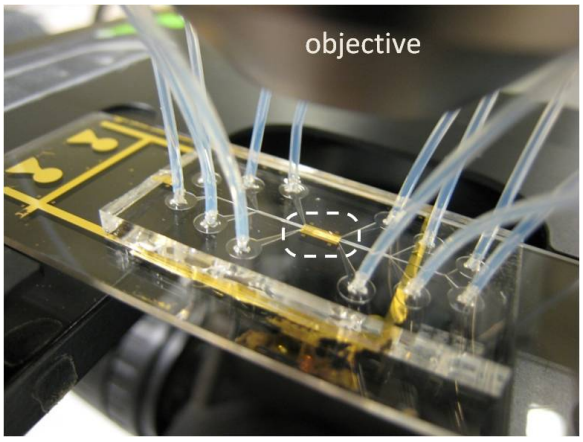

Figure 4.3: **Photograph of a nanohole array device for SPR imaging.** A complete ready-to-use device consists of a patterned gold-coated glass slide with an integrated PDMS microfluidic flow cell with 6 channels, mounted on a microscope stage. Teflon tubes are connected inlets and outlets of channels for delivering various solutions to each channel. Figure is adapted from Im *et al.*[44]

as the refractive index increases from 1.33 to 1.36. This is due to the sign of the slope of the transmission peak at the illumination wavelength: positive for a periodicity of 400 nm (therefore decreasing intensity) and negative for a periodicity of 440 nm (increasing intensity). As described earlier, for SPR imaging, the sensitivity of the nanohole arrays depends both on the spectral shift due to the refractive index change and on the slope of the transmission peak at the illumination wavelength. Therefore, it is important to design a nanohole SPR sensor with a proper periodicity where the illumination wavelength lies directly at the largest slope of the peak in the transmission spectrum.

4.2.2 SPR imaging setup

Figure 4.3 shows a complete ready-to-use device, consisting of a patterned gold-coated glass slide integrated with a PDMS microfluidic flow cell, mounted on an upright microscope stage. The nanohole array device is prepared through similar fabrication procedures described in Chapter 3. E-beam evaporation was used to deposit a 200 nm-thick Au film with a 5 nm Cr adhesion layer on cleaned glass slides and FIB was used to pattern arrays consisting of 16 $\times$ 16 nanoholes with a footprint of about 40 μm^2. Nanohole arrays were arranged in 6 rows and the nanohole array chip was aligned with a 6 channel-PDMS microfluidic flow cell. Teflon tubing connected to the fluidic channels allows addressing nanohole arrays with various solutions, *e.g.* various concentrations of analytes.

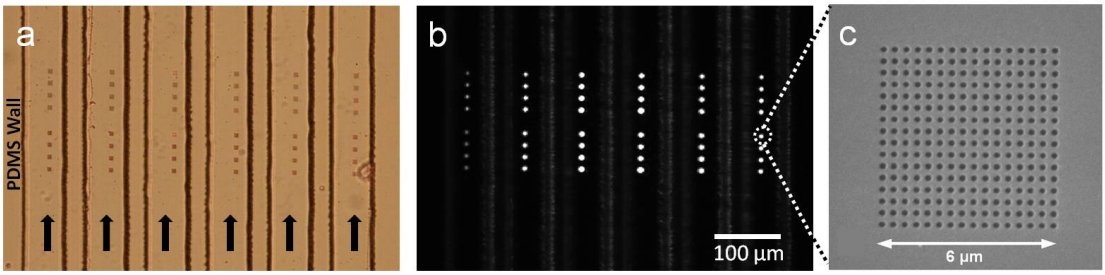

Figure 4.4: **Multichannel SPR imaging with nanohole arrays.** Microscope images of nanohole arrays aligned with 6 parallel microfluidic channels, allowing the delivery of various solutions to each group of nanohole arrays. (a) A bright field image in a reflection mode. (b) A transmission-mode image, illuminated from below with a 633 nm HeNe laser beam. (c) A SEM image of one of the nanohole arrays, consisting of 16 $\times$ 16 nanoholes in 6 μm $\times$ 6 μm. Each nanohole is 150 nm in diameter. Figure is adapted from Im *et al.*[44]

For SPR imaging, a HeNe laser at 632.8 nm was used to illuminate the nanohole arrays from below, through the glass substrate, exciting surface plasmons, and the transmitted light through the nanohole arrays were collected using a 10$\times$ microscope objective (NA = 0.30) and imaged using a CCD camera. Figure 4.4 shows microscope

images of nanohole arrays aligned with a six-channel PDMS flow cell. In each channel, eight nanohole arrays with different periodicities were tested to determine the optimal array periodicity for SPR imaging with the HeNe laser. Multichannel devices are required to perform multiplex experiments with various concentrations and molecules with negative controls. A custom-built MATLAB suite of analytical and signal processing codes were used to control the CCD camera, capture image fies at regular time intervals, and process the image data to extract intensity profies of individual nanohole arrays during the kinetic measurements.

4.2.3 Optimization of nanohole periodicity

Figure 4.5a shows real-time experimental measurements of the transmitted intensity through nanohole arrays with different periodicities ranging from 390 to 420 nm. Mixtures of water and ethanol in varying ratios with refractive indices from 1.333 to 1.353 with a 0.005 step are sequentially injected. As the refractive index varies, the transmitted intensity linearly changes with each refractive index step, however the the magnitude of change is different depending on the periodicity of array. For the array with 420 nm periodicity, the transmission intensity changes little as the refractive index of solution changes, while the nanohole array with 400 nm periodicity shows the largest intensity changes. Similarly, the sensitivity dependence on the periodicity of array is seen with biotin-streptavidin binding events as shown in Figure 4.5b. The difference in the SPR imaging sensitivity of nanohole arrays with different periodicities is directly related to the slope of transmission peak at the laser wavelength as described in the Equation (4.1). The nanohole array with the 400 nm periodicity shows larger intensity response from the refractive index changes than arrays with other periodicities because the laser wavelength of 633 nm is located at the transmission resonance region with the highest slope. For the array with 420 nm periodicity the transmitted intensity remains fairly flat with changes in refractive index because the laser wavelength is at the minimum of transmission where the slope is close to zero. Therefore, it is important to tune the

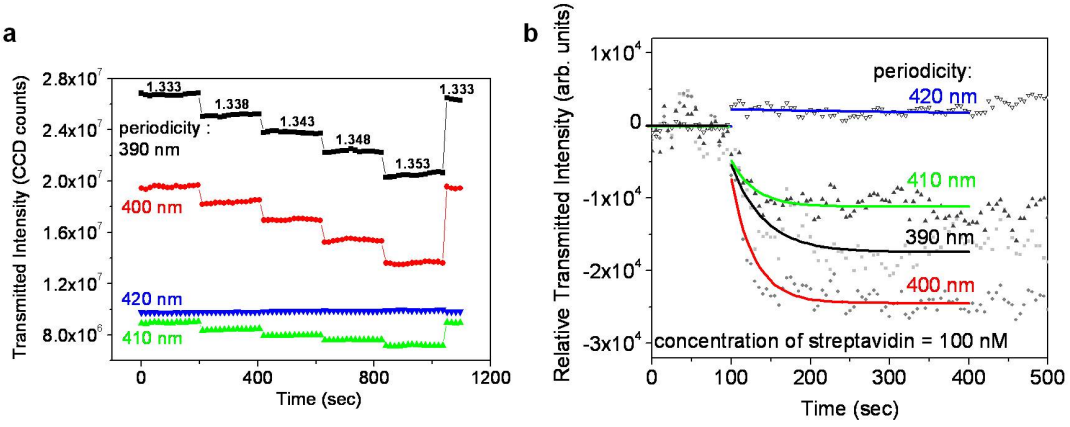

Figure 4.5: **Real-time SPR imaging of nanohole arrays with different periodicities.** Continuously measured transmission intensity with nanohole arrays with periodicities ranging from 390 to 420 nm as the bulk refractive index changes from 1.333 to 1.353 in steps of 0.005. (b) Real-time measurements of binding kinetics between streptavidin and biotin. The concentration of streptavidin is 100 nM. As more streptavidin binds to biotin, the intensity decreases for periodicities of 390, 400, and 410 nm, while it remains relatively unchanged for a periodicity of 420 nm. Figure is adapted from Im *et al.*[44]

nanohole array periodicity to position the laser wavelength at the region of the greatest slope in the transmission spectrum in order to achieve the highest sensitivity.

4.2.4 Parallel kinetic assays and differential sensing

In SPR measurements of ligand-analyte binding, it is important to perform separate control experiments to rule out non-specific binding of the analyte onto the gold surface and to correct the response for bulk refractive index differences between solutions. This is especially important when a high concentration of analyte is injected, a common condition for measuring very weak interactions. The bulk refractive index difference and non-specific adsorption can be significant, causing a large shift in the measured SPR signal as well as response from specific binding events. It should be noted that

in a nanohole SPR sensor, light transmission is measured through a liquid flow cell. Therefore, it is also necessary to measure the light absorption in the sample solution. It is important to rule out these artifacts by measuring responses from channels of both positive and negative controls using the same analyte solutions in order to precisely quantify the binding affinity from the measured kinetic curve. This differential sensing scheme can also eliminate background fluctuation caused by temperature, source intensity, and vibration. In our multichannel platform, each microfluidic channel can be functionalized with a different type of molecule which can subsequently interact with different analytes, allowing concurrent measurements of positive/negative controls and analytes of varying concentrations. To investigate the detection limit of the sensor for biotin-streptavidin binding, different concentrations of streptavidin solution were injected into parallel channels including corresponding reference channels, which do not have immobilized biotin.

Figure 4.6 shows binding kinetics measured for different concentrations of streptavidin (20, 30, 50, and 100 nM) from nanohole arrays with a 400 nm periodicity. The transmitted intensity decreases, at saturation, by 6.5 %, 8.9 %, and 18.8 % for concentrations of 30, 50, and 100 nM, respectively. The red curves show exponential decaying fits to the measured data for each concentration, following binding responses based on a simple biomolecular reaction model.[52] Calculations based on the data presented in Figure 4.6a gives the dissociation constant, K_D, to have a value of 4.12×10^6 M^{-1}. This value is fairly close to a previously reported value[52] of 7.3×10^6 M^{-1}. As the concentration of streptavidin goes below 20 nM, the transmitted intensity change is comparable to the noise level, making it difficult to accurately fit a curve. Figure 4.6b shows differential sensing of streptavidin and biotin binding kinetics using two neighboring microfluidic channels. The net binding kinetics between streptavidin and biotin was obtained by subtracting response in the reference channel, which does not have immobilized biotin, from the data obtained in the positive sample channel functionalized with biotin. 100 nM streptavidin solutions were injected to both positive and reference

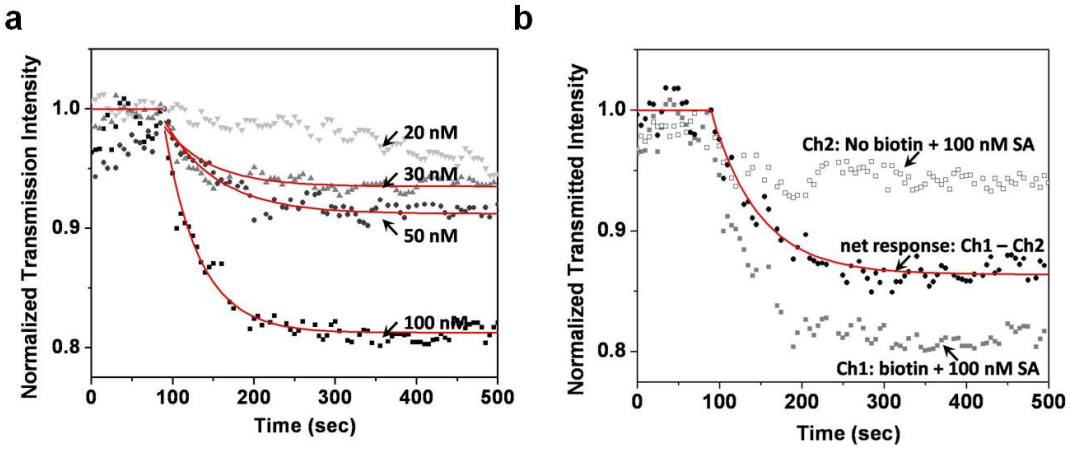

Figure 4.6: . (a) Real-time streptavidin-biotin binding kinetics measured for different concentrations of streptavidin (20, 30, 50, and 100 nM) binding to immobilized biotin. The measured data are fit to curves based on a simple bimolecular binding model (A + B = AB). (b) Real-time differential sensing of streptavidin and biotin binding kinetics is obtained by subtracting the response of negative channel in an absence of biotin from the response of positive channel where biotin is immobilized. 100 nM streptavidin solutions are simultaneously injected to two neighboring microfuidic channels separated by 100 μm at the same flow rate of 2 μl/hr. Figure is adapted from Im *et al.*[44]

channels at a ow rate of 2 μl/h. The transmitted intensity change from the reference channel is 5 – 7 %. This is due not only to nonspecic bindings of streptavidin onto the Au surface but also due to the bulk refractive index change. The multichannel platform is able to simultaneously measure binding kinetics with different concentrations with corresponding negative controls, enabling differential sensing of binding kinetics while removing experimental artifacts.

4.2.5 Microarray application with plasmonic nanohole arrays

Figure 4.7 shows a microarray of 252 sensing elements wherein the nanohole arrays are grouped as 3 × 3 subarrays with different periodicities ranging from 370 to 450

nm. The center-to-center distance between each array is 8 μm, which gives the packing density of 1.45×10^6 arrays per cm^2. Bragg mirrors surrounding the nanohole arrays enables to achieve even higher packing density with sub-1-μm sized nanohole arrays and shorter spacing between the arrays.[45] The transmitted intensities vary depending on the periodicity of nanohole array. The enlarged image of a 3×3 subarray is shown in Figure 4.7b. Each row, consisting of three sensing elements, has the same periodicity, which is varied by 10 nm for each row. Figure 4.7c is an SEM image of the nanohole arrays. Each sensing element consists of a periodic array of 7×7 nanoholes. This nanohole array based SPR imaging technique demonstrates the possibility of packing the nanohole array sensing elements at a density for microarray application. The combination of multiplex SPR sensing using a simple microscope setup with differential sensing for accurate quantifiation shows promise for using this platform for high-throughput studies of protein-protein interactions on protein microarrays.

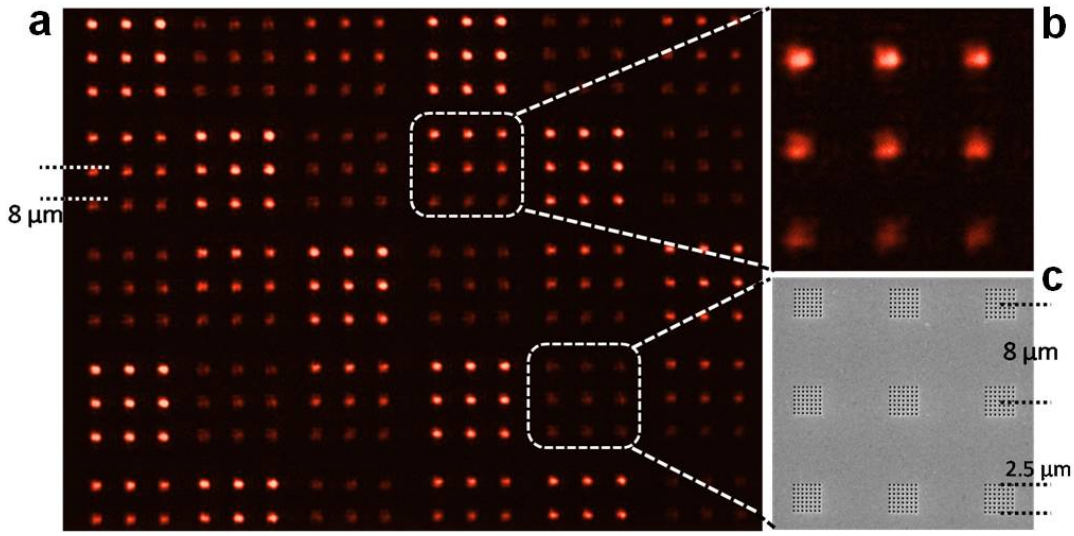

Figure 4.7: **High-resolution SPR microarray imaging.** (a) A transmission image of a large microarray with 252 nanohole arrays, each one separated by 8 μm. The arrays are grouped as 3 $\times$ 3 subarrays, where each subarray has three different periodicities ranging from 370 to 450 nm, giving different transmission intensities. (b) Enlarged image of a 3 $\times$ 3 subarray. Each row has the same periodicity, which varies by 10 nm for the next row. (c) SEM of one of the 3 $\times$ 3 subarrays. Each nanohole array consists of 7 $\times$ 7 nanoholes, each with a diameter of 150 nm. Figure is adapted from Im *et al.*[44]

Chapter 5

SPR Biosensing with Lipid Membranes

Examining interactions between molecules and proteins embedded in lipid bilayers are of particular interest to biomedical researchers. In fact half of the 100 best selling drugs target membrane-bound proteins.[6] Accordingly, the ability to investigate molecular interactions on lipid membranes is of great importance for fundamental research as well as new drug discovery.[7] However, membrane-bound proteins are not easily manipulated in solution and do not maintain their three-dimensional sructure when removed from membranes, making it difficult to study and characterize them with conventional SPR sensing techniques. Therefore, there is a critical need for development a sensing platform to quantitatively analyze membrane-bound proteins and receptors in a lipid membrane environment. In this chapter, methods for the formation of supported and suspended lipid membranes over nanopore SPR biosensors, characterization of the membrane formation, and real-time binding kinetics of antibodies to membrane-bound proteins in lipid membranes are described. The results shown in this chapter are derived in part of the following publication:

1. H. Im, N. J. Wittenberg, A. Lesuffleur, N. C. Lindquist, and S. H. Oh, *Chemical*

Science, **1**, 688-696 (2010).[53]

5.1 Introduction to Lipid Membranes

Lipid membranes are crucial biological structures that define the boundaries of cells and subcellular organelles. Lipid membranes are largely to water-soluble molecules and along with membrane-bound ionic pumps, maintain the chemical and ionic gradients across plasma and organelle membranes. These membranes are composed of a variety of lipids, such as phospholipids, sphingolipids, glycolipids, and cholesterol, to name a few, and are decorated by a number of sugars and membrane-bound proteins.

Phospholipids are major components of cell membranes and consist of a hydrophilic head with two hydrophobic tails as shown in Figure 5.1. Depending on the presence of carbon-carbon double bonds in the tails, phospholipids are classified as saturated or unsaturated lipids. Unsaturated lipids have carbon-carbon double bonds that affect the physical properties of lipid membranes such as the packing density and phase transition temperature. Because phospholipids are amphiphiles (contain both hydrophilic and hydrophobic sections), phospholipids will self-assemble in an aqueous environment. In an aqueous solution, phospholipids self-assemble into a thin sheet of two layers where hydrophilic heads of two layers are facing out toward water and hydrophobic tails are facing toward inside of the sheet. These sheets of two monolayers are known as lipid bilayers, as shown in Figure 5.2. Phospholipids can also exist as spherical structures called vesicles or micelles. Furthermore, these membranes contain numerous peptides and proteins that decorate the membrane surfaces or span across the membrane. The physiological basis for many diseases and conditions can be traced to irregularities in the cell membranes themselves or with membrane-bound proteins. For this reason, many therapeutic antibodies and drug molecules target membrane-bound proteins.[6]

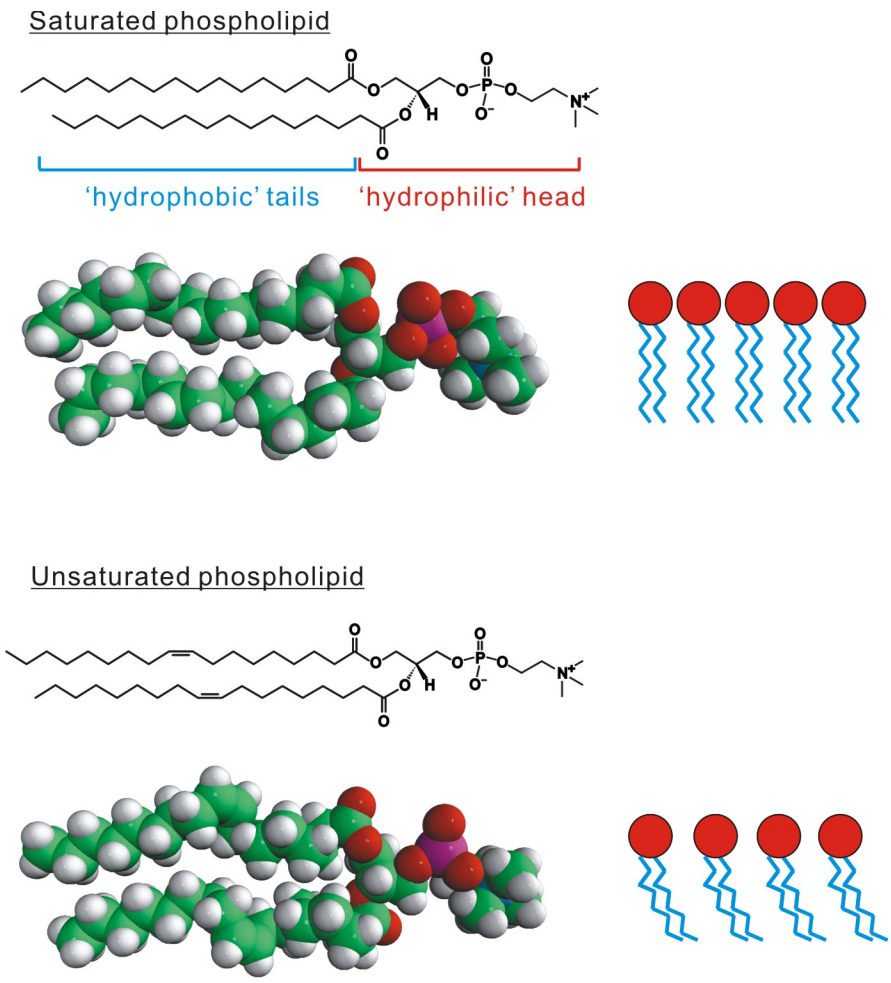

Figure 5.1: **Phospholipids.** Phospholipids consist of hydrophilic head and hydrophobic tail groups. Depending on the presence of the carbon-carbon double bonds in the tail group they are classified as saturated or unsaturated lipids. Structures of 1,2-dipalmitoyl-sn-glycero-3-phosphocholine (DPPC) and 1,2-dioleoyl-sn-glycero-3-phosphocholine (DOPC) are shown as examples of saturated and unsaturated lipids, respectively. Structures and 3-D models are provided by Avanti Polar Lipids, Inc.

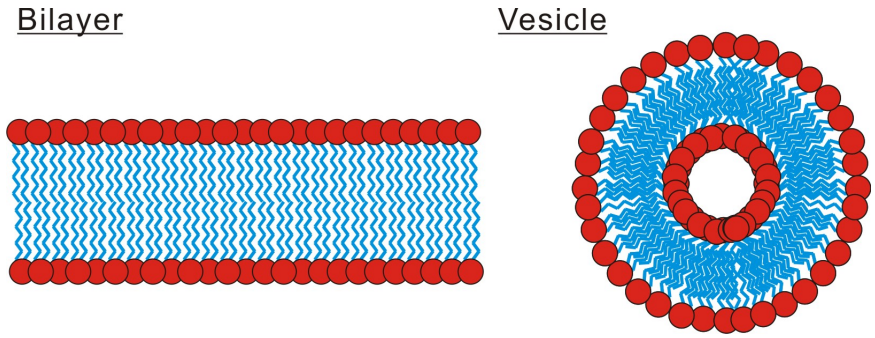

Figure 5.2: **Shapes of phospholipids.** In an aqueous solution, phospholipids can self-assemble into planar bilayers, spherical vesicles or micelles due to the strong polarity of the heads and tails.

5.1.1 Formation of lipid bilayers

In order to interface lipid membranes with biosensors, many groups have employed supported lipid bilayers (SLBs) or black lipid membranes (BLMs).[54] A SLB is a planar lipid bilayer membrane formed directly on a solid substrate, whereas a BLM is a planar lipid bilayer membrane that is suspended over a small aperture in a solid substrate. SLBs have been employed in a number of biochemical and biophysical studies on the fundamental properties of lipid membranes.[55–59] For SLBs, the lipid bilayer is directly formed on a solid substrate with an underlyng water layer ($\sim 1-2$ nm thick) as depicted in Figure 5.3a. While SLBs are often used to study physical properties of lipid bilayers because of their long-term stability, steric hindrance due to the presence of underlying substrate often makes incorporation of integral proteins challenging and those proteins that are inserted can be denatured.[60,61] Also the diffusion mobility of lipids in the bilayer is about 2.5 times slower compared to a suspended lipid bilayer due to surface interaction between lipids and underlying substrate.[62] The lower lateral mobility of the lipid bilayer can affect the binding property of certain types of molecules that bind to multiple components in the membrane.[63] In order to overcome these issues, polymer cushions can be placed between the layer and the substrate Figure 5.3b or linker

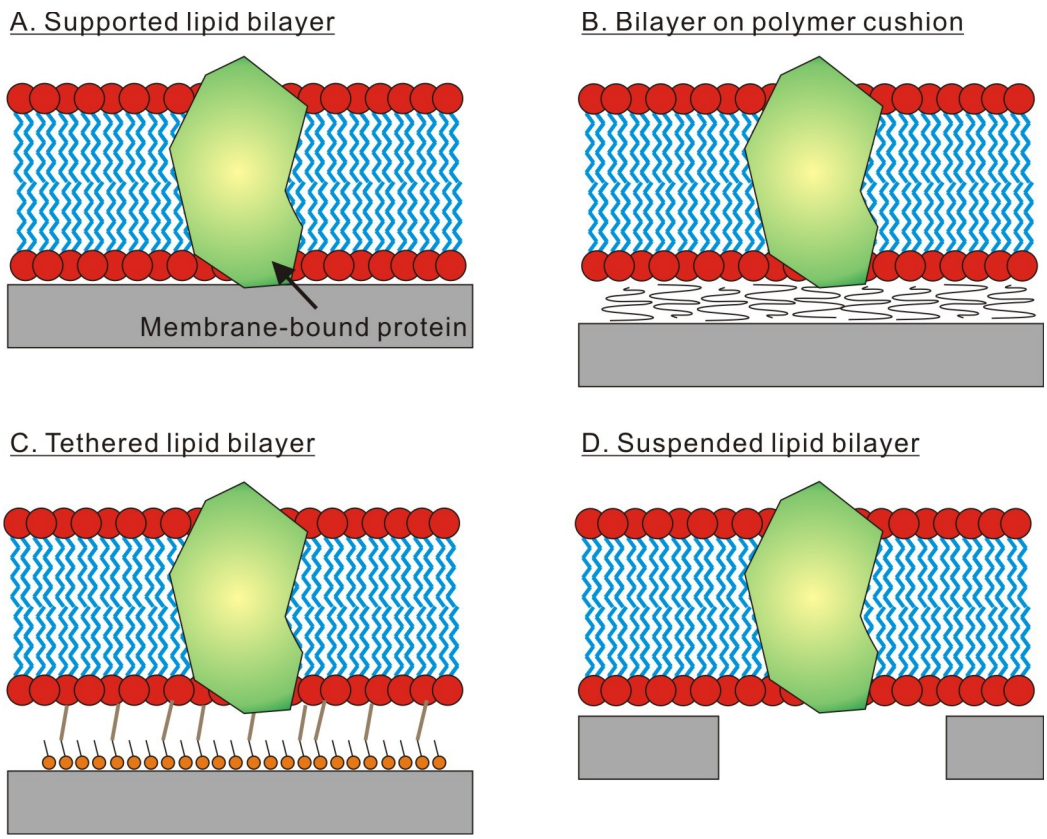

Figure 5.3: **Formation of lipid formation on solid-state substrates.** (a) Supported lipid bilayers can be formed directly on a hydrophilic surface. However, due to the presence of the underlying solid substrate and direct contact with the surface, membrane-bound proteins in the bilayers can be denatured. In order to resolve the issue, lipid bilayers formed on (b) polymer cushions or (c) tethered lipid bilayers are used. (d) A suspended lipid bilayers, also called as a black lipid membrane (BLM), is a way to mimic a natural cell membrane without the interference of the underlying substrate.

molecules can be used form tethered lipid bilayers Figure 5.3c. In another conformation, suspended lipid bilayers, also called a black lipid membrane (BLM), are formed across apertures or patterns in free-standing films or high-aspect ratio patterns as depicted in Figure 5.3d. This form better mimics real celluar membranes where both sides of the lipid membranes are in contact with aqueous environments than SLBs wherein only one side is accessible. To form lipid planar bilayers, several methods including painting[64,65] Langmuir-Blodgett,[66,67] vesicle rupture,[55] and other techniques.[68–70] have been developed. In the painting method, a drop of organic solvent containing dissolved lipids is introduced on the substrate surface immersed in an aqueous solution. When the solvent is removed, the lipids assemble into a bilayer on the substrate. This method is often called as painting because a soft brush is often used to deliver the lipid containing solvent to the surface. In the Langmuir-Blodgett method, the amphiphilic lipids are dispersed at a water-air (sometimes water-oil) interface by surface tension between the lipids and their surrounding environment. Then the substrate is slowly translated through the interface to form a lipid bilayer. With a hydrophilic substrate, the substrate is first pulled from the solution to the air, forming a monolayer of lipid as the substrate moves away from the solution. Then, the substrate is vertically inserted into the solution, depositing a second monolayer on top to form a lipid bilayer on the substrate. In the vesicle rupture method, an aqueous buffer solution containing unilamellar lipid vesicles is introduced onto a hydrophilic substrate and vesicles rupture upon contact with the surface. The vesicle rupture occurs simultaneously on some hydrophilic surfaces to form lipid bilayers. Vesicles can also rupture on hydrophobic surfaces, *e.g.* a pre-formed hydrophobic self-assembled monolayer with alkyl groups, but in this case they fuse into lipid monolayers and form hybrid bilayers where one side of bilayer is made by the SAM layer and the other side is made by the lipid monolayer. Among these methods, forming lipid vesicles and rupturing them on the surface is one of the most widely used methods because it is a solvent-free method that is compatible with lipid membranes containing membrane-bound proteins. The vesicle rupture pathway, while somewhat dependent on

the lipid composition and the nature of the substrate, proceeds through the following general steps. First, a small number of vesicles adsorb to the surface. Then when a certain number of vesicles populate the surface, they begin to rupture, forming a SLB.[71] The surface interaction between lipid vesicles and substrate is a key parameter to make the vesicles rupture while in some cases the rupture can be aided by adding Ca^{2+} ions in the buffer solution.[72] A variety of hydrophilic substrates, such as glass and SiO_2 are compatible with vesicle rupture to form lipid bilayers.

5.1.2 Characterization of lipid bilayers

Fluorescence recovery after photobleaching (FRAP) is a technique that quantifies the two-dimensional lateral diffusion of lipid components on the membrane and is widely used to characterize the formation of supported or suspended lipid bilayers. When fluorescent dyes are incorporated into lipids in lipid bilayers, they can freely diffuse around because of the lateral fluidity of lipid bilayers. In FRAP experiments, as shown in Figure 5.4 a small circular area of membrane is photobleached with an intense laser beam. Diffusion of unbleached fluorescence dyes back into the previously bleached area indicated the formation of a continuous lipid membrane layer.

Quantitatively, the diffusion coefficient (D) for lipid membranes can be calculated using the following equation:

$$D = \frac{R^2}{4\tau_D} \tag{5.1}$$

where R is the radius of the photobleached spot and τ_D is the characteristic diffusion time obtained from the fluorescence recovery curve.[74,75] From the recovery curve with the known size of photobleached area, the lateral mobility of lipid bilayer is calculated. The lateral mobility varies depending on lipids, substrates, and lipid structures,[76] and the diffusivity for suspended bilayers is about 2.5 times faster than supported bilayers.[62] In addition to the uniform fluorescence intensity, the lateral diffusion mobility of lipids in the membrane from the FRAP measurement confirms the formation of continuous lipid bilayer on the substrate. Lipid membranes and their formation process can be

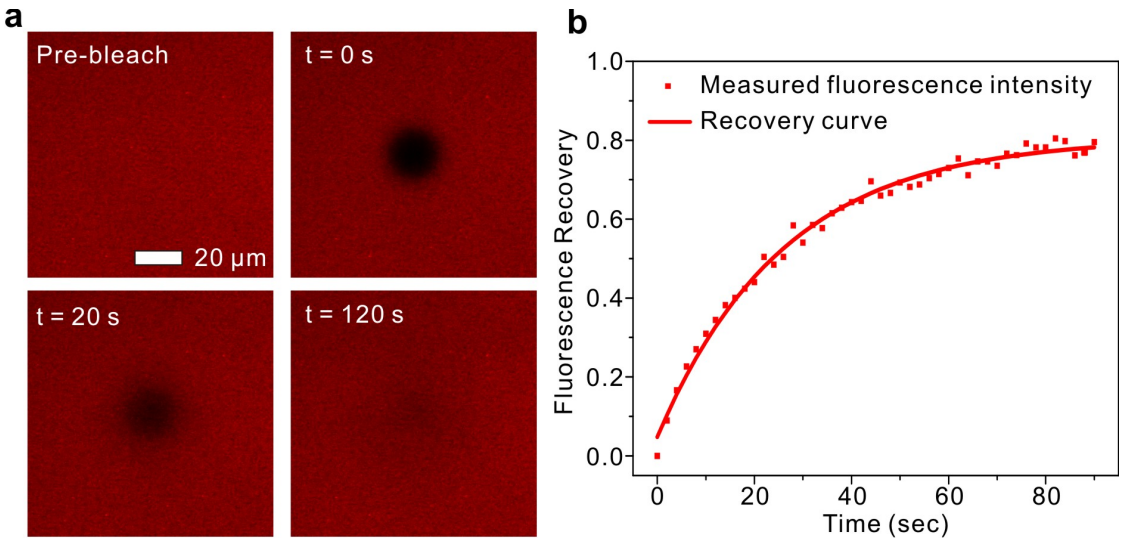

Figure 5.4: **Fluorescence recovery after photobleaching (FRAP).** (a) Frames from a FRAP experiment with an L-α-phosphatidylcholine (egg PC) lipid membrane on the silica surface. The time of recording each frame is indicated in the top left corner. At time t = 0, a circular area of membrane is photobleached. (b) Representative FRAP recovery curve for an egg PC membrane on the flat silica surface. Figure is adapted from Im *et al.*[73]

also characterized by electrochemical impedance spectroscopy (EIS). In an equivalent circuit model, lipid membranes can be represented as a capacitor with capacitance in the range of 0.5 – 1.0 μF/cm^2 and a resistor with resistance in the order 10^5 – 10^7 Ω cm^2 connected in parallel.[77,78] Those values can be calculated by measuring impedance and phase difference before and after forming lipid membranes in the frequency range of 10^{-2} – 10^6 Hz. The formation of a single lipid bilayer is directly determined from the thickness of lipid membranes calculated from its capacitance. Atomic force microscopy (AFM) has been used to study physical properties and stability of BLMs formed on porous substrates.[79,80] It has also been used to image the distribution of lipid domains or lipid rafts,[81] wherein the local concentration of certain types of lipids, especially cholesterol, is enriched.

5.2 Plasmonic Biosensing with Supported Lipid Bilayers

In cell membranes, lipid bilayers are decorated with various types of membrane-bound proteins which act as receptors that respond to certain molecules in the external environment. Whereas the lipid bilayer is selectively permeable to polar molecules and ions enabling it to maintain the chemical gradients between intra- and extra-cellular environments, binding of specific molecules to the membrane receptors can trigger a cascade of biological reactions.[82] Because membrane-bound proteins are so heavily involved in cell signaling, almost 50 % of the drug molecules currently available on the market target membrane-bound proteins.[6] Therefore, studying specific molecular binding to the receptors residing in the membrane is important for the discovery of potential new drug molecules as well as understanding basic mechanisms of molecular recognition. An important example of a disease that could be potentially treated with membrane-binding drugs is multiple sclerosis (MS). MS is a disease in the central nervous system, which consists of the brain and the spinal cord.[83] In MS, myelin sheaths covering and protecting axons are damaged, leading to demyelination and eventually neuronal injuries.[83] Myelin electrically insulates axons and facilitates fast signal transduction. Damaged myelin interferes with the communication between the brain and the rest of body and causes a number of symptoms.[84] MS can affect vision, speech, sensation, physical activities, and bowel control. Unfortunately, there is no cure for MS and currently available treatments are limited to reducing the rate of damage.[84] Our collaborators in this work, Dr. Moses Rodriguez and coworkers at the Mayo Clinic have discovered *immunoglobulin* M (IgM) antibodies that bind to the surface of oligodendrocytes and promote myelin re-growth, preventing continued neuronal loss.[85,86] Oligodentrocytes are the cells in the central nervous system that produce the myelin sheaths that insulate axons. They discovered that well-characterized monoclonal mouse antibodies, IgM O1 and O4, promote remyelination in mouse models of multiple sclerosis.[85] Studies based on immunofluorescence techniques showed that the IgM O1 and O4 presumably bind to galactocerebroside

and sulfatide containing membranes, respectively.[87] Galactocerebroside and sulfatide are lipids present in myelin membranes. Unfortunately, little is known about the binding kinetics and affinities of IgM O1 and O4 Determining their binding kinetics of IgM O1 and O4 for their identified antigens in lipid membranes provides essential information to understand binding behavior of other remyelination promoting antibodies, to identify their unknown antigens, and eventually to understand the mechanism of the remyelination process.

5.2.1 Nanopore SPR sensors with supported lipid bilayers

To characterize binding kinetics of IgM O1 and O4, supported lipid bilayers (SLBs) containing 2 % sulfatide (SUL) and galactrocerebroside (GalC) mixed with L-α-phosphatidylcholine (egg PC) were formed on plasmonic nanopore SPR sensors. As discussed in Chapter 5.1.1, even though SLBs may not be suitable to study some transmembrane proteins due to the proximity to the underlying solid substrate, they are still useful to study antibodies that recognize small lipid-based receptors residing on the lipid membrane surface. Furthermore, the long-term stability of SLBs enables measurement of a number of binding interactions on the same lipid bilayer. In this work the vesicle rupture technique was used to form SLBs on the nanopore SPR sensors, which were prepared using nanoimprint lithography with a gold-coated glass slide. Refer to Chapter 6 and Appendix B for the detailed fabrication process of the nanopore sensor. To form a lipid bilayer on the nanopore array, the hydrophobic Au sensing surface needs to be rendered to hydrophilic. In this work, a 12-nm-thick hydrophilic silica layer is uniformly coated on the Au surface using atomic layer deposition (ALD). ALD provides a thin conformal layer with precise control of film thickness and good uniformity over a large area. Detailed information of ALD is described in Appendix A. The silica-coated Au nanopore SPR sensor is then assembled with a 12-channel PDMS flow cell. A solution containing lipid vesicles is injected through the microfluidic channel, and the lipid vesicles rupture to form a lipid bilayer on the silica surface. The formation of continuous membrane is

confirmed by using the FRAP technique as presented in Figure 5.4

5.2.2 Real-time kinetic binding assays

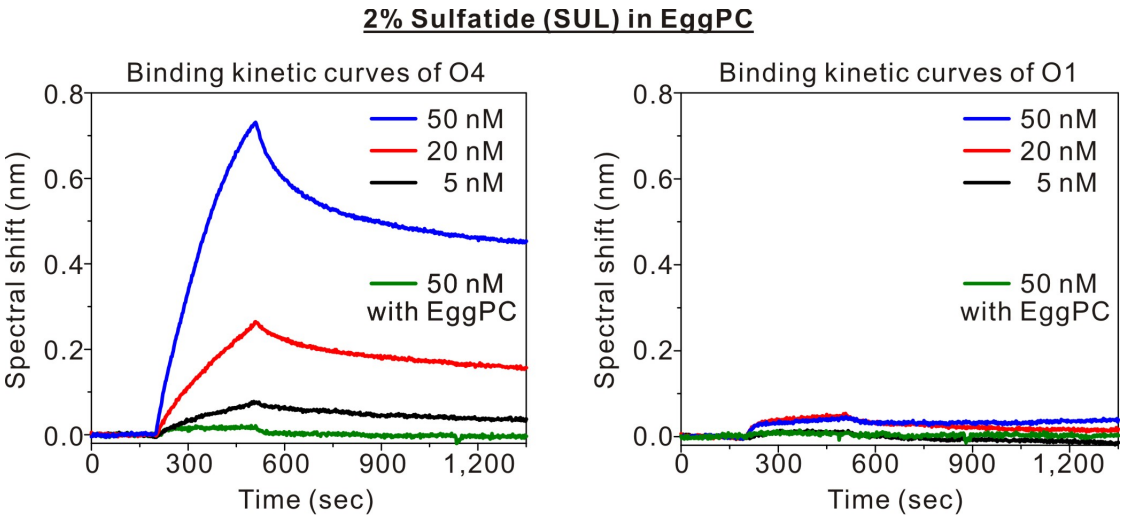

Figure 5.5: **Binding kinetic curves of IgM O4 and O1 antibodies with SLBs containing 2 % sulfatide (SUL).** IgM O4 and O1 binding to SLBs containing 2 % SUL in Egg PC. Green curves on both panels indicate negative controls only with egg PC membranes in the absence of sulfatide.

Forming SLBs on the silica-coated nanohole arrays allows SPR sensing of antibody binding to membrane-bound molecules. In this work, SLBs with and without SUL and GalC lipids are formed on the silica-coated nanopore sensor surface, and various concentrations of IgM O1 and O4 are injected through the PDMS microfluidic channels. Figure 5.5 shows binding kinetic curves of IgM O4 and O1 antibodies with SLBs containing 2 % SUL in the egg PC membrane. It is clearly seen that 5, 20, and 50 nM IgM O4 antibodies bind to SLBs containing SUL and induces spectral shifts. In a negative control, where the SLB is composed of only egg PC in the absence of sulfatide, there is no significant shift with 50 nM IgM O4, demonstrating the specific binding between IgM O4 and SUL. In contrast, IgM O1 does not cross-react with SLBs containing SUL,

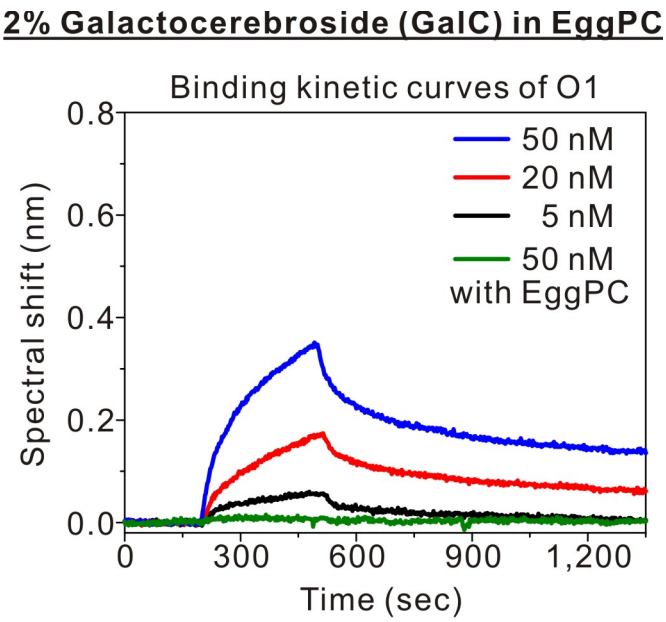

Figure 5.6: **Binding kinetic curve of IgM O1 antibody with SLBs containing 2 % galactocerebroside (GalC).** IgM O1 antibodies of various concentrations (5, 20, and 50 nM) bind to SLBs containing GalC and induce spectral shifts. In a negative control, IgM O1 does not bind to the SLB in the absence of GalC.

but it does bind to SLBs containing GalC as shown in Figure 5.6 Again the negative control performed in the absence of GalC presents the specific binding between IgM O1 and GalC. The calculated dissociation constants, K_D, for IgM O4-SUL and IgM O1-GalC are 1.5 ± 0.3 nM and 8.0 ± 2.0 nM, respectively. These are the first measurement of binding kinetics and affinity values between IgM O1/O4 antibodies and SUL/GalC containing lipid membranes.

5.2.3 Human therapeutic antibodies

While IgM O1 and O4 are mouse antibodies that promote remyelination in the mouse model of MS, a human autoantibody, IgM 22, also binds to oligodendrocytes and promotes myelin re-growth.[86] Recombinant IgM 22 antibodies have been prepared for

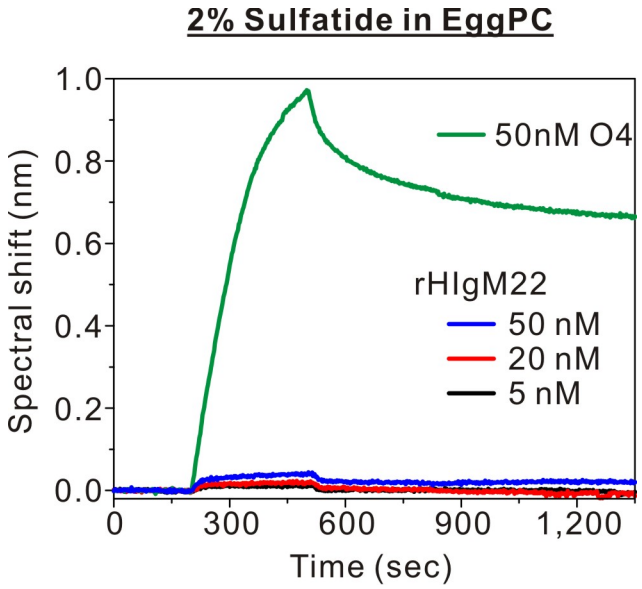

Figure 5.7: **Binding kinetic curves of IgM 22 with SLBs containing 2 % SUL.** IgM 22 was injected with various concentrations onto SLBs with 2 % SUL and there was no significant binding between IgM 22 and SUL-containing membrane to which mouse IgM O4 specifically binds.

human clinical trials for patients with MS.[88,89] For the clinical trials, information about binding affinity of the antibody and recognition of surface antigens is needed to determine the proper dose of drug molecules and potential side effects of the treatment. Previously it was determined that antibodies that bind to the oligodendrocyte surface promote the remyelination, but not all antibodies that bind to the surface can promote remyelination.[86] Indeed, binding of certain antibodies to their specific antigens may trigger the remyelination process, but the mechanism of remyelination process is not fully understood yet. Therefore, more effort is necessary to understand the mechanism of remyelination process caused by these therapeutic antibodies. Previously, experiments based on immunofluoresce techniques demonstrated that IgM 22 colocalizes with mouse IgM O4 on the surface of oligodendrocytes derived from sulfatide-positive cells,[88]

leading to a hypothesis that SUL may play a role in IgM 22 binding. To test the hypothesis, IgM 22 with various concentrations ranging from 5 to 50 nM was injected onto SLBs containing 2 % SUL. Figure 5.7 shows binding kinetics curves of IgM 22 with the SUL-containing SLBs. However, there is no significant binding between IgM 22 and the SUL-containing membrane to which mouse IgM O4 shows strong binding. This result indicates that the presence of only SUL alone is not sufficient to have IgM 22 bind to the surface. Thus, more screening tests with different types and combinations of cell-surface antigens are necessary. Nevertheless, these kinetic experiments with IgM antibodies and SLBs, however, demonstrate the capability of nanohole SPR sensors to identify antigens as well as to understand binding kinetic behaviors of antibodies and is useful for discovery of new therapeutic antibodies.

5.3 Plasmonic Biosensing with Suspended Lipid Bilayers

5.3.1 Limit of conventional SPR sensors

SLBs are a stable platform that can last for more than several hours to study their physical properties and molecular binding events between antibodies and small antigens conjugated to the membrane. As mentioned earlier, however, it is not suitable for studying transmembrane proteins due to the presence of underlying substrate that can affect to the functionality of the membrane-bound proteins as depicted in **Figure 5.3**. SLBs on polymer cushions or tethered lipid bilayers have proven useful for incorporating proteins into lipid bilayers for biosensing,[90] but the lipid bilayer is still only accessible from the top side, limiting their utility for studying transmembrane signaling processes. An alternative approach, suspended membranes over apertures in a substrate, also called as black lipid membranes (BLMs), has been employed for interrogating membranes and membrane-associated proteins. Studies on the electrical properties of lipid membranes and reconstituted ion channels have made extensive use of BLMs, even though the stability of BLMs is notoriously poor. To enhance the long-term stability of BLMs, some

groups have employed nanometer-sized apertures for electrical and physical property measurements of membranes and proteins.[91–94] This configuration allows for the incorporation of transmembrane proteins into the pore-spanning regions of the membrane and accordingly the ionic transport properties of the membrane proteins can be investigated.[67] While SPR technologies have been successfully used to characterize the interaction between pairs of soluble binding partners,[95–98] significant challenges still remain to adapt conventional SPR instruments to the needs of membrane proteins.[6] In particular, the metallic film/nanostructures and transparent substrate prohibits access to the bottom side of the membrane and can have issues of incorporating transmembrane proteins.[60,99] In contrast, nanoholes made in free-standing metallic films can be accessed from both sides of membranes, and the small dimensions of nanoholes can increase the stability of suspended lipid bilayers spanning over nanoholes. Therefore, combining pore-spanning lipid bilayers and nanopore-based SPR sensors would be a more suitable configuration to study membrane-bound proteins than other conventional SPR instruments.

5.3.2 Nanopore arrays in free-standing films

The concept of the nanopore-based SPR sensing with suspended lipid membrane spanning over nanopores is illustrated in Figure 5.8a. To form the pore-spanning lipid membrane with access from both sides of membrane, a nanopore array is patterned in a free-standing gold film instead of the Au-coated glass substrate. Similar to forming supported lipid bilayers, the hydrophobic Au surface was uniformly covered by a conformal silica layer, allowing vesicle rupture to form pore-spanning lipid bilayers. With the pore-spanning lipid bilayers, lipids spanning over nanopores are accessible from both sides, more closely mimicking natural cell membranes. The FDTD computer simulation shows strong field intensities due to SPs around the nanopores. (Figure 5.8b) The intense, highly confined plasmonic fields probe the local refractive index, suggesting high sensitivity in and around the edges of the nanopores[100–102] where the pore-spanning

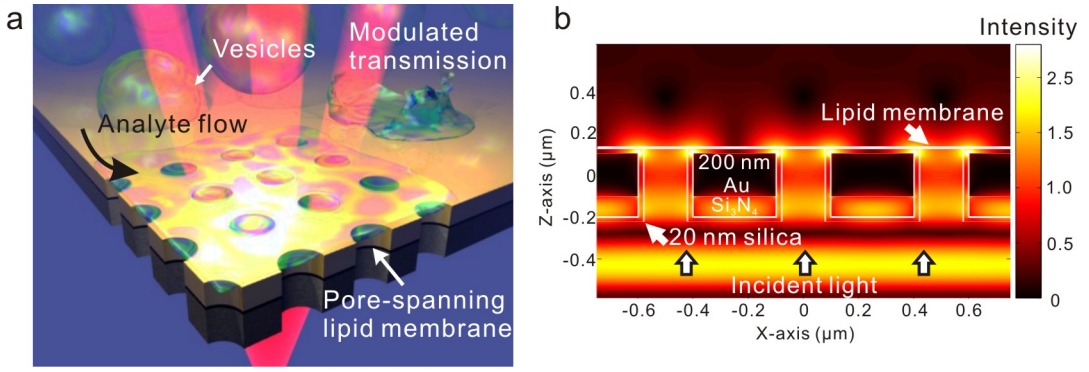

Figure 5.8: **Nanopore-based membrane biosensing.** (a) Concept of a nanopore array in free-standing Au/Si_3N_4 films for sensing in a suspended lipid membrane environment. The optical transmission is modulated by the presence of a lipid membrane, formed by vesicle rupture, and the subsequent molecular binding on the nanopore array. Part of the lipid membrane is suspended over the nanopores, better mimicking a natural cell membrane. (b) 3-D FDTD computer simulation of the electric field intensity on resonance (787 nm) shows the plasmonic field enhancement at the edges and corners of the nanopores, extending into the membrane region. Figure is adapted from Im *et al.*[53]

lipid membrane forms. Therefore, it is able to detect the formation of lipid bilayers as well as the molecular binding to the pore-spanning lipid membrane.

The free-standing Si_3N_4 film is made by an anisotropic Si etching process. Figure 5.9 shows a process flow for making free-standing nanopore device integrated with a PDMS microfluidic cell. First, the free-standing Si_3N_4 film is fabricated by patterning a 100 nm-thick low-stress Si_3N_4 layer on the backside of a Si wafer and a subsequent anisotropic Si etching process with potassium hydroxide (KOH). A thin Si_3N_4 film has a tensile stress in the film, which enables the formation of a stably suspended film over an almost mm^2 sized area, and therefore, is often used to make free-standing cantilevers or membrane structures. A Si wafer is anisotropically etched by the KOH solution due to the etch rate difference at the (100) and (111) crystalline planes. Because the etch rate of the (111) Si plane is negligible against the KOH solution, Si gets being etched until

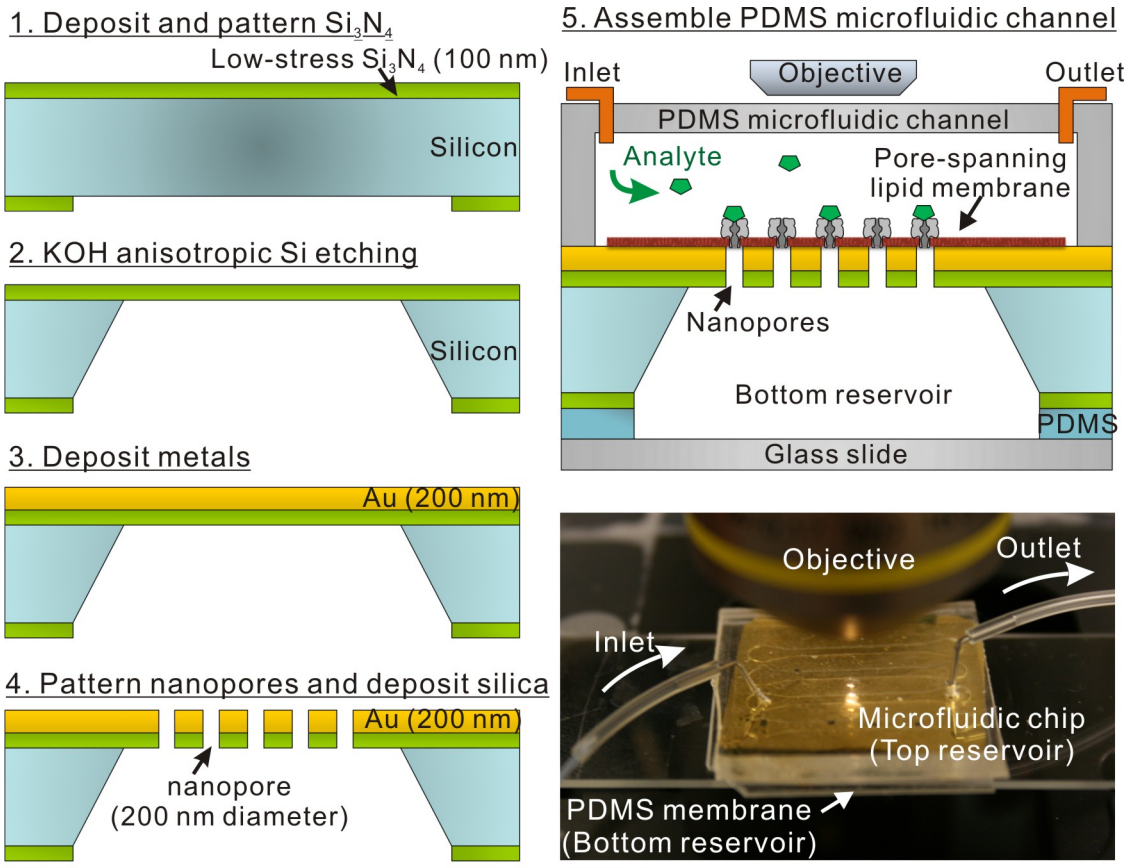

Figure 5.9: **Process flow for the fabrication of free-standing nanopore device.** Nanopore arrays are patterned in free standing Au/Si_3N_4 flims and integrated with PDMS microfluidic chips. Figure is adapted from Im *et al.*[53]

the (111) plane is exposed, making a trapezoid-shaped trench from a square pattern as depicted in Figure 5.9. After making the free-standing Si_3N_4 film, a 200 nm thick Au layer with a 5 nm-thick Cr adhesion layer is deposited by evaporation. Then, the periodic nanopore arrays are milled through the free-standing Au and Si_3N_4 stack with a FIB. Alternatively, the nanopore arrays can be patterned in the Si_3N_4 film first and then the Au film is deposited on the patterned Si_3N_4 film.[103] A PDMS microfluidic channel and a thin PDMS membrane sealed the top and bottom sides of nanopore chip to create buffer reservoirs, allowing both sides of the chip, the nanopores, and the lipid membrane to be immersed in aqueous solution. After forming a pore-spanning lipid bilayer, analytes were injected through the top-side microfluidic channel for real-time binding kinetic measurements. Figure 5.10 shows SEM images of the fabricated free-standing nanopore SPR device. The bottom reservoir created by anisotropic wet etching of Si with KOH is sealed by a thin PDMS membrane with a buffer solution filled inside. Figure 5.10b shows a cross-sectional SEM image of the nanopore array milled through the free-standing Au/Si_3N_4 films. The array consists of 16 $\times$ 16 nanopores with the pore diameter of 200 nm and periodicity of 500 nm. The Au sensing surface was then coated with a 20 nm-thick silica layer using ALD[104] as shown in Figure 5.10c. The silica layer uniformly covered the top surface and the sidewall inside each nanopore, which promoted vesicle rupture on its hydrophilic surface, allowing the formation of the suspended lipid bilayer over the nanopore array. In general, propagating SP-based periodic nanopore arrays show sensing ranges of about 100–300 nm in the visible wavelengths. Therefore, the presence of the 20 nm thick silica layer does not severely degrade the EOT detection sensitivity.[105] More discussion about the sensitivity degradation with dielectric overlayers is described in Chapter 6.

5.3.3 Nanopore SPR sensors with suspended lipid membranes

For pore-spanning membrane formation, a phosphate buffered saline (PBS) solution was injected through the microfluidic channel, flowing for at least 1 hour to ensure that

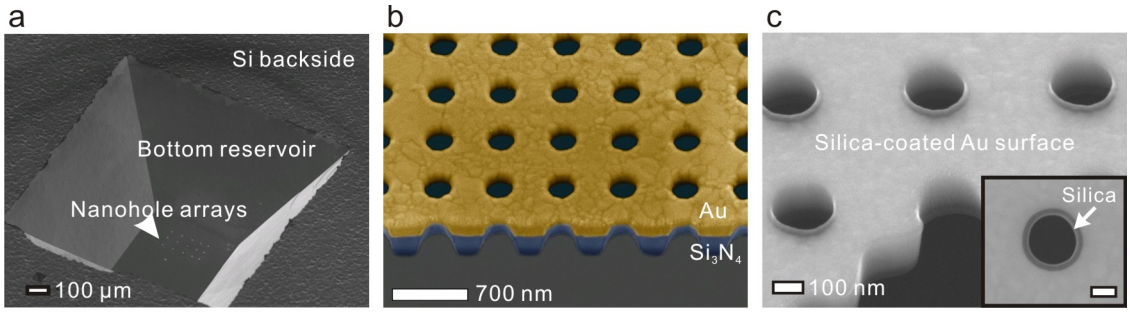

Figure 5.10: **SEM images of fabricated free-standing nanopore arrays.** (a) The backside of the free-standing film with a bottom reservoir. (b) Cross-sectional image of the nanopore arrays in a free-standing Au/Si_3N_4 film (colorized for clarity). (c) Cross-sectional image of the nanopore array after the ALD encapsulation process. Inset: The top surface and vertical sidewall of each nanopore is uniformly coated with a 20-nm-thick silica layer to promote vesicle rupture. Figure is adapted from Im *et al.*[53]

both sides of nanopores were filled with buffer. This guarantees that the membrane would be contacted by buffer on both sides, closely mimicking a natural cell membrane environment and increasing the stability of the pore-spanning lipid membrane. After washing the channel with NaTrisCa buffer, a solution containing vesicles is injected through the PDMS microfluidic channel at a slow flow rate of 10 μl/hr for at least 1 hour to allow vesicle rupture and formation of the pore-spanning lipid membrane. The channel was then rinsed with NaTrisCa buffer followed by PBS. The vesicles used in this study averaged 361 nm in diameter. Therefore, the rupture of a vesicle this size leads to a planar membrane disc that is 722 nm in diameter, which is more than sufficient to cover a 200 nm-sized individual nanopore. After lipid membrane formation, FRAP was used to confirm the formation of continuous membrane over the nanopores. From recovery curves, the diffusion coefficient of 1.99 $\pm$ 0.14 $\mu m^2/s$ was calculated, which is similar to the coefficient measured from membranes formed on a flat silica surface (1.94 $\pm$ 0.14 $\mu m^2/s$) The similarity between diffusion coefficient values suggests that a pore-spanning lipid membrane is formed over the nanopore array, and that the pores do

not limit lipid diffusion.[76] Without the formation of pore-spanning lipid membrane, the diffusion coefficient would be smaller than the value for a membrane on the flat silica due to the reduced pathway for diffusion of fluorescence dyes in the lipid membrane. In addition to FRAP, fluorescence was seen from the backside of nanopore arrays. Because the chip is opaque, fluorescence excitation and emission can only pass through the nanopores. Taken in combination with FRAP data, this provides strong evidence that the nanopores are covered with a continuous lipid membrane.

5.3.4 Real-time kinetic binding assays

After pore-spanning membrane formation, a transmembrane protein, α-hemolysin (α-HL), is incorporated into the membrane. α-HL is a water-soluble peptide monomer secreted from the pathogenic bacteria *Staphylococcus aureus* that binds to the plasma membranes of many mammalian cells.[106] Upon binding to the membrane the monomers freely diffuse about the membrane and self-assemble to form an about 1.4 nm sized heptameric transmembrane pore as shown in Figure 5.11. Because α-HL is stable over a wide pH and temperature range and the pore normally stays open, this transmembrane protein has been widely used to study transport of ions or small molecules as well as DNA. Because the heptameric pore of α-HL is irreversibly formed only in membranes with certain level of lateral diffusivity,[107] it is expected that the pores are presumably formed only at the pore-spanning membranes. After forming pore-spanning lipid membrane, anti-α-HL is injected to measure specific binding of the molecule to α-HL incorporated in the membrane. And the presence of anti-α-HL is confirmed by SPR sensing and fluorescence imaging after binding of streptavidin-R-PE (SAPE) to biotin conjugated on the anti-α-HL as depicted in Figure 5.12.

This sequence of formation and binding activities are deduced from spectral shifts of the resonance transmission wavelengths as shown in Figure 5.13. With the formation of pore-spanning lipid membrane, the resonance wavelength red-shifts. The spectrum

Figure 5.11: **Structure of α-hemolysin.** (a) Structures of α-hemolysin (α-HL) as a monomer (left) and as a heptameric pore (middle and right) Black lines indicate amino acids recognized by anti-α-HL. Figure is adapted from Ragle *et al.*[108] (b) Dimensions of the various parts of α-HL. Figure is adapted from Gu *et al.*[109]

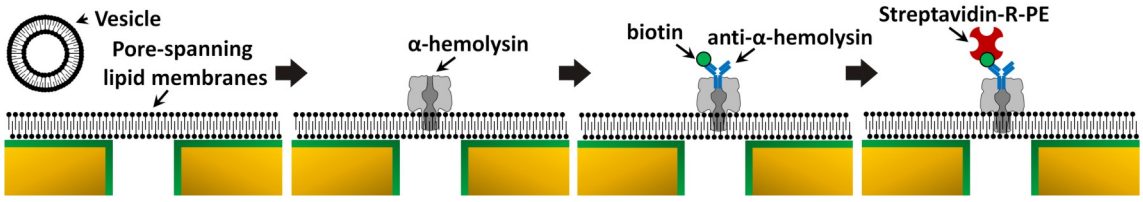

Figure 5.12: **Schematic of biosensing procedure with α-HL.** To study molecular binding between -HL and anti-α-HL, α-HL is first incorporated into pore-spanning membranes formed on the silica-coated nanopore sensor surface by vesicle rupture. Binding of anti-α-HL to α-HL is then detected. The binding of anti-α-HL and its binding location are confirmed with fluorescent streptavidin-R-PE which binds to biotin on the anti-α-HL.

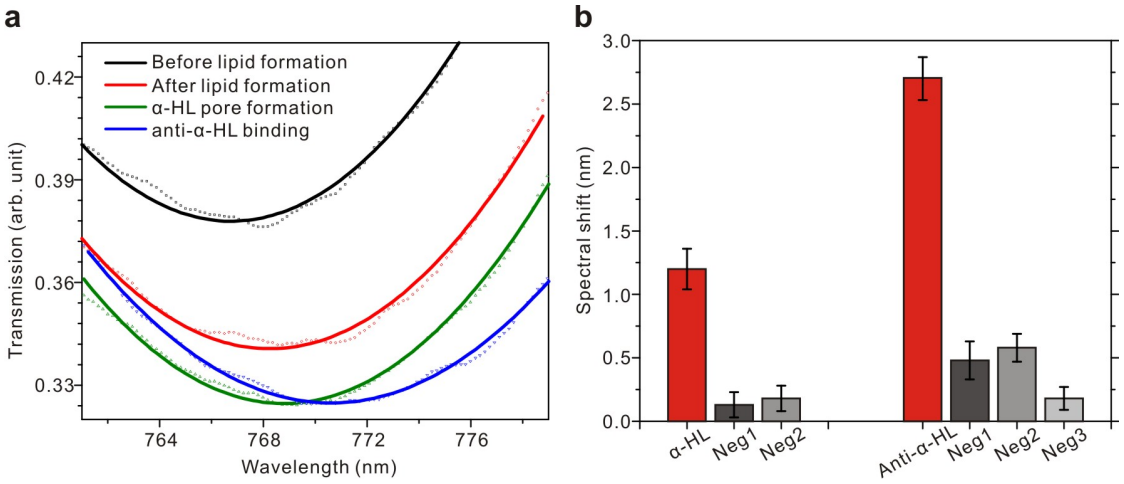

Figure 5.13: **Spectral sensing of α-HL incorporation and subsequent antibody binding.** (a) Transmission spectra change before (black line) and after the formation of pore spanning lipid membrane (red line), after the formation of α-HL pore in the membrane (green line), and after the binding of anti-α-HL (blue line). (b) Spectral shift from the binding of α-HL and anti-α-HL with three negative controls: negative 1 and 2 are lipid-free environments where pore-spanning membrane is replaced by a monolayer of APTES or BSA, respectively; negative 3 is the same pore-spanning lipid environment as the positive control, but with the absence of α-HL. Figure is adapted from Im *et al.*[53]

shifts further after incorporating transmembrane proteins, α-HL, into the lipid membrane and subsequent binding of anti-α-HL to the α-HL. The real-time kinetics of these procedures are measured from the spectral shifts of the transmission spectra as a function of time during molecular association and dissociation. To incorporate α-HL, 1 μM of α-HL solution was injected and incubated for an hour, sufficient to form transmembrane pores.[110] To confirm the incorporation of α-HL with the lipid membrane and specific binding between α-HL and anti-α-HL, the spectral shifts obtained from the positive control were compared with, in all, four negative controls where the pore-spanning lipid membrane is replaced (1) by APTES or (2) by BSA, and (3) α-HL is absent in the pore-spanning lipid membrane. As shown in **Figure 5.13**, spectral shifts from those

negative controls were less than 20 % of the shift in the positive control for both α-HL and anti-α-HL binding, indicating that α-HL can be incorporated only with the presence of pore-spanning lipid membrane and the specific binding of anti-α-HL can occur only with the presence of α-HL incorporated in the pore-spanning lipid membrane.

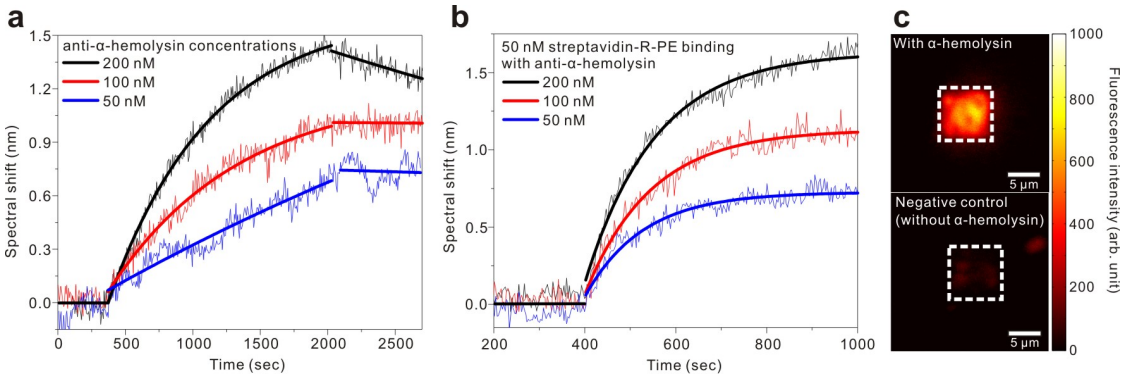

Figure 5.14: **Real-time kinetic measurements with anti-α-HL.** (a) Kinetic curves of anti-α-HL binding with different concentrations (50, 100, and 200 nM) to α-HL incorporated in pore-spanning lipid membranes. (b) Kinetics of 50 nM streptavidin-R-Phycoerythrin (R-PE) to biotinylated anti-α-HL. The three curves correspond to the three different concentrations of anti-α-HL antibodies in panel a. (c) Fluorescent images after binding of 50 nM streptavidin-R-PE onto 100 nM anti-α-HL. The negative control is performed without α-HL. Figure is adapted from Im *et al.*[53]

When α-HL is present in the pore-spanning lipid membrane, real-time binding kinetics of anti-α-HL to α-HL are measured with different concentrations (50, 100, and 200 nM) of anti-α-HL as shown in Figure 5.14a. After 5 min of baseline with a PBS solution, an anti-α-HL solution was injected to the channel with a constant flow rate of 30 μl/min. The binding association was measured for 15 min and then the channel was washed with PBS solution with the same flow rate of 30 μl/min for dissociation. A non-linear least squares analysis method[26] was used to determine the dissociation constant, K_D, from the kinetic measurements, giving a value of $1.9 \pm 1.0 \times 10^{-8}$ M. This value is close to the previously reported value ($K_D \sim 8.5$ nM) with monoclonal anti-α-HL binding.[?] For further confirmation of the specific binding of anti-α-HL with α-HL on

the pore-spanning lipid membrane, 50 nM of streptavidin-R-phycoerythrin (SAPE) was injected to bind with the biotinylated anti-α-HL. Figure 5.14b shows the binding kinetics of 50 nM of SAPE to the membrane-bound anti-α-HL antibodies. Each curve shows different maximum signal value, R_{max}, which corresponds to the maximum capacity of immobilized ligand that binds with analytes in the injected solution. The Rmax values have a linear relation to the concentration of anti-α-HL injected, indicating more anti-α-HL was captured on the surface at higher concentration of α-HL injected. After consequent binding of 100 nM of anti-α-HL and 50 nM of SAPE on the lipid membrane surface, the fluorescent images were taken as shown in Figure 5.14c. Positive and negative controls are with and without α-HL on the membrane surface, respectively. The positive control shows strong contrast of fluorescent intensity between inside and outside of array while the negative control shows partial dim spots around the array. The images are shown with the same intensity scale. This indicates that α-HL is primarily incorporated into the pore-spanning membranes formed over the nanopores and anti-α-HL and SAPE chiefly bind to the area where α-HL is incorporated. These α-HL and anti-α-HL kinetic measurements and subsequent binding with SAPE demonstrate successful formation of pore-spanning lipid membrane incorporated with transmembrane protein on a free-standing nanopore arrays and that these nanopore arrays are capable of detecting antibody binding events in real-time using the SPR sensing technique.

5.4 Conclusion

In this chapter, integration of nanopore-array SPR sensors with supported and suspended lipid bilayers for real-time kinetic biosensing is demonstrated. The supported lipid bilayers provide a stable platform to study antibody binding to lipid-based antigens. The suspended lipid bilayers over nanopores made in free-standing films are in contact with buffer solution and accessible on both sides of the bilayer, better mimicking

natural cellular membranes than supported lipid membranes. Both supported and suspended lipid membranes are formed using vesicle rupture facilitated by conformal coating of the gold sensing surface with a thin ALD-grown hydrophilic silica layer. FRAP measurements with fluorescence imaging demonstrate that the lipid membranes formed over the nanopore arrays are homogeneous and continuous. The detection of antibody binding to its surface antigens and transmembrane proteins incorporated in lipid membranes demonstrates the new functionality of nanohole SPR sensors. Nanopore array can combine SPR sensing capability with pore-spanning lipid bilayers to avoid undesirable side-effects for membranes, *i.e.* denaturing membrane proteins due to the presence of substrate in other conventional SPR techniques. This provides a natural platform for real-time label-free SPR sensing and high-throughput imaging[44] with lipid membranes. Furthermore, the solvent-free vesicle rupture method may be compatible with cell plasma membranes and membrane proteins integrated therein, demonstrating that this platform could potentially be employed for characterizing ligand binding to transmembrane proteins such as G protein-coupled receptors (GPCRs) and ion channels. In addition, SPR could be combined with electrical measurements, such as electrochemical impedance spectroscopy, to monitor and quantify insertion of ion channels and to study ion transport through the ion channels.

Chapter 6

Low-Cost High-Throughput SPR Instruments

Nanohole-based SPR biosensors have unique optical and geometrical advantages compared to conventional SPR instruments as described in Chapters 3 – 5. Despite these promising new directions and unique advantages, costly fabrication of the nanohole sensor chips has been a bottleneck for their widespread dissemination and use instead of commercialized instruments. In this chapter, high-throughput strategies for making low-cost plasmonic nanohole array sensors compatible with a wide range of biosensing applications with high-sensitivity to molecular detection are described. The results shown in this chapter are mainly derived from following publications:

1. H. Im, N. C. Lindquist, A. Lesuffleur, and S. H. Oh, *ACS Nano* **4**, 947-954 (2010).[105]

2. H. Im, S. H. Lee, N. J. Wittenberg, T. W. Johnson, N. C. Lindquist, P. Nagpal, D. J. Norris, S. H. Oh, *ACS Nano* **5**, 6244-6253 (2011).[73]

6.1 Plasmonic Nanohole Arrays with Dielectric Encapsulation Layers

6.1.1 Materials for plasmonic devices

Au has been most widely used for plasmonic devices because of its excellent chemical stability and good optical properties in the visible spectrum range. Many biosensors are made of Au because it is inert and compatible with biomolecules and the surface chemistry for Au is well established. However, Au is a costly material, so it is not suitable for certain applications such as disposable devices where the cost of the device is a key factor. Also the poor adhesion of Au to Si-based substrates including glass requires using an adhesion layer of Cr or Ti, which dampens plasmonic effect due to high absorption[111–114] and causes some non-specific binding of proteins to the adhesion layer.[115] Therefore, alternative materials have been tested and studied for plasmonic devices.[116–119] Among many materials, Ag-based plasmonic devices exhibit better intrinsic optical performance, *e.g.* longer SP propagation lengths, than devices made from Au, Cu, or Al within the visible spectrum. Unlike Au, Ag does not require the use of a Cr or Ti adhesion layer when conventional glass slides or Si wafers are used as a substrate, although adhesion can still be a problem. In addition to these advantages, its relatively low-cost has lead to Ag being widely used as electrodes for plasmonic solar cells rather than Au.[120,121] Nevertheless, many plasmonic devices, including the majority of biosensors, are still made with Au. One of the reasons lies in the poor chemical stability of Ag: it oxidizes readily in air, resulting in unstable chemical properties. In addition, silver is not fully compatible with biological samples and is toxic to cells.[122] Therefore, a broad range of applications can benefit by developing a simple method that can harness the better intrinsic plasmonic performance of Ag while circumventing its poor chemical stability.

6.1.2 Encapsulation of nanohole arrays with ALD overlayers

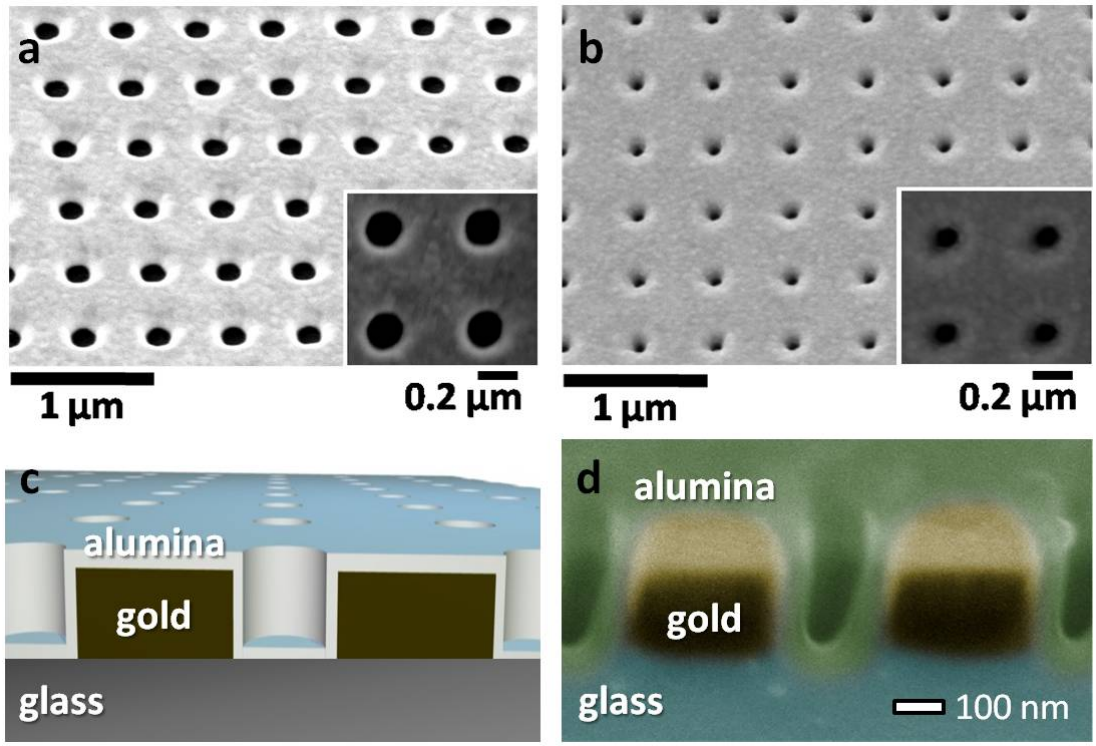

Figure 6.1: **Periodic nanohole arrays encapsulated with alumina overlayers.** A SEM image of nanohole arrays in gold film on a glass substrate (a) before and (b) after ALD of a 40 nm thick alumina overlayer. The insets to panels a and b show enlarged images of the nanoholes; (c) a cross-sectional schematic of a nanohole array with an alumina overlayer deposited with ALD; (d) a cross-sectional SEM image of a nanohole array with a 40 nm ALD-grown alumina overlayer. Figure is adapted from Im *et al.*[105]

One possible solution for protecting Ag from unwanted oxidation is encapsulating the Ag nanostructure with a protective layer. Atomic layer deposition (ALD) of a conformal dielectric layer on the nanostructures can provide a generally applicable solution. The ALD technique utilizes self-limiting chemical reactions to enable conformal deposition of compound thin films with atomic layer thickness resolution.[123,124] Among materials that can be deposited by ALD, alumina (Al_2O_3) can act as an excellent barrier against

gas diffusion and is thus suitable for device encapsulation.[125] Because of precise thickness control and conformal deposition, ALD alumina has been used to characterize the localized surface plasmon resonance (LSPR) of silver nanoparticles as well as to increase the stability of patterned silver films for surface-enhanced Raman spectroscopy.[126,127] In this work, ALD alumina is used to encapsulate periodic nanohole arrays. The effect of the alumina layer on the nanohole arrays is studied and the capability of alumina for protecting Ag nanohole arrays from unwanted oxidation is tested. First, to compare properties of Au and Ag nanohole arrays as well as their sensitivity, a nanohole array with 180 nm hole size and 500 nm periodicity was made in a 200 nm-thick Au or Ag film on a glass substrate using FIB and covered by alumina overlayers using ALD as presented in Figure 6.1. The ALD provides a conformal layer, covering the flat metal areas as well as the sidewalls and bottoms of the nanoholes.

Similar to biosensing of a thin molecular layer, the deposition of thin alumina layers changes the local refractive index change on the nanohole array surface and red-shifts the transmission spectrum. Figure 6.2 shows the transmission spectra change of both gold and silver nanohole arrays with 180 nm hole diameter and 500 nm periodicity versus the thickness of Al_2O_3 overlayer. As described in Chapter 2, the optical transmission through the periodic nanohole array in metallic films shows dominant peaks that correspond to the (1,0) and (1,1) resonances at the metal-dielectric interfaces from the Equation (2.21). For Au nanohole arrays, only two dominant resonance peaks from the Au-air interface are shown in the transmission spectra because the resonance peaks from the Au-glass interface are dampened due to the absorption of a Cr adhesion layer. For Ag nanohole arrays, however, more peaks from (1,0) and (1,1) resonances on both Ag-glass and Ag-air interfaces are observed in the absence of Cr adhesion. It should be noted that the transmission through the Ag nanohole array is greater than the Au nanoholes with the identical nanohole parameters and measurement condition. This is due to the better optical properties of Ag as well as the absence of Cr adhesion layer.

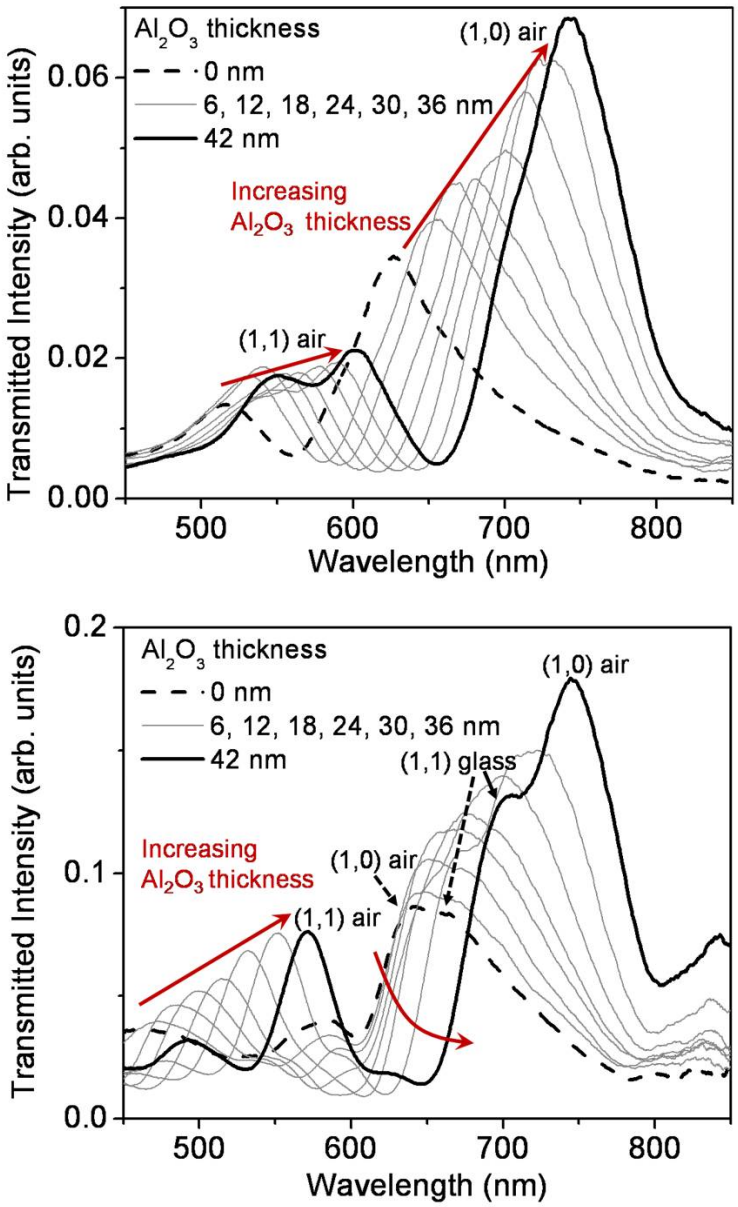

Figure 6.2: **Transmission spectra of nanohole arrays with ALD alumina.** Sequence of transmission spectra through the same 16 ×16 nanohole array as the thickness of the ALD-grown Al_2O_3 overlayer increases from 0 nm to 42 nm at 6 nm intervals. The diameter and periodicity of nanohole is 180 and 500 nm, respectively. The nanoholes were milled through (a) gold and (b) silver films. Figure is adapted from Im *et al.*[105]

For both samples, however, the metal-air transmission peaks red-shift and their intensity increases as the thickness of the Al_2O_3 overlayer increases from 0 nm to 42 nm. The spectral shifts are due mainly to the refractive index response of suface plasmon polaritons (SPPs) as presented in Chapter 3. According to the Equation (3.3), neff increases as the thickness of the Al_2O_3 overlayer increases, red-shifting λ_{peak} since n_{layer}, the refractive index of Al_2O_3, is larger than n_{bulk}, the refractive index of air. Therefore, ALD of a dielectric layer, with its ultrafine thickness resolution, can precisely tune the plasmon resonance of metallic nanostructures. Additionally, as the peaks red-shift, the transmitted light intensity also increases, shown in Figure 6.2. This is due to combinations of different effects. First, as resonance red-shifts to longer wavelength, SP damping losses decreases.[128] Second, as the effective hole size is increased due to filling the hole with a higher index Al_2O_3, the waveguide-type attenuation in the subwavelength holes decreases, boosting the transmission. Third, index-matching effects between both sides of the nanohole array, *i.e.* making an asymmetric system (air-metal-glass) into an effectively symmetric one (air-alumina-metal-glass) at a certain Al_2O_3 thickness, have also been shown to increase the transmission efficiency.[129]

Because response to a thin dielectric layer is similar to sensing a molecular layer, ALD of thin dielectric overlayers can be used to characterize the local sensitivity and the probing range of SPR devices. Figure 6.3 shows the spectral shifts of the (1,1) air resonance peaks of Ag and Au nanohole arrays as a function of increasing Al_2O_3 overlayer thickness. The (1,0) air resonance peak was not tracked because of the wavelength range limits of our spectrometer. Beyond $\sim$ 100 nm thickness, comparable to the decay length of the SP evanescent field, the spectral shifts are saturated. In the linear region, where the Al_2O_3 overlayer thickness is less than 50 nm, the spectral shifts for both Ag and Au nanohole arrays are linearly proportional to the Al_2O_3 thickness, indicating the linear probing range. In this regime, the Ag nanohole array show about 30 % better sensitivity to the local refractive index change induced by the Al_2O_3 overlayers than the Au nanohole array. This experiment also shows that an overlayer thickness of up

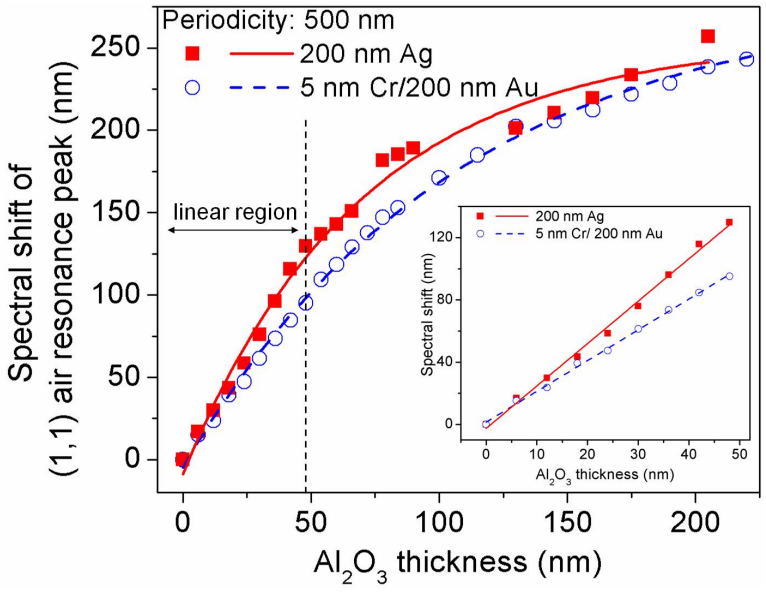

Figure 6.3: **Long- and short-range responses of nanohole arrays with Al_2O_3 overlayers.** As the thickness of the Al_2O_3 overlayer increases from 0 to 205 nm, the (1,1) air peaks of the Ag and Au nanohole arrays red-shift. Experimental results are shown as squares (Ag) and circles (Au), and the data are fit with exponentially saturating curves. The shift is approximately linear with Al_2O_3 thicknesses ranging from 0 to 48 nm. Figure is adapted from Im *et al.*[105]

to 50 nm does not degrade the sensitivity for detecting the subsequent deposition of an additional Al_2O_3 layer. Increasing the overlayer thickness further, however, gradually reduces the probing range, and the detection sensitivity is sharply degraded. These results demonstrate that the ALD overlayer can be used to tune the optical transmission of plasmonic nanoholes in a precisely controlled manner, which will be valuable for biochemical sensing, photonics, as well as for understanding the various mechanisms involved in the EOT effect. In particular, the increased optical transmission can improve SPR imaging systems, which is often dominated by shot noise.[50]

6.1.3 Chemical stability with ALD overlayers

Besides enhancing plasmon resonances and providing tunability, the conformal deposition of Al_2O_3 overlayers simultaneously act as an encapsulation layer to protect Ag nanohole arrays against unwanted oxidation or contamination. It has been reported that even a few nanometers of Al_2O_3 layer deposited by ALD is sufficient for blocking water vapor penetration through the layer.[125] Therefore, encapsulating Ag-based plasmonic structure with a thin Al_2O_3 layer can improve its poor chemical stability. For robust protection against unwanted oxidation, a thicker oxide is more desirable. On the other hand, to maintain sensitivity to molecules binding on the surface, a thinner overlayer is needed. As seen in Figure 6.3, the spectral response remains linear with a total ALD thickness below 50 nm. Therefore, a 20 nm alumina overlayer, which does not sacrifice the detection sensitivity and is sufficient as a gas diffuse barrier, was chosen to fulfill both requirements, and its resistance against oxidation was tested.

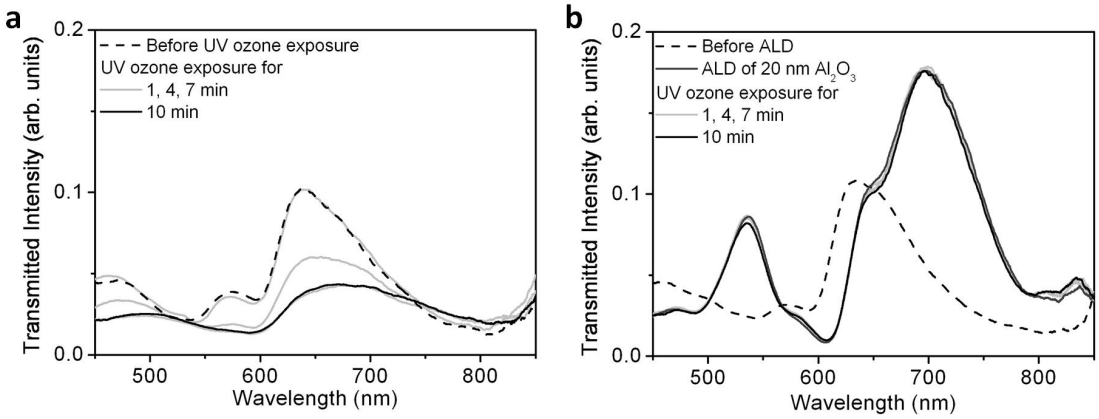

Figure 6.4: **Comparison of transmission spectra from nanohole arrays with an Al_2O_3 protection layer against chemical oxidation.** (a) Transmission spectra change as a nanohole array made in a silver film is exposed to UV ozone for 1, 4, 7, and 10 min without a protective Al_2O_3 overlayer and (b) with a 20 nm protective Al_2O_3 overlayer. Figure is adapted from Im *et al.*[105]

Figure 6.4 shows transmission spectra of Ag nanohole arrays with and without 20 nm-thick Al_2O_3 protection layer. The transmission through the Ag nanohole array is enhanced by the deposition of a 20 nm-thick Al_2O_3 overlayer. The Al_2O_3 layer was deposited at 50 °C to prevent the possible silver-oxide formation during the ALD process due to exposure of Ag surface to water vapor.[126] Following the initial measurements of the EOT spectra, the samples were simultaneously exposed into a harsh oxidizing environment inside an UV-ozone chamber, which generates an intense oxygen plasma, and their individual optical transmission spectra were recorded after 1, 4, 7 and 10 minutes of treatment. The EOT spectrum of the Au nanohole array did not show any measurable change after 10 minutes of oxidation while the Ag nanohole array shows a dramatic reduction in the optical transmission intensity as well as broadened peak widths, which was caused by rapid oxidation of Ag film Figure 6.4a. The Ag nanohole array, however, which was encapsulated with 20 nm-thick Al_2O_3, did not show any noticeable change in the transmission spectra Figure 6.4b. This result confirms that the Al_2O_3 overlayer acts as a good passivation layer for protecting the Ag from oxidation. The exact thickness of the alumina overlayer is determined depending on the specific applications, weighing the relative importance of oxidation protection versus maintaining sensitivity to surface events. ALD encapsulation of alumina (Al_2O_3) or other oxide materials such as silica (SiO_2) or hafnia (HfO_2) overlayers can also be used for other metals such as Cu or Al, tuning their optical properties as well as to protecting the surface from oxidation. The surface of plasmonic devices encapsulated by the dielectric layers can be subsequently functionalized by using a self-assembled monolayer or lipid membranes for biosensing.[53,130] In addition, the ALD overlayers can be used to precisely control the coupling between quantum emitters and the SP waves as well as reducing quenching effects.[131] This technique can be applied to a broad range of plasmonic nanostructures for improved optical properties and stable functional surfaces.

6.2 Large-Area Fabrication of Plasmonic Nanohole Arrays

The majority of existing work on nanohole arrays utilized direct patterning of metal films using focused ion beam (FIB) milling or electron-beam lithography (EBL).[28,39,44,132] These serial writing techniques, however, are not suitable for a routine production of nanohole array chips due to their expensive fabrication costs. Therefore, developing a new fabrication method for producing nanohole arrays with high-throughput is highly desired.

6.2.1 Noise reduction with large-area nanohole arrays

In developing a new fabrication method, it is important to consider the size of the nanohole arrays. For initial theoretical studies and proof-of-concept experiments, FIB or EBL has been mostly used because of its convenience to tune hole size and periodicity. In this case, arrays with small footprints were mainly used because more number of holes does not make the transmission peak sharper if the number of holes is larger than 9×9.[133]

This is due to the limited propagation length of SPs in nanohole arrays. However, for practical applications, especially for biosensing which monitors spectral shift in real-time, it is important to consider the signal-to-noise (S/N) ratio of the sensor, corresponding to the limit of detection (LOD) of the system. The LOD is an important parameter to compare different sensing systems and is often defined as the concentration of target sample that induces a signal 3 times larger than the noise level. To improve the LOD of a sensor, it needs to either enhance the sensitivity, which is defined as the slope of the response-concentration curve as plotted in Figure 6.5. A sensor with higher sensitivity can produce larger signal change from the same amount of concentration change. Within the same sensing configuration, it is often difficult to dramatically improve the sensitivity without changing the sensing scheme. Indeed, reducing the background noise level is sometimes a practical approach in order to achieve lower LOD. It should be noted

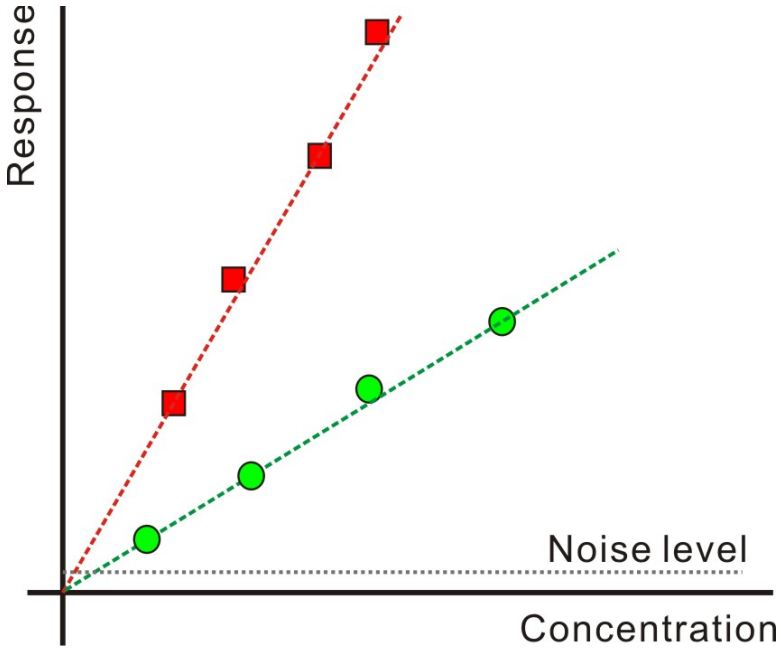

Figure 6.5: **Definition of sensitivity and limit of detection (LOD).** The sensitivity of sensors is defined as a slope in a plot of response vs. concentration. And the limit of detection is defined as a concentration that induces a signal equal to 3 times of the noise level, *i.e.* a signal-to-noise (S/N) ratio is equal to 3. Thus, depending on the background noise level, a sensor with lower sensitivity may be able to detect lower concentration of analyte if the S/N ratio is better because of lower noise level.

that the S/N ratio is more related to the LOD ratio rather than only the sensitivity itself. Depending on the background noise level, a sensor with lower sensitivity may be able to detect lower concentration of analyte than another sensor with higher sensitivity if the S/N ratio is better because of lower noise level.

One simple strategy to reduce the noise is increasing the transmitted light intensity and averaging the transmission spectra more frequently. Figure 6.6 shows the effect of signal averaging to the background noise level. With the same measurement setup, the noise level (in spectral peak position) is reduced about 10 fold by averaging the spectra for 200 times. In the experiment, the integration time was only 10 ms, thus

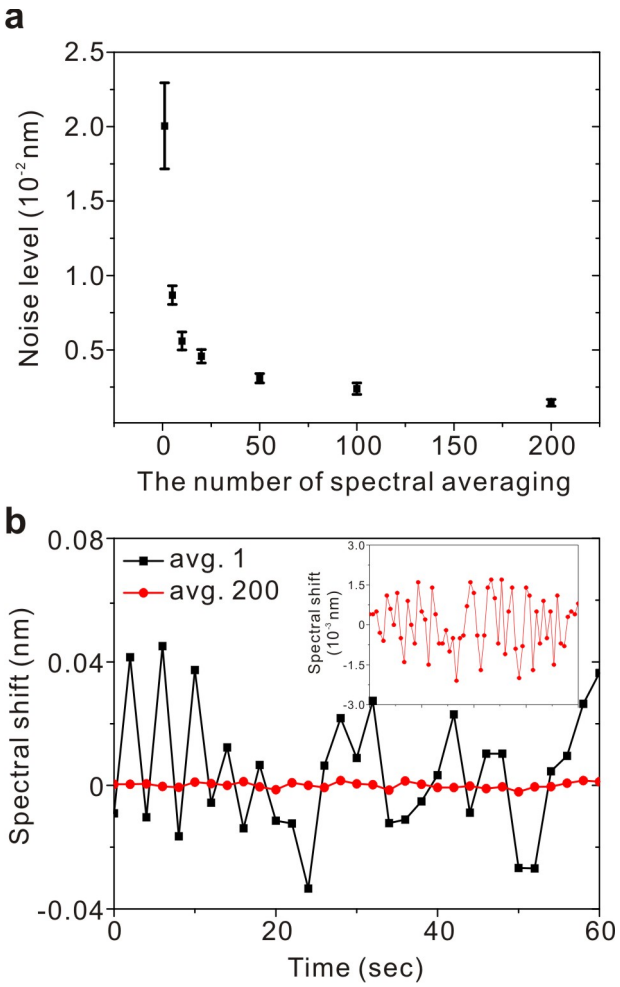

Figure 6.6: **Noise reduction using spectral averaging.** (a) The background noise level with the number of spectral averaging. The noise is reduced about 10 folds by averaging transmission spectra for 200 times. (b) Comparison of real-time spectral shift with and without signal averaging process. The inset to panel b shows a zoomed-in plot for 200 times averaging.

200 times averaging provides a time-resolution of 2 sec. If faster time resolution is desired, shorter number of averaging still provides improved noise level by several folds. With the 200 times spectral averaging, the standard deviation in a minute of baseline is calculated as about 1.5 $\times 10^{-3}$ nm. With previously reported bulk refractive index sensitivity of nanohole arrays with the similar dimension,130 400 nm/RIU, this noise level corresponds to 3.75×10^{-6} RIU. This resolution is slightly higher than commercial BIAcore instrument, 1×10^{-6} RIU. But it should be noted that it is the noise level only by averaging the signal with a short integration time without additional noise reduction components. Other additional methods such as adding temperature controllers for both chip[134] and light source,[135] and using data processing[136,137] can further reduce the noise level, becoming comparable with the resolution of commercial instruments. To increase the transmitted light intensity, the nanoholes should be patterned over a larger area. In addition to the noise reduction, the large-area pattern allows integrating with multiple microfluidic channels, providing multiplex capability. For the large-area patterns, serial writing techniques such as FIB or EBL is too slow and expensive. Therefore, high-throughput fabrication techniques such as nanoimprint lithography[138] or interference lithography[139] are more suitable.

6.2.2 Nanohole arrays with nanoimprint lithography

Nanoimprint lithography (NIL) was designed to make nanometer-sized structures over a large-area with high-throughput. Conventional optical lithography requires using expensive optical components and precise optimization in order to obtain sub-wavelength sized features. In contrast to optical lithography, NIL is based on mechanical stamping where a master template mold is pressed onto a resist layer on a substrate. Then, the patterns in the master mold are transferred into the resist layer, and the underlying substrate is etched with the resist layer as a mask as depicted in Figure 6.7. Then, the master mold is re-used to duplicate other nanohole samples.

Figure 6.8 shows an SEM image of nanohole array fabricated in 200 nm-thick Au

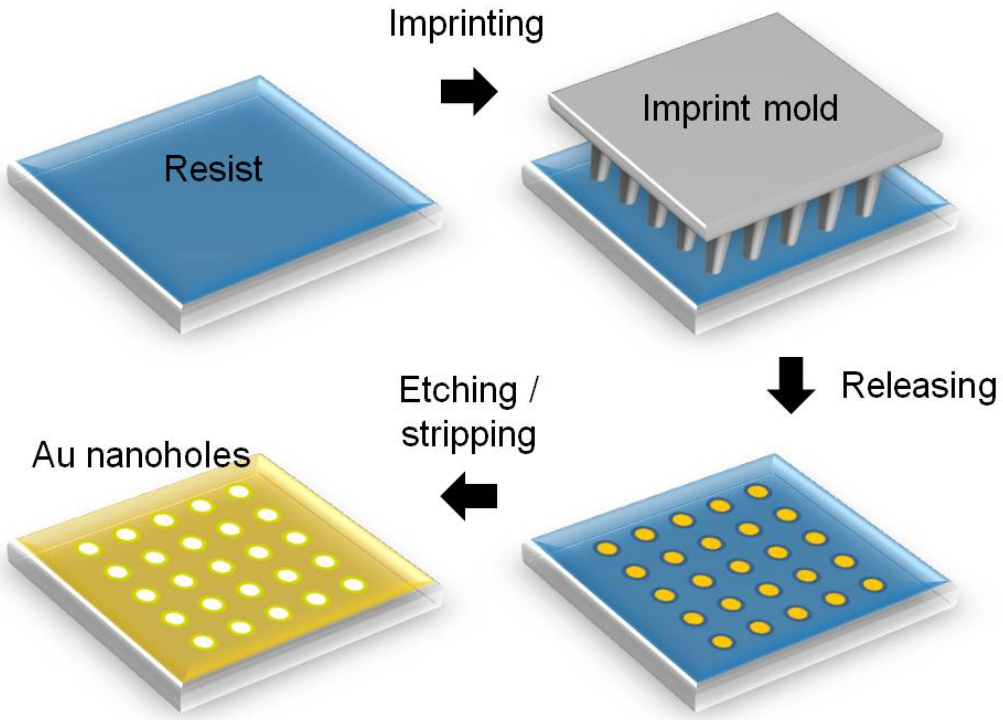

Figure 6.7: **Schematic of nanoimprint lithography process for the fabrication of periodic nanohole arrays.** Following to spin-coating resist on a Au-coated glass substrate, a master mold with circular post patterns is imprinted onto the resist layer. Then, circular patterns are transferred and the underlying Au is etched with the patterned resist layer as a mask.

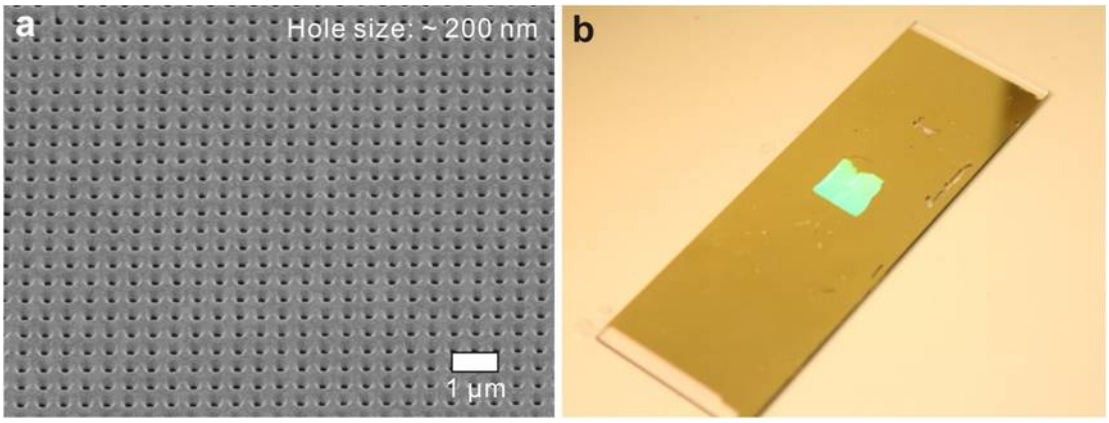

Figure 6.8: **A nanohole array chip prepared using nanoimprint lithography.** (a) An SEM image of Au nanohole array with 200 nm hole size and 500 nm periodicity. The nanopore array was made using nanoimprint lithography with a subsequent ion milling process. (b) A photograph of the fabricated nanopore chip. The nanohole array is made in an almost cm^2 area in the center of a Au-coated glass slide. This chip is assembled with a 12 channel-PDMS microfluidic flow cell and used for kinetic experiments with lipid membranes presented in Chapter 5.2.

film on glass slide using nanoimprint lithography and a photograph of the fabricated chip. The nanohole array is made over an almost cm^2 area in the center of a Au-coated glass slide. This chip is assembled with a 12 channel-PDMS microfluidic flow cell and used for kinetic experiments with lipid membranes presented in Chapter 5.2.

6.2.3 Nanohole arrays with template stripping

Beside nanoimprint lithography,[140–142] other novel fabrication methods including interference lithography[143–145] and nanosphere lithography[146–148] have been employed to pattern nanoholes over large areas. With conventional interference or nanoimprint lithography, photoresist is spun on the metal film, followed by exposure, development, and patterning by ion milling or lift-off, which requires the use of high-capital-cost equipment and cleanroom processing for every chip produced. While nanosphere lithography can eliminate the needs to use a photomask and an exposure system, precise tunability

and long-range patterning order is difficult to achieve, and in most cases only optically thin (< 50 nm) metal films have been demonstrated. A new fabrication technique, template-stripping,[149] leverages mature silicon processing technology to make a precisely patterned Si master template. The pattern is then transferred to a deposited metal film, which can be peeled off on demand using an adhesive backing layer. Because a single master template can be repeatedly used to make multiple (> 50) copies of the patterned metal films, this process does not require any additional photoresist processing, exposure, etching or lift-off. Furthermore, the metallic surface obtained by template stripping retains the smoothness of the crystalline Si master template, typically less than 1 – 2 nm, in contrast to the rough surfaces of as-deposited metal films.[149] The fabrication of smooth patterned surfaces is essential for applications in plasmonics. Since the electromagnetic fields of SP waves are confined to within 10-100 nm of the metallic surfaces, even nanometric roughness can severely dampen the propagation of SP waves or generate unwanted random "hot spots".[149,150]

For the fabrication of periodic nanohole array, the nanoimprint lithography is now used to pattern the reusable Si master templates, from which metallic nanohole arrays are replicated with metal deposition and a one-step, peel-off process using optical epoxy as a backing layer. The template-stripping procedure is illustrated in Figure 6.9. A silicon master template containing a periodic array of deep circular trenches was fabricated using nanoimprint lithography. A 100-nm-thick SiO_2 layer was grown on 4-inch Si wafers by wet oxidation. The Si wafers were then spin-coated by a thermal nanoimprint resist, which was imprinted with a silicon nanoimprint stamp. The nanoimprint stamp contains a periodic array of silicon posts with 210 nm in diameter, 350 nm in height and 500 nm in periodicity over an 8 mm $\times$ 8 mm area. After thermal imprinting, the SiO_2 layer was patterned by reactive ion etching (RIE) with the thermal resist as an etch mask. After removing the resist, circular trenches were made into the Si wafer using the SiO_2 layer as a hard mask. After removing the SiO_2 layer and cleaning the surface, a 200-nm-thick Au film was deposited onto the Si template using evaporation. Similar

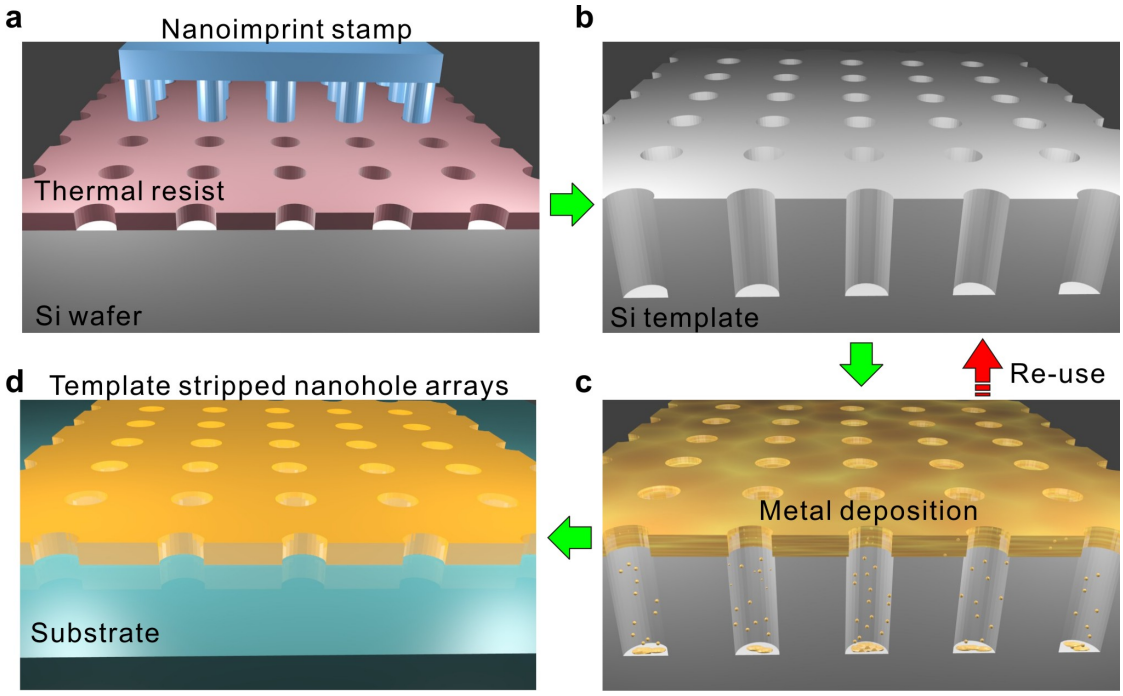

Figure 6.9: **Schematic for template stripping of large-area nanohole arrays.** (a) A thermal resist layer spun on a Si wafer is imprinted with a nanoimprint stamp with circular post patterns; (b) The Si wafer is subsequently etched to be a nanohole template with deep circular trenches; (c) A metal film is directionally deposited on the Si template; (d) The metal surface is coated with a thin layer of epoxy and covered with a glass slide. The Ag film is then peeled off of the template to reveal the smooth nanohole array made in the metal film. The Si template can be reused to make multiple identical samples. Figure is adapted from Im *et al.*[73]

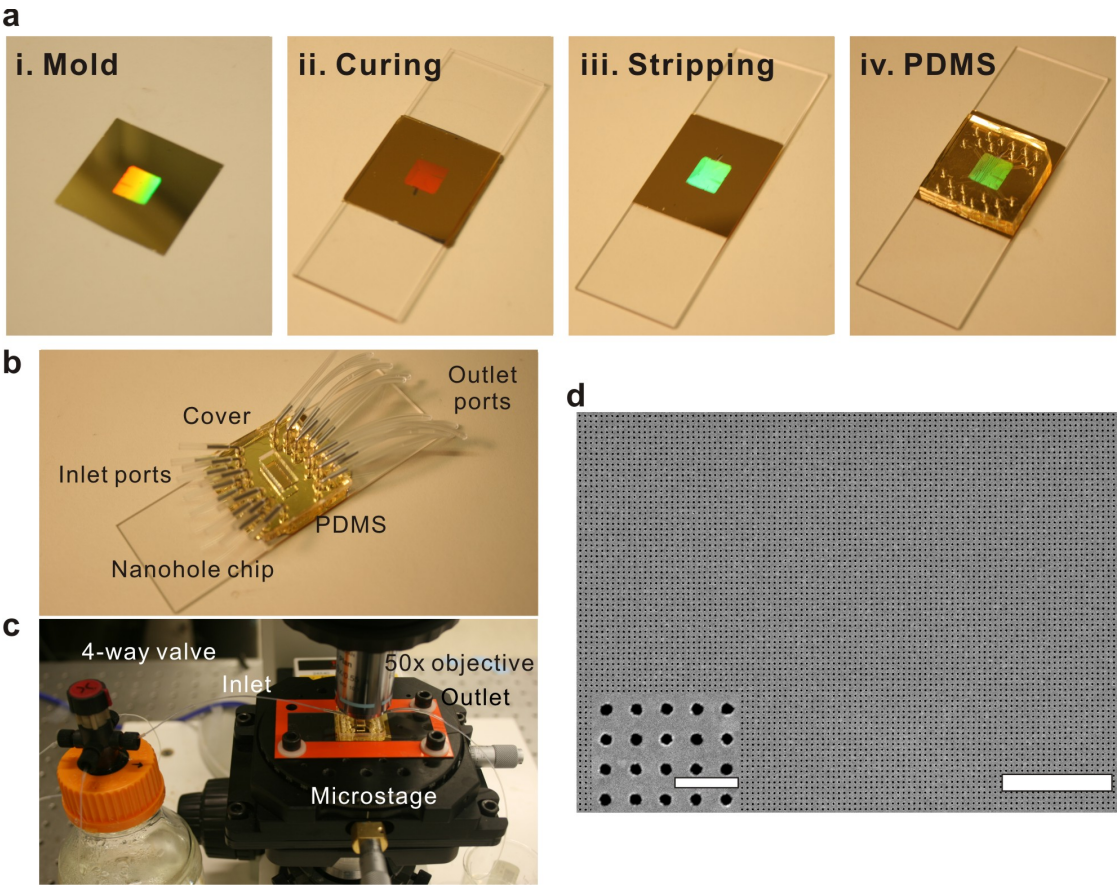

Figure 6.10: **Au nanohole array chips using template stripping for biosensing.** (a) The Au nanohole array is made through processes of depositing Au on the mold, curing the film with optical epoxy covered by a glass slide, and stripping the film off of the mold. Then the template-stripped nanohole chip is aligned with a 12 channel-PDMS microfluidic flow cell. (b) A photograph of ready-to-use nanohole array SPR sensor chip. The plastic cover is placed on the PDMS to prevent lifting the PDMS and leaking a solution. Inlet and outlet ports are connected with tubes through metal connectors. (c) A photograph showing the measurement setup. The nanohole chip with PDMS is placed on a microstage on the upright microscope and the inlet tube is connected to a 4-way valve which control a solution injected to the PDMS channel on the nanohole chip. (d) An SEM image of the template-stripped Au nanohole array. The scale bar is 5 μm. The inset shows a zoomed-in image of nanoholes. The scale bar is 1 μm.

to the lift-off process used in standard lithography, here we exploit the poor step coverage of the evaporation process to detach metal atoms deposited in each trench from the metal film on the top surface of the patterned silicon master, as depicted in Figure 6.9c. Thus a simple metal deposition process can create the nanohole patterns in the deposited metal film without using lithography, etching, or ion milling. In this process, it is crucial to reduce the metal deposition on the sidewalls, which requires the formation of vertical sidewalls in the master template and an alignment of the metal evaporation source normal to the sample surface. The patterned Au film was subsequently coated by a UV-curable optical epoxy and then covered by a glass slide. After curing the epoxy under UV light, the metallic film perforated with nanoholes, now adhered to the glass slide, was peeled off of the template to reveal the smooth surface as shown in Figure 6.10 The Si master mold can be cleaned and reused to make duplicate samples multiple times.

For biosensing, the template-stripped nanohole array is first incubated with a 1:1 mixture of 11-mercaptoundecanoic acid and 2-mercaptetahnol to form a SAM with carboxyl functional groups for surface chemistry based on amine coupling. Then, the nanohole chip is assembled with a 12-channel PDMS microfluidic flow cell as shown in Figure 6.11. The carboxyl group in the SAM layer is activated by flowing a mixture of N-Hydroxysuccinimide (NHS) and 1-ethyl-3-(3-dimethylaminopropyl) carbodiimide) (EDC) and protective antigen (PA) is immobilized through the amine coupling. And the unbound surface is quenched using an ethanolamine solution. After immobilizing the PA on the sensing surface, genetically engineered single-chain antibody fragments (scFv) that bind to the PA with different binding affinities were injected through the channel.[151] These scFv molecules are only 23 kDa, about 45 times smaller than IgM antibodies in Chapter 5.2. Because the refractive index change due to binding of small molecules in SPR sensing is so little, sometimes it requires labeling with bigger molecules to be detected.

Figure 6.12 shows the measured binding kinetic curves between 4 different scFv

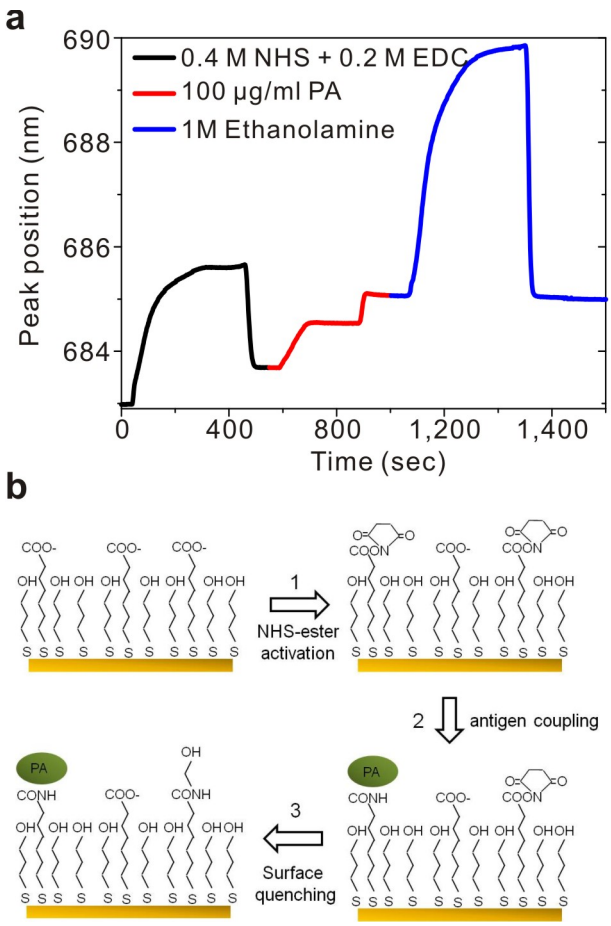

Figure 6.11: **Procedure of antigen immobilization using amine coupling.** (a) Kinetic responses of spectral peak position during the immobilization of protective antigen (PA). (b) Schematic showing the surface chemistry of amine coupling for immobilizing the PA.

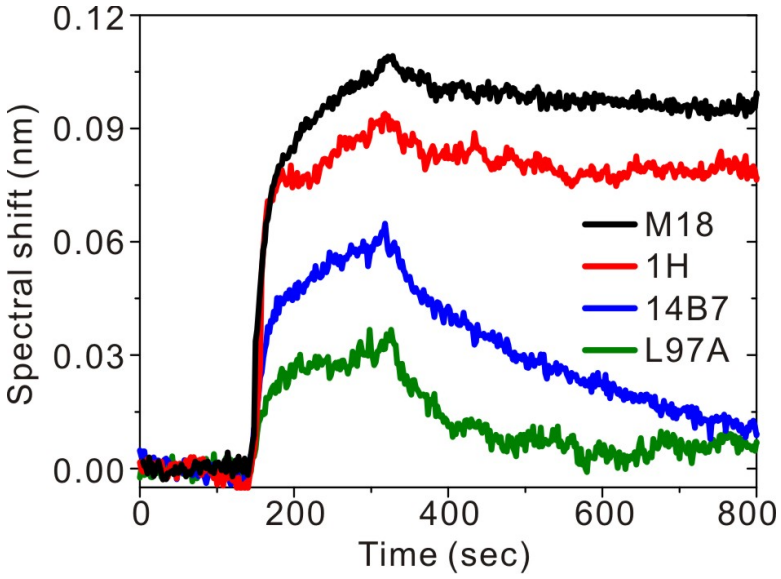

Figure 6.12: **Binding kinetic curves between 4 different scFv antibodies and protective antigen.** 100 nM of scFv antibodies are sequentially injected for binding kinetic measurements with the protective antigen (PA). Those scFv molecules have the same molecular weight, but different dissociation constants with the PA in the range of around 10 pM to 100 nM.

antibodies and PA. Those scFv molecules have the same molecular weight, but different dissociation constants with the PA in the range of around 10 pM to 100 nM. Because of the small molecular weight, the spectral shifts induced due to their binding to the surface are less than 0.1 nm. However, binding kinetics of these small molecules can be still measured because of low background noise level achieved by spectral averaging for each data point. As presented in the section 6.2.1, large-area nanoholes prepared by template stripping allows measuring the transmission spectrum with a very short integration time, leading to a large number of spectral averaging to reduce the noise level. Kinetic parameters, dissociation rate constant (k_d), association rate constant (k_a), and dissociation constant (K_D), are calculated from the kinetic curves shown in Figure 6.12 and compared with values obtained by BIAcore$^{\text{TM}151}$ as summarized in Table 6.1.

	k_d (s^{-1})	k_a (M^{-1} s^{-1})	K_D (M)
L97A (BIAcore)	$1.90 \times 10^{-}2$	3.10×10^{5}	$6.13 \times 10^{-}8$
L97A (Nanohole)	$1.10 \times 10^{-}2$	2.76×10^{5}	$3.67 \times 10^{-}8$
14B7 (BIAcore)	$3.20 \times 10^{-}3$	3.00×10^{5}	$1.07 \times 10^{-}8$
14B7 (Nanohole)	$3.40 \times 10^{-}3$	2.92×10^{5}	$1.17 \times 10^{-}8$
1H (BIAcore)	$1.70 \times 10^{-}4$	6.40×10^{5}	$2.66 \times 10^{-}10$
1H (Nanohole)	$1.58 \times 10^{-}4$	5.47×10^{5}	$2.89 \times 10^{-}10$
M18 (BIAcore)	$4.20 \times 10^{-}5$	1.20×10^{6}	$3.50 \times 10^{-}11$
M18 (Nanohole)	$1.11 \times 10^{-}4$	5.97×10^{5}	$1.86 \times 10^{-}10$

Table 6.1: **Summary of kinetic parameters for scFv molecules and PA measured by BIAcore^{TM} and nanohole array systems.** From the binding kinetic curves shown in Figure 6.12, kinetic parameters, dissociation rate constant (k_d), association rate constant (k_a), and dissociation constant (K_D), are calculated and compared with values obtained by BIAcore^{TM} instrument.

It is seen that those values measured from two different SPR instruments are similar less than an order difference. This verifies the nanohole-based SPR sensors are capable of measuring binding kinetic curves and calculating kinetic parameters accurately even for small molecules.

6.2.4 Template-stripped nanohole arrays with silica shells

Through the chapter, it has been presented that low-cost, but optically superior Ag films can be used as a substrate for nanohole array SPR devices with an alumina protection layer and a new fabrication technique, template stripping, can be used to produce multiple nanohole arrays in large-area for accurate binding kinetic measurements. These two methods can be combined for low-cost, high-throughput fabrication of nanohole SPR device for biosensing applications. As described earlier, Ag has advantageous of better optical properties and lower cost than Au, but the poor chemical stability and

toxicity are barriers for using the material in biosensing. In addition, as-deposited Ag films are typically rougher than Au films,[149] which may cause more scattering loss of SPs. It was shown that these drawbacks can be resolved by using the thin alumina protection layer and the template-stripping method. Therefore, combining these two strategies enable to fabricate smooth Ag nanohole arrays with high throughput. In addition, ALD-grown silica shells play essential roles of protecting both the patterned Ag film and the exposed epoxy substrate while also presenting a uniform surface that is amenable to a wide range of chemical modification techniques. For biosensing, silica is preferred instead of alumina because surface chemistry for silica surface has been well established and the hydrophilic surface of silica allows lipid membrane formation through vesicle rupture as presented in Chapter 5. Figure 6.13 shows SEM images of patterned Si templates and template-stripped Ag nanohole arrays. The periodic nanohole arrays were made in an 8 mm $\times$ 8 mm area centered in a 100-nm-thick Ag film with an area of 26.5 mm $\times$ 26.5 mm as shown in Figure 6.13d. In this scheme, once the reusable patterned Si molds are prepared, metallic nanohole arrays can be easily replicated by a standard metal deposition and one-step peeling process.

Another advantage is that the template-stripped metallic films have smoother top surfaces than films prepared by standard metal deposition techniques such as evaporation as shown in Figure 6.14. The top surfaces of template-stripped Ag nanohole arrays exhibit root-mean-square roughness values below 1 – 2 nm, while as-deposited 100 nm-thick Ag films exhibit roughness of almost 5 nm. Figure 6.15 shows optical characteristics of both bulk and local refractive index sensitivities of the template-stripped Ag nanohole arrays. Figure 6.15a and b show transmission spectra and corresponding spectral shift of template-stripped nanohole arrays as the refractive index of the water-ethanol mixture changes from 1.333 to 1.350. The measured bulk sensitivity is 450 nm/RIU (RIU = refractive index unit). This is about only 10 % lower than the theoretical value calculated with finite-difference time-domain (FDTD) simulations, but higher than previously reported values with similar nanohole dimensions.[39,152] To examine the

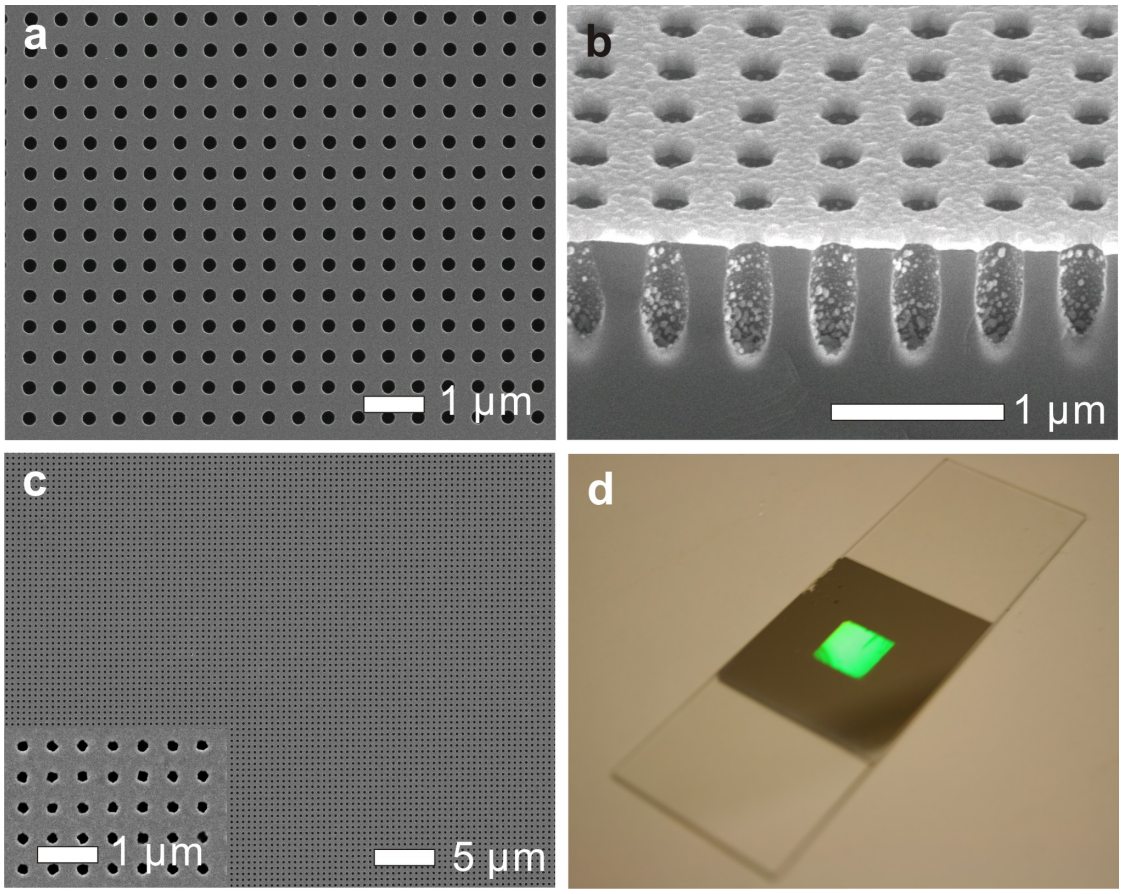

Figure 6.13: **Template-stripped Ag nanohole arrays.** (a) A SEM image of the Si template with deep circular trenches. (b) A cross-sectional SEM image of the Si template after depositing a 100 nm-thick Ag film. (c) A SEM image of the template-stripped Ag periodic nanohole array. The inset shows a zoomed-in image of the template-stripped Ag nanoholes. The diameter of the nanoholes and periodicity of the array are 180 and 500 nm, respectively. (d) A photograph of the fabricated nanohole array chip. A 26.5 mm × 26.5 mm area of 100 nm-thick Ag film with nanohole patterns in an 8 mm × 8 mm area in the center is transferred to a standard microscope slide. Figure is adapted from Im *et al.*[73]

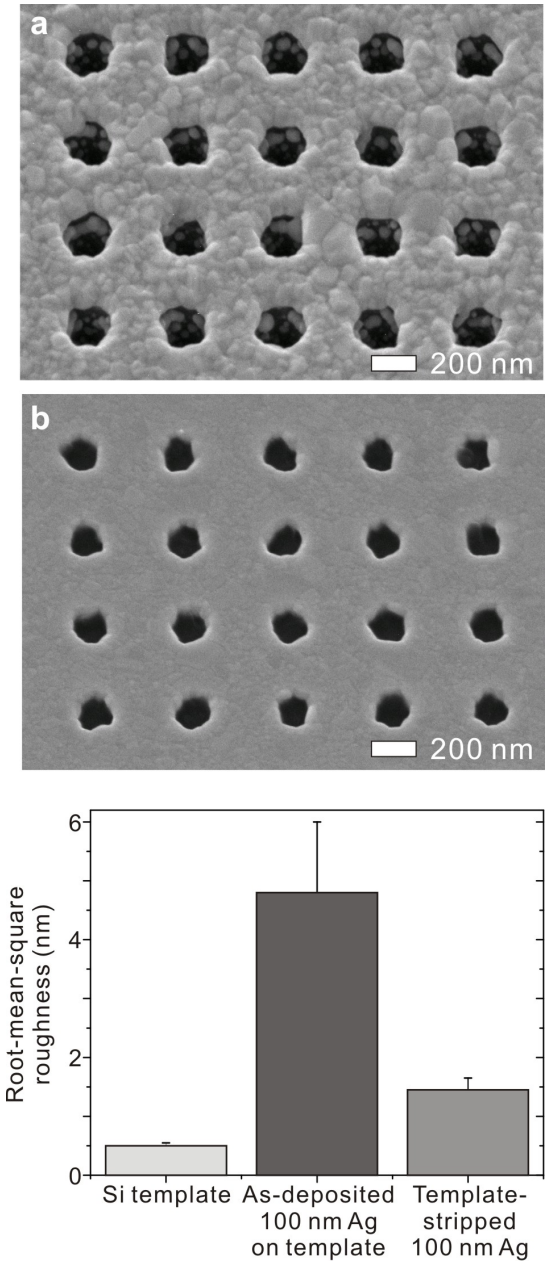

Figure 6.14: **Comparison of surface roughness between as-deposited and template-stripped Ag films.** SEM images of (a) an as-deposited 100 nm-thick Ag film on the Si template and (b) template-stripped Ag nanoholes peeled off of the template in (a). (c) Root-mean-square roughness of the Si template (0.5 ± 0.05 nm), the as-deposited 100 nm-thick Ag film (4.8 ± 1.2 nm) shown in (a), and the template-stripped Ag film (1.45 ± 0.2 nm) shown in (b). Figure is adapted from Im *et al.*[73]

local refractive index sensitivity, thin conformal silica shells were sequentially deposited on the nanohole arrays using ALD. The spectral shifts were measured after depositing sequential 5-nm thick silica overlayers. For comparison, control samples of nanohole arrays made in evaporated and template-stripped Ag films using FIB were also characterized. Figure 6.15c shows the spectral shifts of the template-stripped nanohole arrays with the control samples. The sensitivity of the template-stripped nanohole arrays is similar to the nanohole arrays made by direct FIB milling in a template-stripped Ag film, but about 67 % higher than those made with FIB in as-deposited Ag films. The improved sensitivity can be explained with the reduced SP damping due to the smooth surface. Liu *et al.*, demonstrated that the sensitivity of a Ag SPR sensor can be enhanced by reducing the roughness of an Ag film deposited with a thin Ni seed layer.[153] Previous work demonstrated that the SP propagation lengths on ultrasmooth template-stripped (sub-1-nm roughness) Ag films increased by a factor of 5 to 7 in the visible regime compared with standard evaporated Ag films.[149] In a periodic nanohole system, however, the smooth region between adjacent holes is only a few hundred nanometers in size, and SPs also scatter strongly from each nanohole. Thus, the effect of smoothness on the EOT spectrum is not as dramatic as the propagation length improvements seen in unpatterned films. Nevertheless, template-stripped Ag nanohole arrays include the benefits of high-throughput and low-cost fabrication in addition to the smooth metallic surfaces that improve the overall performance.

For biosensing applications, the template-stripped Ag nanohole arrays were coated with a 15 nm-thick silica overlayer using ALD. Capping the Ag nanohole array with a hydrophilic silica film not only protects its surface but also enables the use of standard surface modification techniques to covalently attach biomolecules or create a supported or suspended lipid bilayer.[53,154,155] As shown in Figure 6.15c, the spectral response of the Ag nanohole array remains linear with the deposition of silica overlayers up to the thickness of 25 nm, indicating that a 15-nm-thick overlayer still provides sufficient sensitivity. In fact, the refractive index of protein layers and phospholipid bilayers are

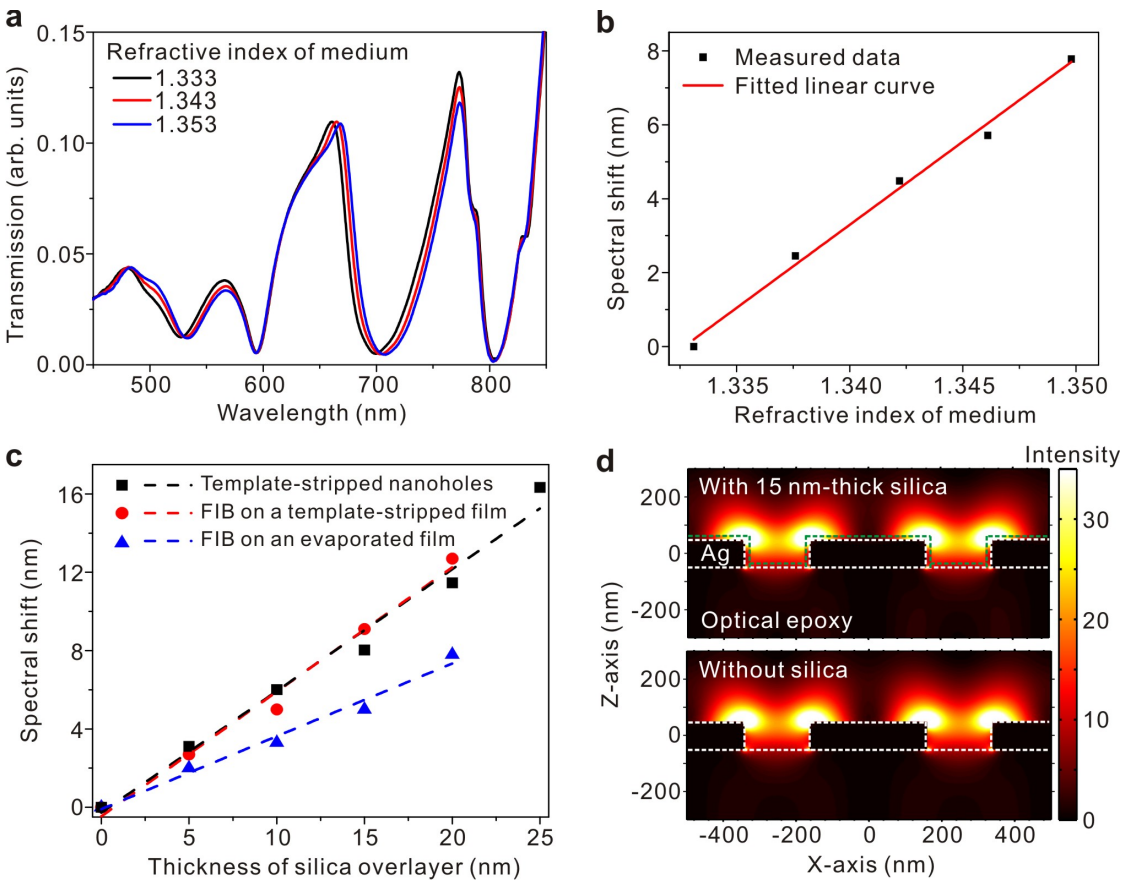

Figure 6.15: **Optical characteristics of bulk and local refractive index sensitivities of template-stripped Ag nanohole arrays.** (a) Transmission spectra of the template-stripped Ag nanohole arrays as the bulk refractive index of a water-ethanol mixture on the Ag film varies from 1.333 to 1.350 (b) Bulk refractive index sensitivity measurements of the fabricated nanohole arrays shown in panel (a). The calculated bulk sensitivity is 450 nm/RIU (RIU = refractive index unit). (c) Local sensitivity measurements of a template-stripped nanohole array with two control samples made by FIB milling on a template-stripped (smooth) and an evaporated (rough) Ag film. In this case, the spectral shift was measured as the thickness of silica shell deposited via ALD increases from 0 to 20 nm. (d) 3-D FDTD simulation of the time-averaged surface plasmon field intensity for template-stripped nanohole arrays with and without a 15-nm-thick silica shell. Figure is adapted from Im *et al.*[73]

close to the refractive index of silica,[30,90] making silica overlayers a useful model for estimating the sensitivity and probing range of plasmonic nanosensors. To visualize this, Figure 6.15d shows the simulated distribution of electromagnetic field intensities around nanoholes before and after depositing the 15-nm-thick silica overlayer. It can be seen that the sizes of hot spots, where strong resonant fields are concentrated around the edges of nanoholes, are larger than the thickness of silica layer and the presence of the overlayer does not reduce the intensity of the field. The 15-nm-thick silica layer is able to protect the Ag nanoholes from harsh oxidizing conditions such as oxygen plasma treatment Figure 6.16a. Therefore, it is also possible to permanently bond a polydimethylsiloxane (PDMS) microfluidic chip and silica-coated Ag nanohole arrays without damaging the underlying nanohole arrays Figure 6.16b.

To demonstrate surface modification of the silica-coated Ag nanohole arrays, the silica surface was chemically functionalized with aminopropyltriethoxysilane (APTES) solutions to form a self-assembled monolayer (SAM), and fluorophores were then covalently linked to the APTES SAM. **Figure 6.16a** shows a fluorescence image of four microfluidic channels. In the leftmost channel, phosphate buffered saline (PBS) was injected as a negative control while the other three channels were incubated with 2 % (v/v) APTES solutions. After 1 hour of incubation, the channels were washed with PBS and 4, 10, and 20 μM of carboxyfluorescein solutions (in the presence of 1-ethyl-3-(3-dimethylaminopropyl)carbodiimide, EDC coupling reagent) were injected for 90 min with a flow rate of 3 μl/min. In the negative control channel, 20 μM of carboxyfluorescein solution was injected. The fluorescence image was taken after washing the channel with PBS for 10 min with a flow rate of 30 μl/min. Figure 6.16b shows the fluorescence intensity from each channel shown in Figure 6.16a. The fluorescence intensity in the negative channel is similar to the level of background noise, and the fluorescence intensity scales linearly with the concentration of carboxyfluorescein solutions injected. This indicates the silica-coated surface can be chemically functionalized by a SAM of APTES and standard coupling chemistry can be used to attach other molecules. In

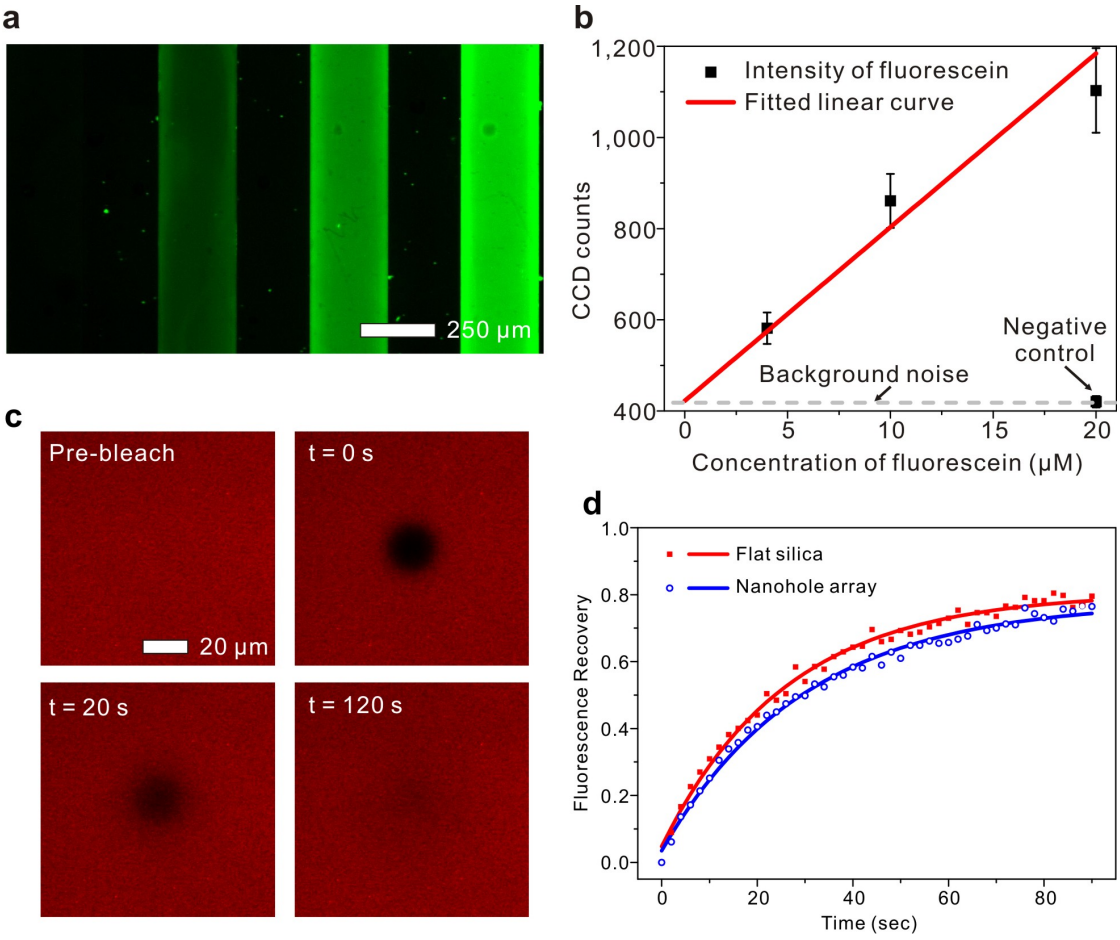

Figure 6.16: **Surface modification of silica-coated Ag nanohole arrays.** (a) A fluorescence image of silica surface functionalized by a self-assembled monolayer of aminopropyltriethoxysilane (ATPES) in 4 microfluidic channels. After functionalizing the silica surfaces with APTES, different concentrations of carboxyfluorescein (20, 10, and 4 μM from the rightmost channel) were injected. The leftmost channel is not functionalized by APTES as a negative control and 20 μM of carboxyfluorescein was injected. (b) The intensity and linear fit of the carboxyfluorescein fluorescence on each channel surface. The intensity from the negative control is similar to the level of background noise, indicating the silica surface is chemically functionalized by APTES and can be used to covalently link different concentrations of molecules in individual microfluidic channels. (c) Frames from a fluorescence recovery after photobleaching (FRAP) experiment on an egg PC supported lipid bilayer with 1 % Rhodamine-PE on the silica-coated Ag nanohole array. (d) Representative FRAP recovery curves for an egg PC membrane on the silica-coated flat surface (red squares) and a nanohole array (blue circles). Figure is adapted from Im *et al.*[73]

addition to surface modification with APTES, the formation of supported lipid bilayers (SLBs) is demonstrated on the silica surface. After allowing Rhodamine B-labeled vesicles to rupture on silica-coated template-stripped smooth surfaces and nanohole arrays, confocal microscopy and fluorescence recovery after photobleaching (FRAP) were used to characterize the resulting fluorescent SLBs. After thorough washing, the SLBs showed uniform fluorescence on both the flat template-stripped areas, as well as the nanohole arrays. FRAP confirms that the SLBs formed on both nanohole array and flat areas are continuous and allow free planar diffusion of lipids. Figure 6.16c shows fluorescence images from different time points during a FRAP experiment for a SLB on a template stripped nanohole array. The nanoholes are not visible in fluorescence mode; however the presence of nanoholes was confirmed by viewing the sample in transmission mode. After photobleaching, fluorescent lipids diffuse into the bleached area and bleached lipids diffuse outward, resulting in the recovery curves shown in Figure 6.16d. Notably, the calculated diffusion coefficient (D) is lower for SLBs over nanohole arrays. The diffusion coefficient over the arrays (D_{array}) was calculated to be 1.90 $\pm$ 0.15 $\mu m^2/s$, while over flat surfaces the diffusion coefficient (D_{flat}) was calculated to be 2.25 $\pm$ 0.09 $\mu m^2/s$ (mean $\pm$ standard deviation). The lower diffusion coefficient over the nanoholes indicates that the membrane probably follows the contours of the nanoporous surface.[76]

For SPR biosensing of molecular binding on SLBs, biotinylated SLBs were formed on the silica-coated Ag nanohole array and a solution containing fluorescently labeled streptavidin-R-phycoerythrin (SAPE) was injected into microfluidic channels to measure binding kinetics of streptavidin to the biotinylated SLBs. The use of fluorescently labeled streptavidin allows simple confirmation of specific binding by fluorescence microscopy. For binding assays, different amounts of biotinylated-phosphatidylethanolamine (biotin-PE) were incorporated into egg phosphatidylcholine (egg PC) vesicles and SLBs of the mixtures were formed in each channel by rupture of the vesicles.[156] A biotin-free egg PC membrane was used as a negative control. After 5 min of baseline with PBS, a

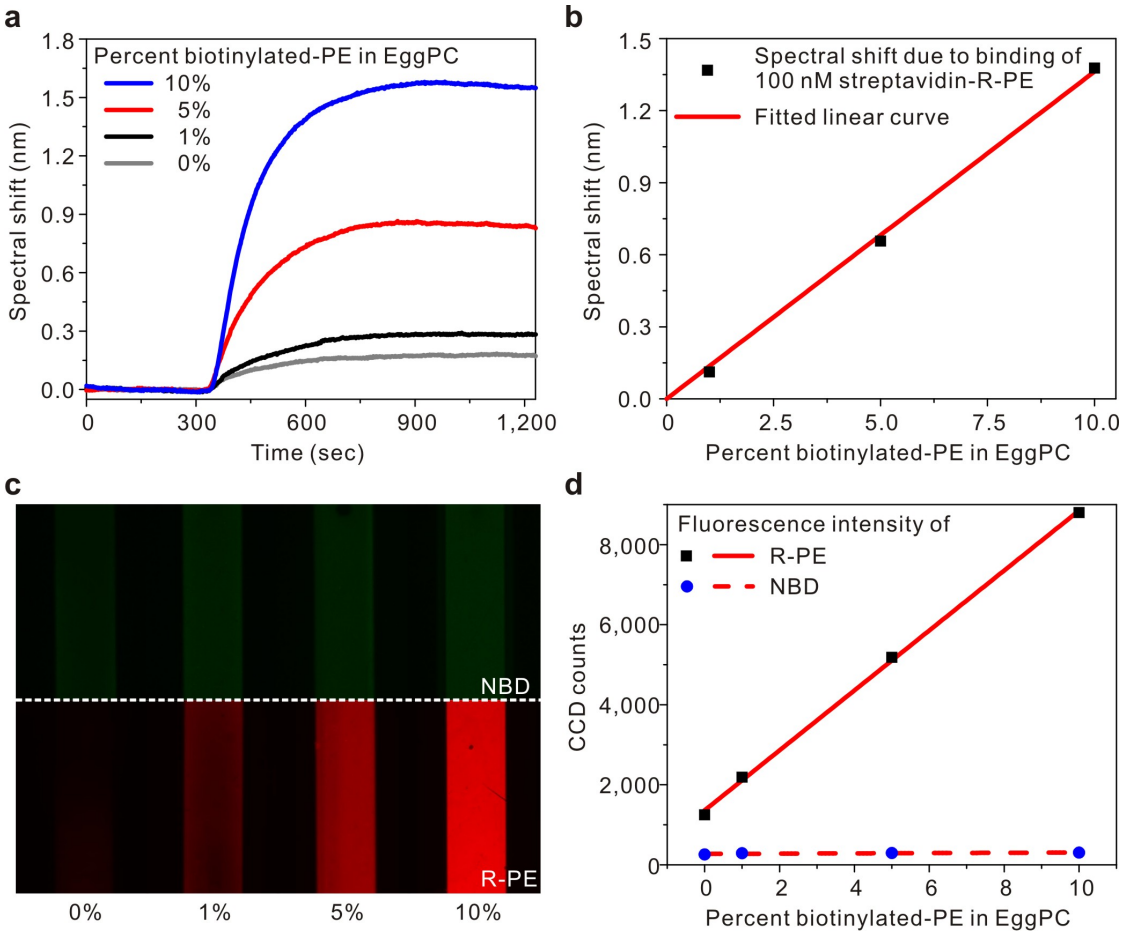

Figure 6.17: **SPR binding assays with biotinylated lipid membranes and fluorescently labeled streptavidin.** (a) Real-time kinetic measurements of 100 nM of streptavidin-R-phycoerythrin (SAPE) and 0, 1, 5, and 10 % biotinylated lipid membranes. After a 5 min baseline with a PBS solution, 100 nM of SAPE in PBS is injected and incubated for 15 min. The flow rate is kept constant at 30 μl/min. (b) The net spectral shift is obtained by subtracting the spectral shift from the binding of SAPE to the non-biotinylated lipid membrane. This eliminates shifts due to bulk refractive index change and non-specific binding of SAPE. (c) Fluorescence images of four channels of nanohole arrays. From the leftmost channel, the percent biotinylated-PE in egg PC membrane increases from 0 to 10 %. The lipid membranes are tagged by 1 % nitrobenzoxadiazole (NBD). Then 100 nM of SAPE are injected through the channels for 15 min. (d) The fluorescence intensity of NBD in the lipid membranes and R-PE after binding with 100 nM SAPE as shown in (c). Figure is adapted from Im *et al.*[73]

100 nM solution of streptavidin-R-Phycoerythrin (SAPE) was injected for 15 min. The flow rate was kept constant at 30 μl/min. Figure 6.17a shows binding kinetics between 100 nM SAPE and egg PC lipid membranes with 0, 1, 5, and 10 % (w/w) biotin-PE as well as 1 % (w/w) nitrobenzoxadiazole-conjugated phosphatidylethanolamine (NBD-PE). The spectral shift shown from the biotin-free egg PC membrane contains a bulk refractive index change and non-specific binding of SAPE. Therefore, the net shift only due to specific binding of SAPE to biotinylated-PE can be obtained by subtracting the kinetic response between SAPE and the biotin-free egg PC membrane from those between SAPE and biotinylated-PE membranes as shown in Figure 6.17b. The net shift after subtracting the signal from the negative control channel is linearly proportional to the percent biotinylated-PE in the SLB, indicating specific binding between SAPE and biotinylated-PE can be quantitatively measured from the differential sensing. Figure 6.17c and d show fluorescence images and intensities of NBD and SAPE after the kinetic experiments shown in Figure 6.17a. The fluorescence intensities of NBD conjugated in the lipid membranes from the four channels are all similar regardless of the amount of biotinylated-PE, but the intensity of SAPE fluorescence increases linearly as a function of the amount of biotin-PE in the SLB. This confirms that the spectral shifts result from specific binding between SAPE and biotinylated-PE membranes.

6.3 Conclusion

In conclusion, this chapter demonstrates strategies to fabricate high-performance nanohole SPR sensors with low cost and high throughput. First, for a material, Ag can be used instead of Au as a substrate for biosensing applications. Despite of its superior optical property, Ag has been less used than Au as a substrate of a SPR biosensor due to its poor chemical stability. However, encapsulation of nanohole arrays with a thin dielectric layer grown by ALD dramatically improves the chemical stability and protects the Ag film from unwanted oxidation. For a fabrication method, a method such as nanoimprint

lithography that can fabricate periodic nanoholes in a large area is of benefit to reduce the background noise level by averaging transmission spectra several times for each data point. As a result, binding kinetics of small molecules can be precisely measured. A new fabrication method, called template stripping, has been demonstrated for high-throughput fabrication of periodic nanohole arrays over nearly centimeter-sized areas in smooth Ag films. Nanoimprint lithography was used to replicate multiple reusable Si master templates. A batch metal evaporation process completes the patterning of nanohole arrays in every mold simultaneously. After curing with an optical epoxy, the patterned metallic films can be stored with the mold and peeled off just prior to use to avoid unwanted contamination or oxidation. Optical transmission spectra from the template-stripped smooth Ag periodic nanohole arrays show intense peaks that respond sensitively to both local and bulk refractive index changes. For biosensing, template-stripped Ag nanohole arrays were coated by a thin silica shell. The resulting sensor chip combines the SPR sensing capability of large-area smooth Ag films with a robust silica surface that can be easily decorated with a variety of biomolecules. A series of experiments including SLB formation, covalent derivatization with APTES, and affinity biosensing with streptavidin and biotinylated lipids demonstrates the utility of this low-cost multi-functional sensor chip. Our fabrication scheme is scalable to high-throughput production because nanoimprint lithography can readily duplicate multiple copies of the reusable silicon nanohole templates, all of which can simultaneously and repeatedly produce centimeter-sized nanohole arrays in a single metal evaporation chamber. Therefore, template-stripping techniques have the potential to enable broad dissemination of the nanohole-based sensing platform to many researchers who cannot routinely access high-resolution lithography equipment in a cleanroom facility.

Chapter 7

Surface-Enhanced Raman Spectroscopy

While SPR biosensors are useful tools for characterizing molecular interactions in a real-time, label-free manner, it does not provide any chemical information of the detected molecules. This is because SPR sensors detect refractive index changes induced by molecular binding and consequently non-specifically bound molecules can induce a false negative response. In contrast, surface-enhanced Raman spectroscopy (SERS), which also relies on the excitation of surface plasmonic resonances, responds to the chemical structures of molecules and therefore provides chemical "fingerprints" to indentify molecules. This unique capability of SERS allows selective detecting of target molecules or identification of unknown molecules, *e.g.* toxin, pathogen, or radioactive waste, from a complex sample mixture.[157] Thus it has been used for a broad range applications including molecular detection,[158] cellular sensing, *in vivo* clinical research,[159] food science,[160] and environmental pollution detection.[161] Because the enhancement of SERS scattering highly depends on the electromagnetic field intensity, this technique is also used to characterize the field distribution of plasmonic devices. In this chapter a brief introduction to SERS is given and different types of SERS substrates are described.

Furthermore, a novel fabrication method for reproducible fabrication sub-10-nm plasmonic nanogap arrays is presented. A portion of contents described in this chapter is derived from following publications:

1. H. Im, K. C. Bantz, N. C. Lindquist, C. L. Haynes, S. H. Oh, *Nano Letter* **10**, 2231-2236 (2010).[162]

2. K. C. Bantz, A. F. Meyer, N. J. Wittenberg, H. Im, O. Kurtulus, S. H. Lee, N. C. Lindquist, S. H. Oh, *Physical Chemistry Chemical Physics* **13**, 11551-11567 (2011).[158]

7.1 Surface-Enhanced Raman Spectroscopy

7.1.1 Raman scattering

In 1928, *Sir* C. V. Raman and K. S. Krishnan reported their discovery of light scattering with "degraded frequency" from the incident beam when the light is scattered by molecules in liquids or gases.[163] This is due to the inelastic collision between the incident photons and the molecules, and bands in the spectrum of scattered light are related to vibrational and rotational motion of molecule.[164] This optical scattering phenomenon is now called Raman scattering named after C. V. Raman.[165]

In light scattering from molecules, the incident photon excites the molecule to a higher energy state. As the molecule relaxes back to a ground state, the released energy is converted into a scattered photon as depicted in Figure 7.1. Depending on the energy difference between the scattered and incident light, the scattering can be categorized as either elastic or inelastic. Rayleigh scattering is an elastic process wherein the light is scattered without loss of energy. In contrast, Raman scattering is an inelastic process wherein incident photons either gain energy from or lose energy to the collided molecule. For example, if when an incident photon with energy $\hbar\omega_0$ is scatter from the molecule and the molecule absorbs the energy of $\hbar\omega_1$, the scattered photon has a lower energy of

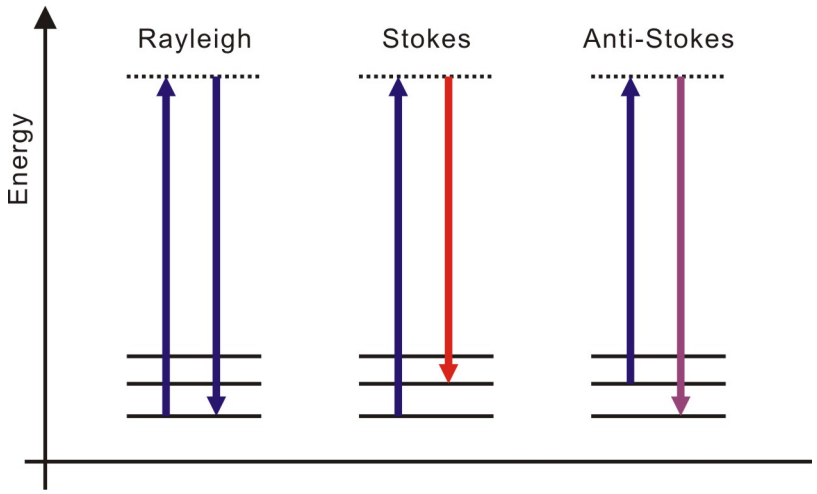

Figure 7.1: **Quantum mechanical model of Raman scattering.** The lengths of upward-pointing arrows are proportional to the frequencies of the incident light and the lengths of downward-pointing arrows are proportional to the frequencies of the scattered light.

$\hbar(\omega_0 - \omega_1)$. This is called *Stokes* scattering. In contrast, if the molecule loses energy, the scattered photon has a larger energy of $\hbar(\omega_0 + \omega 1)$. This is called *Anti-Stokes* scattering. The frequency change of ω_1 is related to vibrational or rotational motions of the chemical structures in the molecule. Therefore, Raman spectroscopy is a valuable tool in mapping out the structures of chemical species in the gas, liquid or solid phase, providing chemical "fingerprints" to identify molecules. Compared to fluorescence, Raman scattering shows sharper peaks, thus enabling a detailed analysis of the analyte molecule. However, Raman is a feeble phenomenon due to small scattering cross-sections in the range of 10^{-29} – 10^{-31} cm^2/molecule compared to fluorescence dyes, which have typical cross-sections of about $10^{-15} cm^2$/molecule. Therefore, Raman spectroscopy typically requires a high-power laser source and a high concentration of analytes, wich has been limiting its widespread practical applications.

7.1.2 Surface-enhanced Raman scattering

In 1974, Fleischmann *et al.* observed an enhanced Raman effect with roughened silver electrodes.[166] Initially, they believed that the enhanced signal derived from an increased surface area of the electrode and thus the number of adsorbate molecules. In 1977, Jeanmaire and Van Duyne, and independently, Albrecht and Creighton, first clarified the Raman signal enhancement of pyridine on Ag electrodes based on electromagnetic and chemical effects.[167,168] This phenomenon is called surface-enhanced Raman scattering (SERS). The signal enhancement factor of SERS over the normal Raman scattering is typically around 10^4 – 10^8. This enhancement of SERS is contributed to by a combination of two mechanisms: the *chemical* and the *electromagnetic* enhancement. The chemical enhancement, typically 10 – 100 times, is attributed to charge interactions between the metal and adsorbate molecules. Thus this mechanism varies depending on both adsorbate and substrate.[169] The electromagnetic enhancement, on the order of 10^4 – 10^8, is a wavelength-dependent effect due to the excitation of localized surface plasmon resonance around the nanostructured noble metal surface.

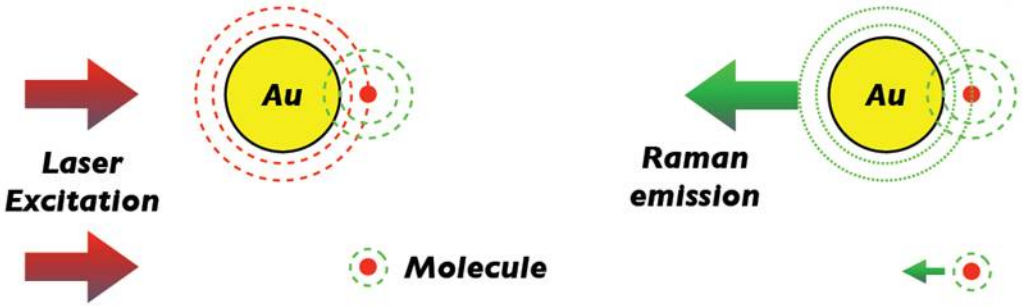

Figure 7.2: **Mechanisms of electromagnetic enhancement.** A gold nanostructure enhances both incident and scattered fields. Because both fields are enhanced, the SERS signal is proportional to a square of field intensity, and the fourth power of the field enhancement factor.

The electromagnetic enhancement is contributed to by two mechanisms depicted

Figure 7.2. First, a metallic nanostructure in resonance excites a strong electromagnetic field localized on the metal surface from the incident light, increasing the field for a proximity molecule. And secomd, the Raman scattered light is also amplified by the same metal structure. Even though the frequency of the scattered photons is shifted, the localized surface plasmon resonance is broad enough to cover both incoming and scattered frequencies. Thus both enhancements can be combined and SERS signal is proportional to the square of the field intensity, and likewise the fourth power of the field enhancement factor. Therefore, it is important to design and develop SERS substrates which can harness strong electromagnetic fields to dramatically enhance the SERS intensity and thus the sensitivity of molecular detection.

7.2 Plasmonic SERS substrates

Since the first discovery of surface-enhanced Raman scattering from roughened noble metal surfaces,[167] many researchers have demonstrated various types of SERS substrates that can harness strong localized surface plasmon resonance (LSPR) and give a significant enhancement of the SERS signal. A substrate with a higher enhancement factor (EF) requires smaller amounts of analytes to detect the SERS signal and with a high enough EF, the SERS signal from a single molecule can be detected. The single molecule detection with SERS was first demonstrated using aggregated metallic nanoparticles.[170,171] Sub-wavelength sized metallic nanoparticles excite strong LSPR and when they are placed close with only 1 – 2 nm spaces inbetween, it creates an even a stronger resonant field between particles than individual nanoaprticles.[172] When nanoparticles are aggregated, they randomly generate SERS "hotspots" where the particles are in close proximity and strong local fields are generated. When a molecule is placed at a hotspot, Raman scattering from the molecule is largely enhanced. Because these colloidal nanoparticles are easily prepared and modified with partition layers that capture and bring target analytes close to the metal surface, a large portion of SERS

research has utilized these aggregated colloidal metallic nanoparticles to detect and identify small molecules, nucleic acids, peptides, and proteins as well as cellular and *in vivo* sensing.[158] While high EFs have been measured from the colloidal nanoparticles, they have the disadvantage of randomly distributed hotspots and thus lack of reproducibility. Practical applications of SERS biosensing requires engineered substrates that can provide reproducible hotspots at desired sites as well as tunable plasmonic properties to achieve the maximum SERS intensity which is achieved when the plasmon resonance wavelength at the substrate is placed near the laser excitation wavelength.[173] Therefore, many groups have been developing new techniques for making various types of engineered SERS substrates. For designing an engineered SERS substrate, the cost to fabricate the substrate as well as the enhancement factor are the primary factors. Electron-beam lithography (EBL) and/or focused ion beam (FIB) milling have been used to make nanostructures with accurate control of sizes and shapes, but these serial writing techniques are slow and very expensive to produce a large number of samples. Therefore, it is desired to develop low-cost and high-throughput fabrication methods that can create metallic nanostructures with strong LSPR.

7.2.1 Nanostructures with nanosphere lithography

Nanosphere lithography (NSL), also called as colloidal lithography, is a facile, inexpensive, and reproducible fabrication method for the production of ordered nanostructures. Different sizes and shapes of nanostructures including indented films, nanoparticles, nanoholes, and nanowires can be fabricated from film deposition, etching, stripping, and/or imprinting with the self-assembled nanosphere arrays as depicted in Figure 7.3. Because of its versatile fabrication capability with low-cost, high-thoughput, and tunability, NSL has been widely used for various SERS substrates.(Figure 7.4) Ag films on nanospheres (AgFON) have been widely used in many biosensing applications of SERS.[174–176] They are simply made by depositing thick ($>$ 200 nm) Ag films on self-assembled nanospheres. Geometric curvatures between the packed nanospheres

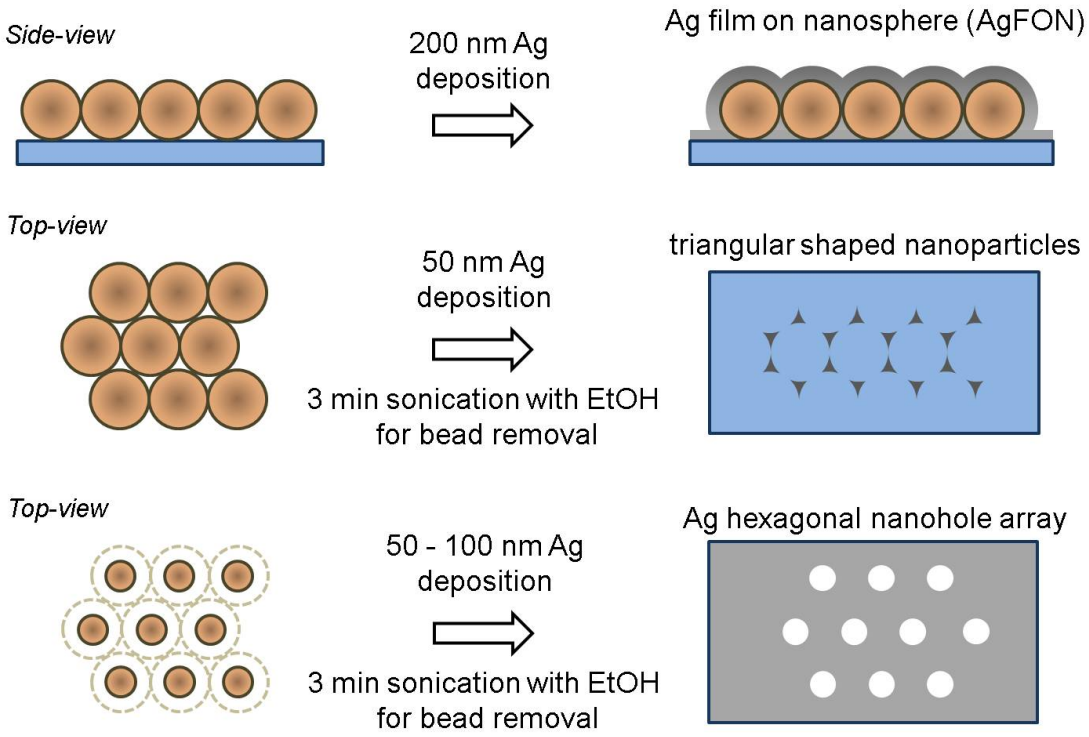

Figure 7.3: **Nanosphere lithography.** Different shapes of nanostructures can be fabricated through simple metal deposition with different thicknesses and/or sphere removal from the self-assembled nanosphere arrays.

make sharp corners where biomolecules fit between two metal surfaces which create intense resonance fields. In addition, the as-deposited rough silver surfaces covering the nanospheres also contribute to the SERS signal. While the field distribution varies with position, it is known that only a few dominant Raman hotspots contribute to the overall signal.[177] The EFs for AgFON are typically in the order of 10^4 – 10^6.[178,179] Another useful structure made by NSL is a triangular nanoparticle array.[180] Thin metal deposition onto self-assembled nanospheres followed by removal of the spheres from the substrate reveals triangular shaped nanoparticles arranged along hexagonal grids. This nanoparticle array has been widely used for both SERS and LSPR spectral

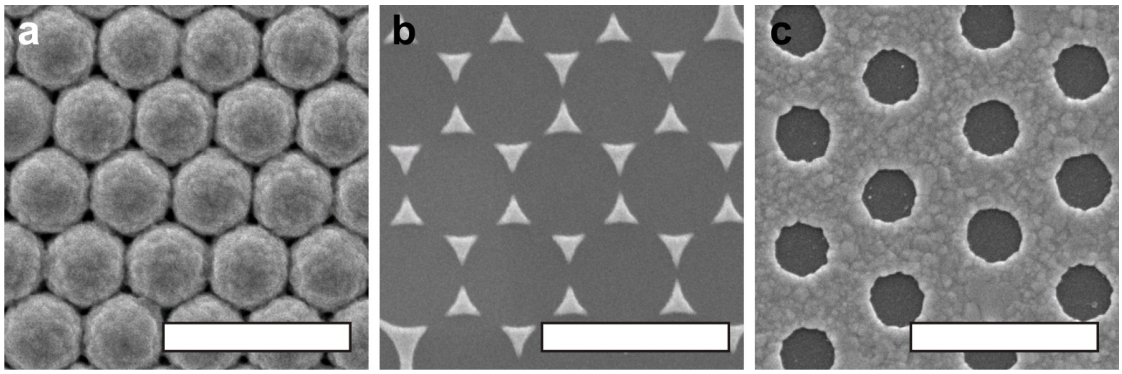

Figure 7.4: **Nanostructures made by nanospheres lithography.** SEM images of (a) Ag film on nanospheres (AgFON), (b) triangular nanoparticles, and (c) ordered nanohole array. These structures are made by nanosphere lithography methods sketched in Figure 7.3.

biosensing.[33,35] In triangular nanoparticle structures, strong electromagnetic fields are confined at the sharp corners,[181] and the field enhancement increases as the distance between particles decreases.[180] The excitation of LSPR in nanoparticles is strongly influenced by the particle size, shape, and inter-particle spacing as well as its material.[180,182,183] Therefore, it is important to design suitable structures tuned to the excitation laser wavelength in order to achieve the maximum enhancement. Additionally, ordered and disordered nanohole arrays are made using NSL.[147,148] To fabricate the ordered nanohole arrays, nanospheres are first arranged into a densely packed monolayer. Subsequent a reactive ion etching (RIE) process reduces the size of nanosphere in a controlled manner. Following to thin metal deposition, removal of the nanospheres reveals a hexagonal nanohole array. For the ordered nanohole array, propagating SPs are excited and their resonance wavelengths are tuned by changing the periodicity and hole size,[152] determined by the initial size of nanospheres used in the NSL and RIE etching time, respectively.[147] In contrast, disordered nanohole arrays, which are made from thinly distributed nanospheres, excite LSPR and the resonance is tuned by the hole size and film thickness. The reported EFs for ordered nanohole arrays are in the

range of 10^4 – 10^5.[147]

7.2.2 Metallic tips

Traditionally, sharp tips have been used in a scanning probe microscope (SPM) for high-resolution imaging of surface roughness, stiffness, electrostatic- and magneto-static fields. When the tips are made of noble metals, similar to triangular nanopartricles, a strong field is confined at the sharp tips from incident light.[184,185] These metallic tips have been used for plasmonic nanofocusing,[150] high-resolution imaging with near-field scanning optical microscope (NSOM),[186,187] and sensing applications.[188] The ability of confining a strong field at a tip is also suitable for application in SERS. Tip-enhanced Raman spectroscopy (TERS) is an emerging new branch of SERS wherein a sharp metallic tip is mounted to the probe of a SPM.[189] Metal-coated SPM tips or thin metallic nanowires have been used for TERS.[190] Because the radius of the tip is much smaller than the diffraction-limited spot size, it allows ultra-high-resolution SERS imaging similar to AFM and NSOM imaging.[191] The combination of SERS detection and SPM imaging is advantageous because it can provide high sensitivity for molecular detection as well as high-resolution mapping of the molecular distribution. Furthermore, TERS is a versatile technique that can extend the utility of SERS because the analyte does not need to be in direct contact with the SERS-active substrate.[192] Theoretical modeling predicts that bringing a tip close to a metallic substrate can increase the local electric field intensity 5000-fold.[193] When a gold tip is brought to within one nanometer of a gold surface coated with benzenethiol molecules, EFs of 10^6 to 10^8 have been reported.[194] In addition, a series of recent studies have established TERS as a promising detection technique with single molecule sensitivity.[193–195]

7.2.3 Nanogap structures

While sub-wavelength metallic nanostructures can excite strong electromagnetic fields, even larger field enhancements are achieved when those metallic structures are spaced

within only a couple of nanometers.[172,181] These nanogap configuration can generate substantial plasmonic electromagnetic fields, and a large SERS enhancement occurs when a SERS-active molecules is positioned within the nanogap. Therefore, a large portion of current SERS research has been focused towards fabricating nanogap structures.

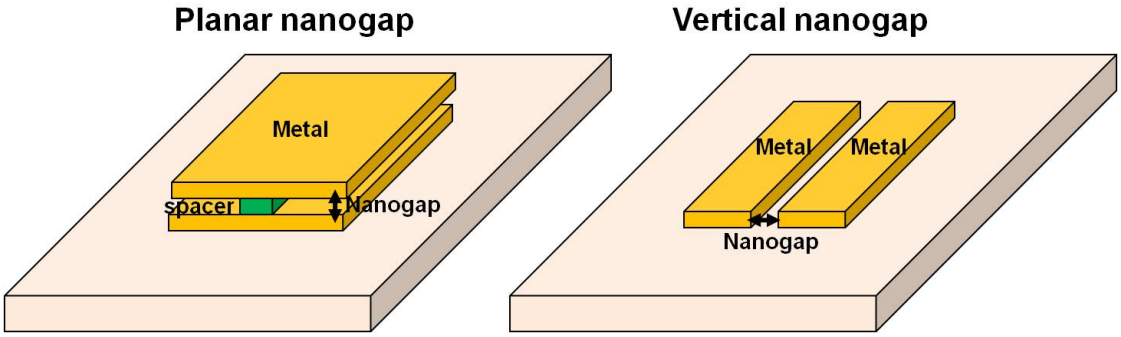

Figure 7.5: **Planar and vertical nanogaps.** Nanogap structures are classified into planar and vertical nanogaps.

Nanogaps are classified into two main structures: planar and vertical nanogaps, as shown in Figure 7.5. In planar gap structures, two metal layers are stacked with a dielectric layer sandwiched in-between. In this configuration, the gap size is determined by the thickness of the sandwiched dielectric layer.[196] This dielectric layer can be deposited by chemical vapor deposition (CVD) and/or physical vapor deposition (PVD) methods. The main advantages of this structure are that the nanogap or cavity structures are simply made through the film deposition process, and the gap size is precisely tuned by the thickness of dielectric layer. Furthermore, atomic layer deposition (ALD) can provide even more accurate control for the film thickness with a sub-nanometer resolution that is not achievable by even the most advanced electron-beam lithography techniques. Miyazaki *et al.* demonstrated nanometric confinement of visible light in a plasmonic nanocavity wherein two metal layers were separated by a 3 nm-thick SiO_2

layer.[197] While the planar nanogap structures are made through simple film deposition, a major limitation in utilizing such planar structures for optical sensing is the difficulty in coupling normally incident light into and out of the in-plane nanogaps since the illumination and collection of the light is shadowed by the metallic overlayers. In contrast, vertical nanogap structures are more suitable to couple with normal incident light and collect scattered light from the nanogaps. Conventional EBL and FIB milling have been used to fabricate vertical nanogap structures, but making sub-10-nm features in a large area is challenging. Therefore, a variety of unconventional approaches including dip-pen lithography[198,199] nanosphere lithography,[180,200,201] molecular lithography,[202] mechanical break junction,[203] electromigration,[204] and electrochemical growth.[205] have been developed for the fabrication of vertical nanogap structures. Although interesting and often effective, most of these techniques are not easily amenable to mass production and the fabrication of a large number of arrays with precisely tuned gap sizes in a large area is still expensive and time consuming.

7.3 Vertically Oriented Sub-10-nm Plasmonic Nanogap Arrays

While several novel fabrication methods have been developed, a reproducible fabrication method, especially one using conventional optical lithography techniques, for the production of sub-10-nm gaps with precise control of the gap's size, position, shape, and orientation remains a significant challenge.

Here, this key fabrication challenge is addressed by using ALD-a technique that can readily achieve film thicknesses with sub-nanometer precision-to form vertically oriented metal-dielectric-metal nanogap structures. Such structures can generate significant field enhancements and tight localization in the gap with normally incident light as shown in Figure 7.6

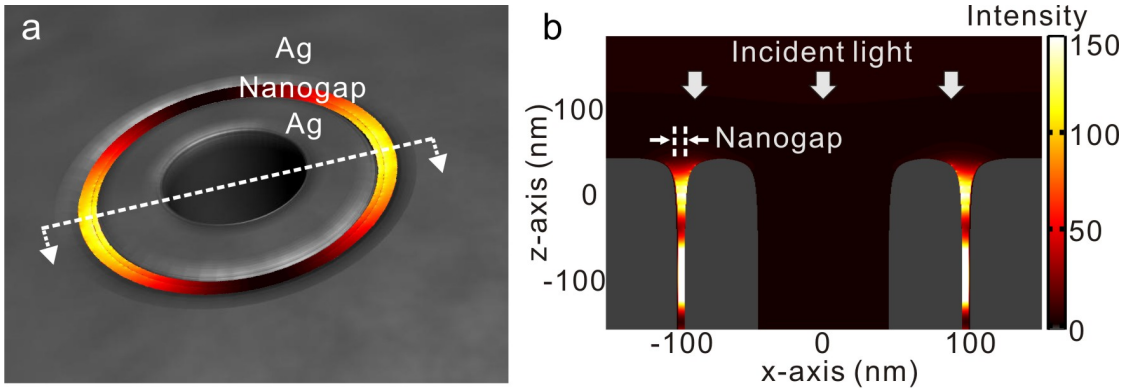

Figure 7.6: **Resonant EM fields inside plasmonic nanogaps.** 3-D finite-difference time-domain simulation results showing significant field intensity enhancement within a 5 nm nanogap from (a) top view and (b) side view. Figure is adapted from Im *et al.*[162]

7.3.1 Fabrication of plasmonic nanogap arrays

The ALD-based new nanogap fabrication process is illustrated in Figure 7.7. First, a 200 nm-thick gold or silver metal film was deposited on a 4-inch Si wafer using electron-beam evaporation, topped with an additional 30 nm Ti hard mask layer. It was experimentally confirmed that the thin Ti hard mask layer aided in steeper sidewall profiles of the metal patterns during subsequent ion milling. For the gold film, a 5 nm-thick Cr adhesion layer was pre-deposited before the gold deposition. Thinner (50 nm) or thicker (250 nm) initial metal films can be also used for the subsequent nanogap fabrication process. A standard optical lithography method or maskless lithography using FIB milling was used to define the initial metal patterns. For optical lithography, a positive-tone photoresist was spin coated on the metal film and the desired patterns were obtained by exposing the resist through a photomask, followed by developing the resist. A negative-tone photoresist was used for inverse structures. The patterned resist was used as a mask for etching the Ti hard mask layer, which is then used as a mask for milling the gold or silver metal film. The maskless FIB milling was used to pattern sub-micron sized features with

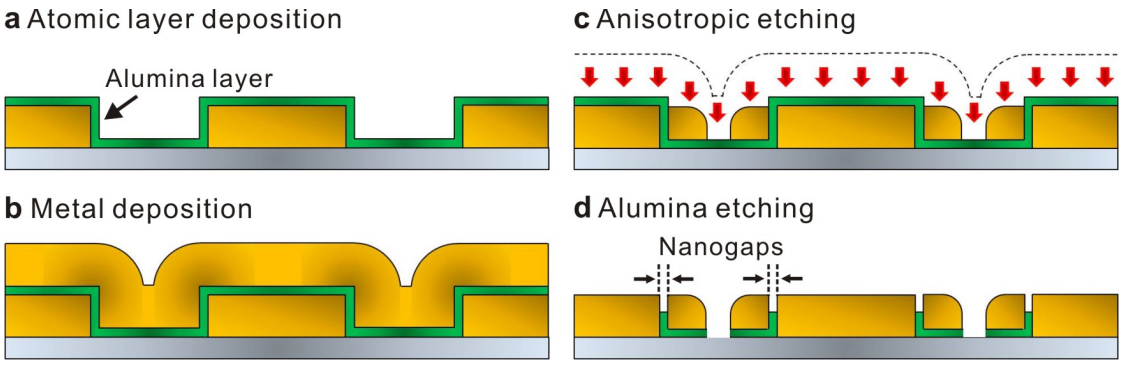

Figure 7.7: **Schematic of fabrication process for nanogap arrays.** (a) A thin alumina layer is deposited on metallic patterns using atomic layer deposition. (b) A secondary metallic film is deposited on the alumina layer using metal evaporation. (c) The second metal layer is anisotropically etched by ion milling until the alumina layer is exposed. (d) The alumina layer is then selectively etched to reveal nanogap structures. The nanogap size is determined by the thickness of the alumina layer. Figure is adapted from Im *et al.*[162]

the various sizes (200 - 1000 nm) and shapes. After patterning the first metal layer, a thin sacrificial alumina (Al_2O_3) layer is deposited using ALD which provides a uniform and conformal layer covering the top and sidewall of metallic patterns.[105] Alumina was chosen because it can be deposited over a wide range of temperatures (50 $\sim$ 300 °C) with a slow deposition rate (1.1 – 1.8 Å/cycle) and is easily etched by a buffered oxide etchant (BOE) solution with a high selectivity to the underlying metal films. The alumina films are deposited on Au patterns at 250 °C and on Ag patterns at 50 °C to minimize the oxidation of Ag during the ALD process.100 The deposition rate of alumina was 1.1 and 1.8 Å/cycle at 250 and 50 °C, respectively. The thickness of the alumina layer, controlled by the number of ALD cycles, determines the size of nanogap. Besides alumina, other dieletric materials such as hafnia (HfO_2), titania (TiO_2) or silica (SiO_2) may also be used as the sacrificial spacer layer depending on fabrication process and applications.

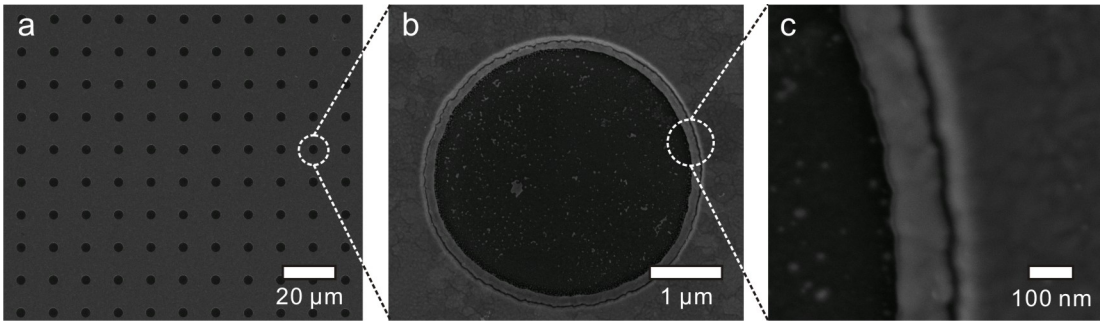

Figure 7.8: **Nanogap arrays fabricated using optical lithography.** (a) SEM image of a nanogap array with a circular pattern defined via optical lithography. (b) The magnified image of a single ring-shaped element shown in panel b. (c) The magnified image of the 10-nm nanogap formed along the ring-shaped pattern. Figure is adapted from Im *et al.*[162]

After the deposition of a second metallic layer on the alumina-coated metallic patterns, anisotropic ion milling is performed to create metallic sidewalls spaced by the now exposed alumina. Because the etch rate of the alumina layer against the ion milling is negligible, it acts as a etch stop during the process. The alumina was subsequently etched by a BOE solution, forming vertically oriented metal-air-metal nanogap structures with the precisely controlled gap size defined by the thickness of the conformal alumina layer. Figure 7.8 shows a circular gold-air-silver nanogap array, where the Au circular patterns were defined using optical lithography over a 4-inch Si wafer. Each circle in the Au film contains a 10-nm nanogap structure along its Ag inner wall. Using photoresist with opposite polarity, inverse structures were also made as shown in Figure 7.9.

Because a continuous nanometric gap is created along the perimeter of the patterned metal areas, the nanogap shape conforms with the first metal layer patterned, providing a wide variety of design options for making SERS substrates and plasmonic devices. Various other silver-air-silver nanogap structures, where the initial patterns were defined using FIB milling, are shown in Figure 7.10. The key advantage of this fabrication

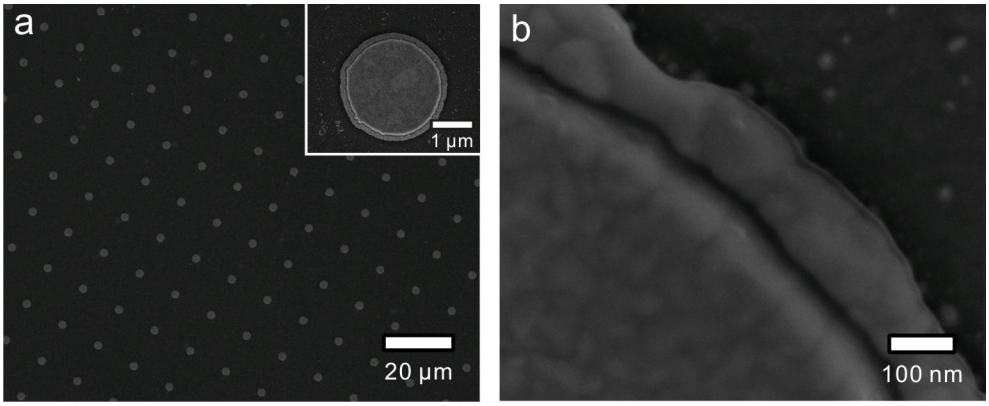

Figure 7.9: **Nanogap arrays fabricated using optical lithography.** (a) SEM image of a nanogap array made with pillar patterns using the opposite polarity of photoresist than used in Figure 7.8. The inset to panel a shows the magnified image of a single ring-shaped element shown in panel a. (b) The magnified image of the 10-nm ring-shaped nanogap formed along the pillar pattern. Figure is adapted from Im *et al.*[162]

scheme is the ability to precisely control the gap's size, shape, position, and orientation and to confine and manipulate SPs and their associated high field intensities along the entire vertically oriented metal-air-metal nanocavities.[206]

7.3.2 Characterization of nanogap arrays for SERS

To characterize the SERS performance of the fabricated nanogap arrays, nanogap substrates were incubated in 1 mM benzenethiol (BZT), a well-characterized and efficient Raman scatter, and AgFON substrates[207] were used as reference samples. While the field distribution varies with position on the AgFON substrates, the fabricated nanogap arrays provide well-defined, high-density hotspots along the entire length of the nanogap. Confocal Raman microscopy is used to characterize the nanogap arrays by imaging the spatial distribution of hotspots and calculating SERS enhancement factors from individual hotspots. A diffraction-limited 514.5 nm laser spot was scanned over the substrates, and Raman spectra were collected as a function of position. Each pixel in the images

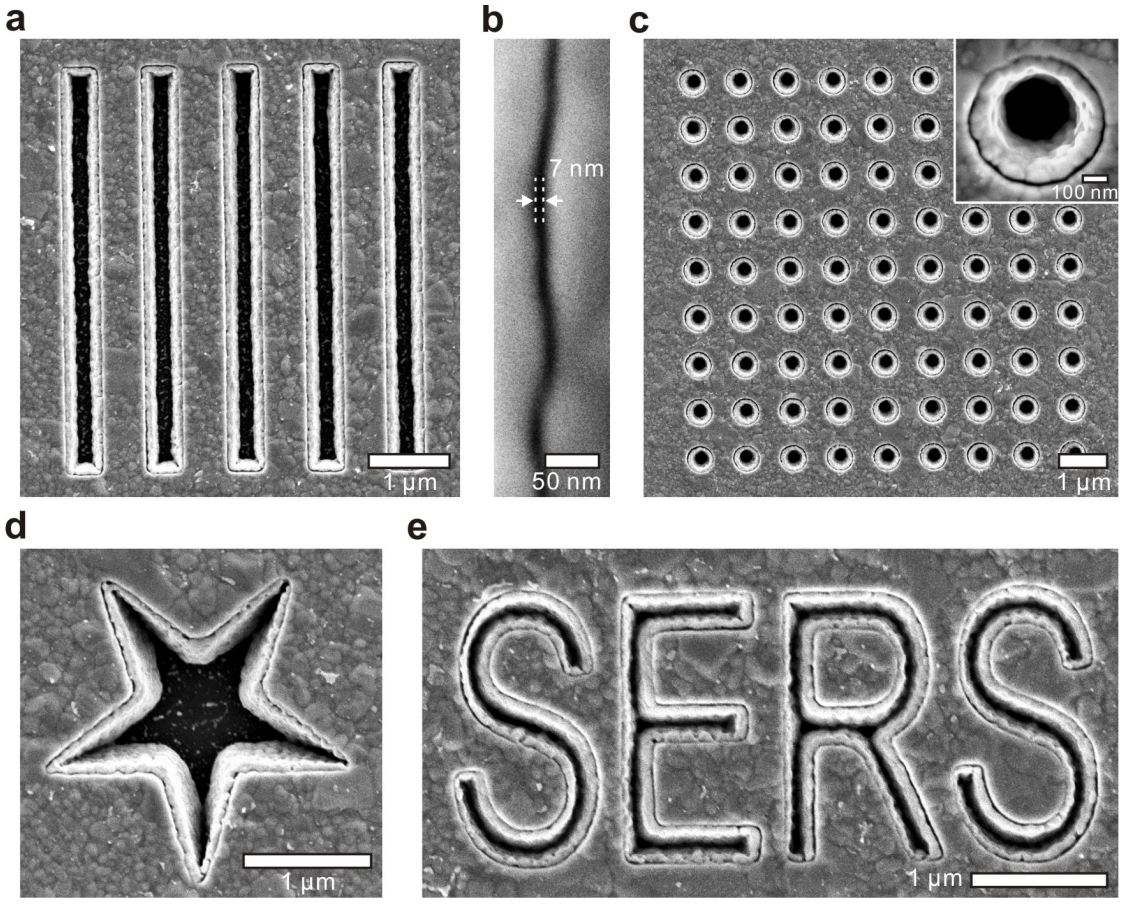

Figure 7.10: **Various shapes of nanogap arrays.** SEM images of nanogaps made in (a) slit array with 500 nm width and 1.5 μm periodicity. (b) the magnified image of 7 nm nanogap from a slit pattern shown in panel a. (c) 9 $\times$ 9 nanohole array with 500 nm diameter. The inset to panel c shows the magnified image of one of holes. (d) nanogap on a single star shaped substrate. (e) nanogap formed along a "SERS" character pattern. Figure is adapted from Im *et al.*[162]

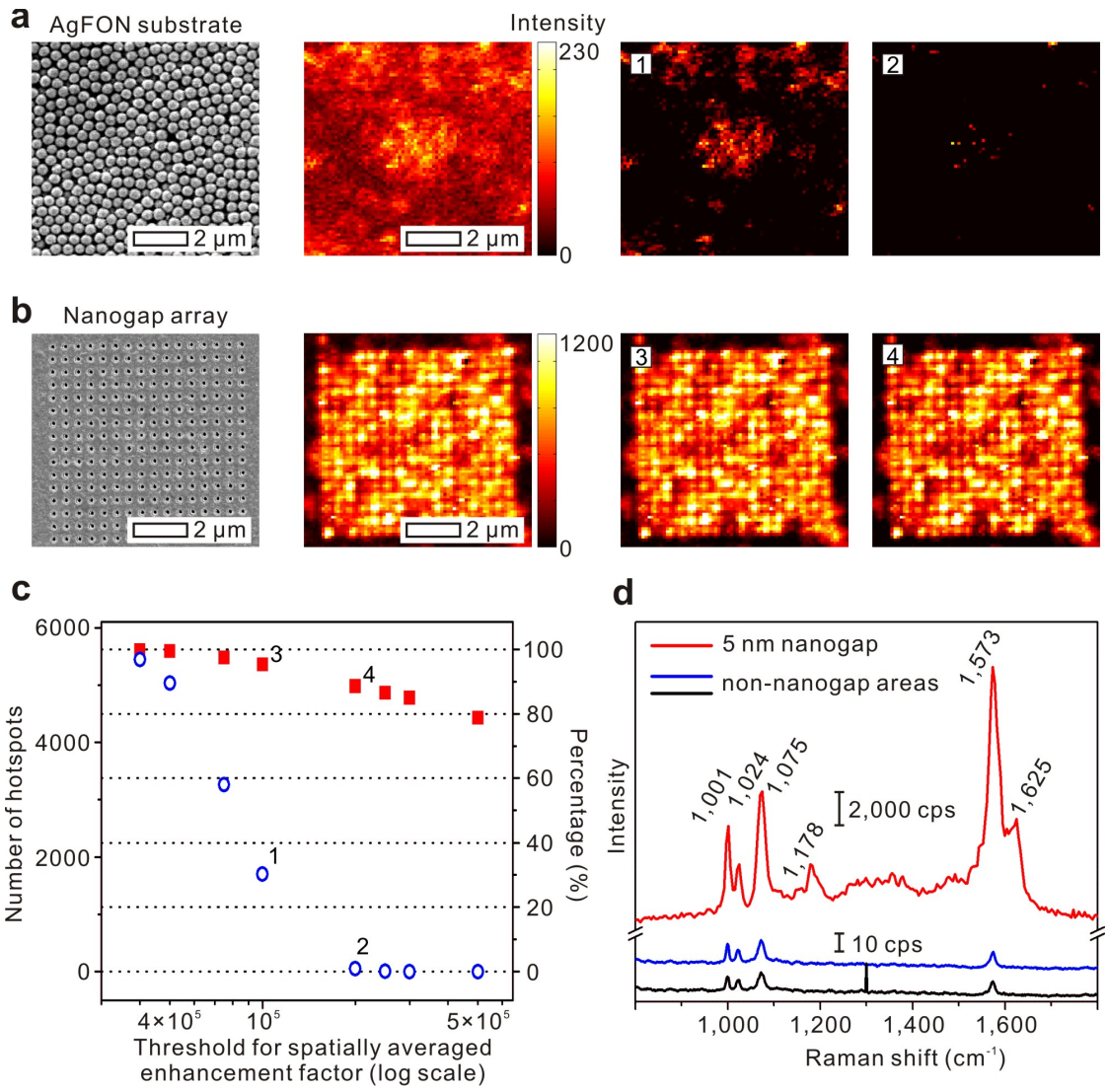

Figure 7.11: **Characterization of nanogap arrays with confocal Raman imaging.** (a) Confocal Raman imaging of a Ag film over nanosphere (AgFON) substrate and (b) nanogap array of hole patterns with different spatially averaged EF thresholds (1×10^5 and 2×10^5 in panels 1/3 and 2/4, respectively). (c) The number of SERS hotspots on the AgFON substrate and the nanogap array with different spatially averaged EF thresholds. (d) Comparison of Raman spectra of benzenthiol from nanogap (red line) and non-nanogap (blue and black lines) areas. Figure is adapted from Im *et al.*[162]

represents the intensity of the band at a 1,075 cm^{-1} shift, corresponding to an aromatic breathing mode in BZT. While an 8× 8 μm^2 area of an AgFON substrate shows randomly distributed hotspots (Figure 7.11a), a nanogap device made on a nanohole array with an ALD-defined gap size of 5 nm shows a more homogenous distribution over the same sized area with stronger Raman signals for the same incident laser power.(Figure 7.11b) In terms of spatially averaged enhancement factor (EF), clearly the nanogap device has a significantly higher density of hotspots with a spatially averaged EF above 1×10^5 and 2×10^5 then the AgFON substrate. Less than 30 % of the AgFON substrate has spatially averaged EFs above 1×10^5, while the nanogap sample shows more than 90 % coverage. This drops only slightly when the threshold is raised to 5×10^5, whereas less than 1 % of the AgFON area exceeds this EF. (Figure 7.11c) Additionally, the nanogaps exhibit a signal-to-background contrast of more than 500 between nanogap and non-nanogap areas. (Figure 7.11d) It should be noted that the nanogap EFs calculated here are spatially averaged over the spot size of the incident laser. Typically, the enhancement factor of SERS is calculated from the ratio of signal density of SERS scattering to the signal density of normal Raman scattering expressed by the following equation:

$$\mathrm{EF} = \frac{\frac{I_{surf}}{N_{surf}}}{\frac{I_{vol}}{N_{vol}}} = \frac{N_{vol} \times I_{surf}}{N_{surf} \times I_{vol}} \tag{7.1}$$

where N_{vol} is the number of BZT molecules contributing to the bulk liquid Raman signal, N_{surf} is the number of BZT molecules contributing to the SERS signal, and I_{surf} and I_{vol} are the intensities of the scattering band of interest in the SERS and bulk liquid Raman spectra, respectively. The spatially averaged enhancement factor was calculated by considering the surface area defined by the confocal spot size and nanogap structures. With the packing density for BZT on an Ag surface, 6.8×10^{14} molecules/cm^2,[208,209] the value of N_{surf} was calculated. While the spatially averaged enhancement factor is a good practical measure of substrate utility, there is significant

interest in the local enhancement factor achieved within the nanogap structure. Because the SERS signal is predominantly contributed to by the nanogap structures as shown in Figure 7.12d, it can be assumed that the SERS signal is mostly coming from the nanogap structures while the contribution of SERS signal collected from outside the nanogap arrays is negligible. The local EFs are also calculated by assuming that a single-molecule-wide stripe of the BZT molecule with a molecular footprint of 0.15 nm^2 along the top edge of the nanogap contributed the majority of the SERS signal. It was experimentally shown that the Raman signal from a non-nanogap area (background) is less than 1 % of that from a nanogap area Figure 7.11d, supporting this assumption. Table 7.1 summarizes the surface areas used to calculate spatially averaged and local EFs of 5 nm nanogap structures with various sizes and shapes. Based on these values, the spatially averaged and local enhancement factors were calculated and plotted in Figure 7.12.

	Surface area (cm^2)	
	for spatially averaged EF	for local EF
200 nm slit	1.27×10^{-10}	2.94×10^{-12}
500 nm slit	2.25×10^{-10}	1.83×10^{-12}
1000 nm slit	2.25×10^{-10}	1.83×10^{-12}
200 nm hole	3.02×10^{-10}	2.18×10^{-12}
500 nm hole	3.41×10^{-10}	1.90×10^{-12}
1000 nm hole	5.10×10^{-10}	1.83×10^{-12}

Table 7.1: **Surface areas of nanogap arrays.** Surface areas used to calculate spatially averaged and local EFs of 5 nm nanogap structures. Table is adapted from Im *et al.*[162]

Figure 7.13 shows the calculated local EFs for various fabricated nanogap structures with different gap sizes ranging from 5 to 20 nm. A patterned substrate without an ALD step (no nanogap) has spatially averaged EFs less than $\sim 10^5$ whereas a 20 nm-gap structure has spatially averaged EFs of $\sim 10^6$ and a local EF of $\sim 10^8$. The EF

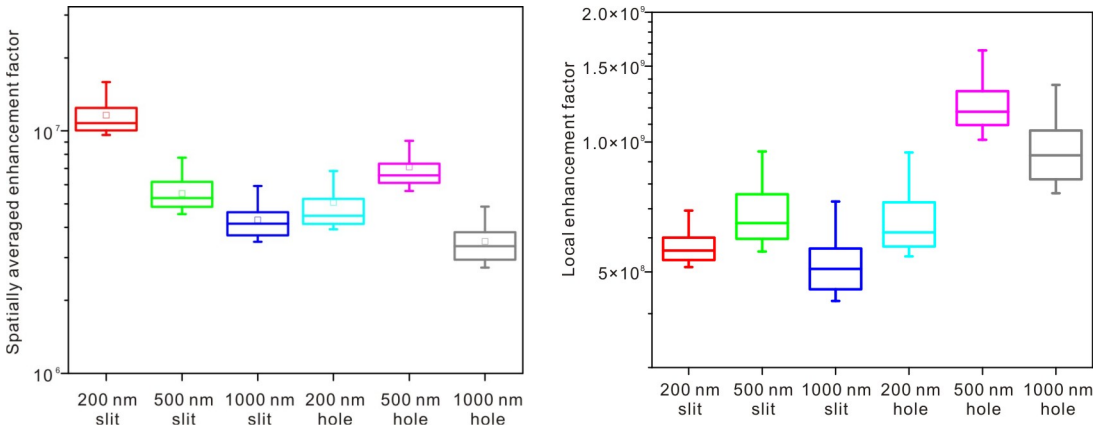

Figure 7.12: **The enhancement factors of 5-nm nanogap arrays.** The spatially averaged and local enhancement factors of 5-nm nanogap arrays with different nanogap shapes were compared. Figure is adapted from Im *et al.*[162]

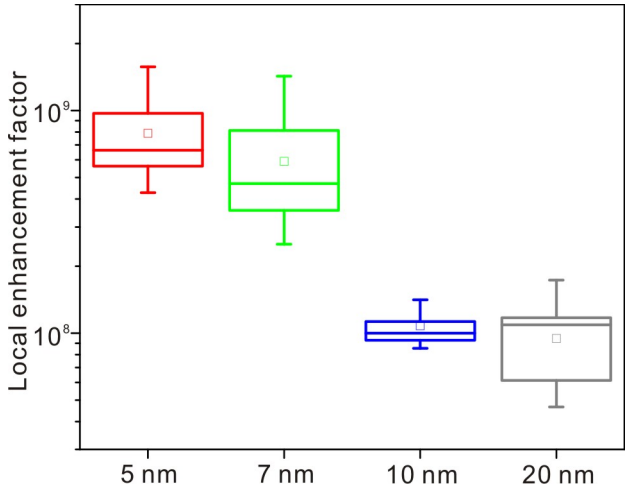

Figure 7.13: **The local enhancement factors of nanogap arrays.** The local EFs of nanogap arrays with nanogap sizes ranging from 5 to 20 nm are compared. Lines in error bars represent values of minimum, 25 %, median, 75 %, and maximum, and a square represents the mean value. Figure is adapted from Im *et al.*[162]

increases as the nanogap size decreases, and a 5 nm gap structure has spatially average EFs above 10^7 with the maximum local EF value exceeding $\sim 10^9$. This behavior of increasing EFs with decreasing gap size is consistent with theoretical calculations.[181] From the EFs shown in Figure 7.12 and 7.13, it is experimentally demonstrate that the gap size is a primary factor that determines the local EFs.

7.3.3 Polarization dependency

With these metallic nanogap structures, the SERS intensity is maximized when the incident light is polarized across the gap and minimized when the polarization is parallel to the gap.[210,211] For 10-nm gap devices, the number of hotspots decreases by more than two-fold when the incident polarization is switched parallel to the nanogap (Figure 7.14a). Because the lithographically defined sidewall exhibits its own nanoscale roughness as seen in Figure 7.10b, some hotspots will still remain with the parallel polarization. With square patterns, it is clearly seen that the SERS hotspots are redistributed according to the incident polarization.(Figure 7.14b) In Figure 7.14c, with a vertical polarization, the nanogap areas marked as "1" are aligned perpendicular to the incident polarization and show a signal intensity approximately three times higher than the orthogonal regions "2". This is reversed with horizontal polarization.

7.4 Large-Area Nanogap Fabrication with Nanosphere Lithography

In the previous section, the high-throughput fabrication of sub-10 nm plasmonic nanogap arrays is demonstrated via the conformal deposition of ultrathin sacrificial layers using ALD on the vertical sidewalls of patterned metal films. The gap size is precisely controlled by the ALD film thickness, and the nanogap is aligned vertically, enabling simple optical excitation and collection over a large area and An array of densely packed 5-nm gaps exhibits high density SERS hotspots with local EFs exceeding 10^9. Combining this

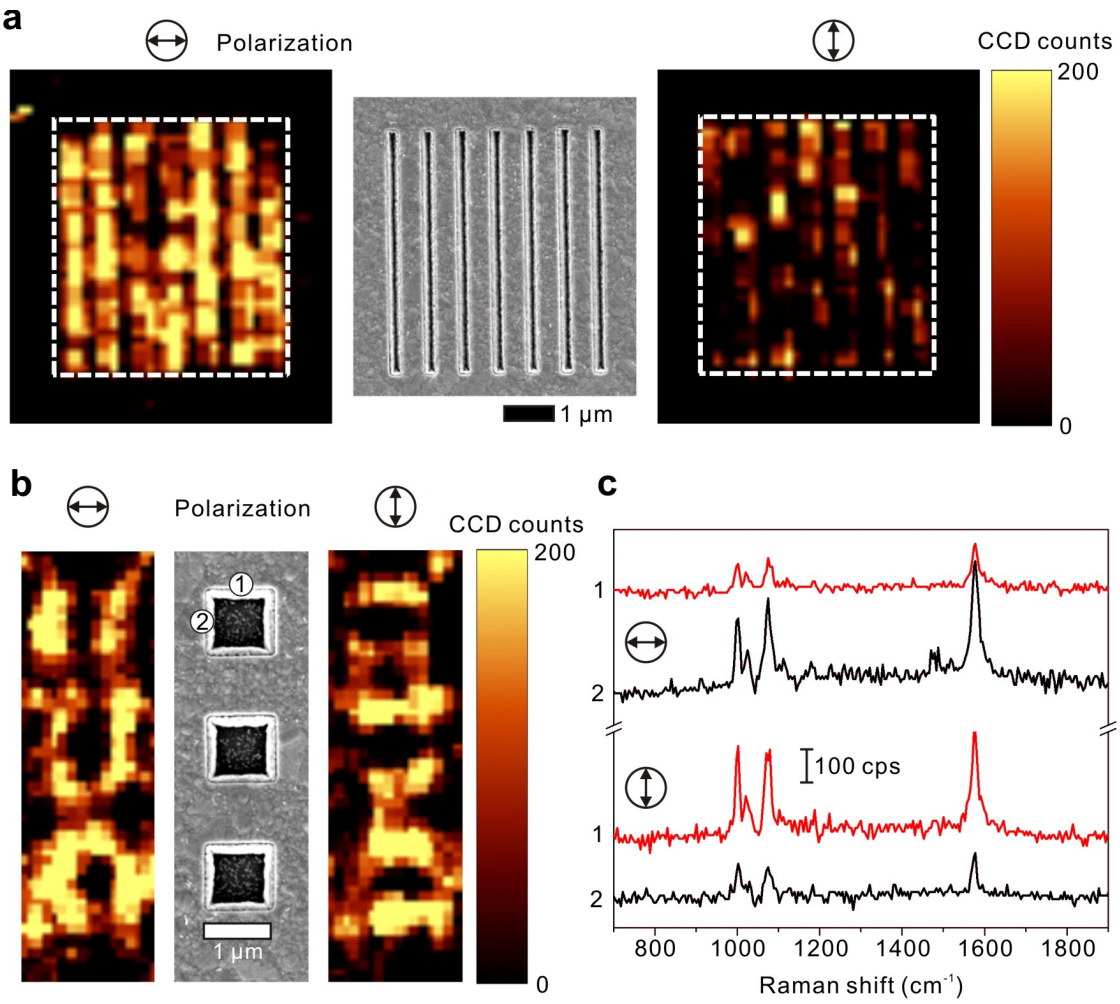

Figure 7.14: **Polarization dependency of Raman signal.** (a) Confocal Raman imaging of nanogaps in slit patterns with two different polarization directions of the incident laser beam. (b) Confocal Raman imaging of nanogap in 1 μm $\times$ 1μm square patterns, showing the modulation of hotspots along the polarization direction. (c) Corresponding Raman spectra from two areas indicated in panel b with two different incident beam polarizations. Figure is adapted from Im *et al.*[162]

method with high-throughput nanofabrication techniques such as nanosphere lithography allows these nanogap structures to be easily and inexpensively fabricated over large areas and provide versatile substrates for reproducible and efficient SERS detection.

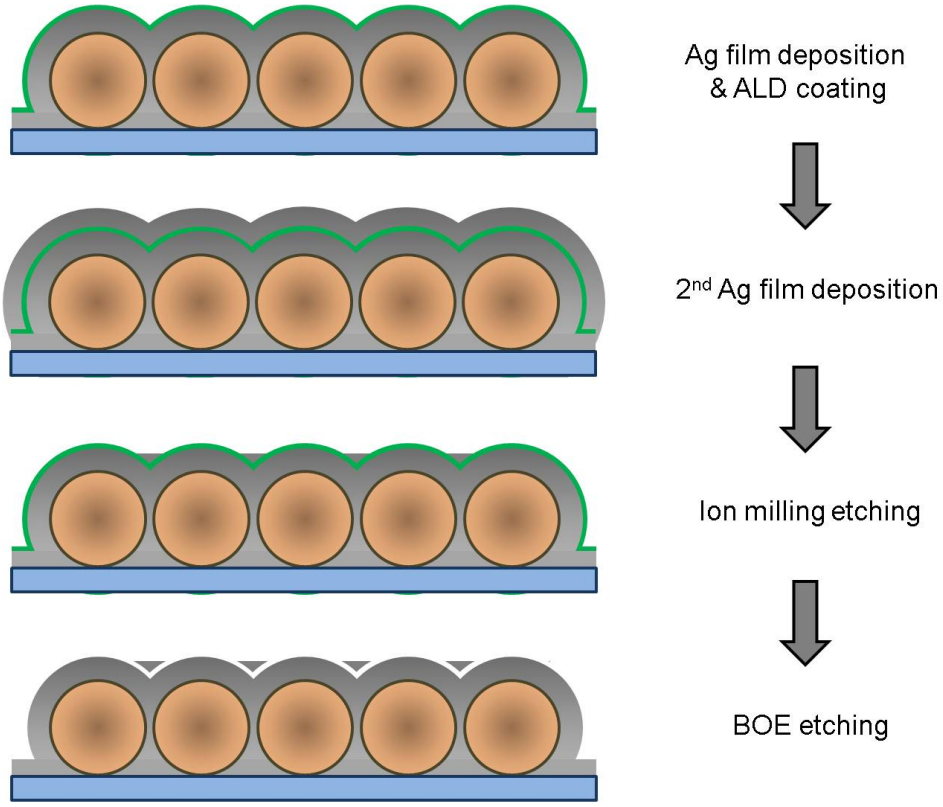

Figure 7.15: **High-throughput fabrication of nanogap structures.** Combining with nanospheres lithography allows the high-throughput fabrication of nanogap structures in a large area. Starting from AgFON substrates, subsequent ALD coating and metal deposition, followed by anisotropic ion milling and BOE etching make uniform nanogap structures over patterns on AgFON substrates.

Figure 7.15 shows the fabrication scheme forming nanogap structures over AgFON substrates using a similar approach using the ALD sacrificial layer. After ALD of thin sacrificial layer and metal deposition on the AgFON substrate, the metal layer is anisotropically milled until the alumina layer is exposed. Partially etching the alumina

layer by BOE reveals the gap structures formed along the patterns on the AgFON substrates. Figure 7.16 shows SEM images of the fabricated nanogap structures on the AgFON substrate. Because the AgFON substrates provides initial patterns, and the nanogaps are formed along the patterns on the AgFON substrates, the high-throughput low-cost fabrication of uniform nanogap arrays in a large are with high packing density are readily achieved through simple film deposition and subsequent etching processes. The new fabrication method would be a benefit to a broad range of SERS application by providing reproducible and high-sensitive SERS substrates.

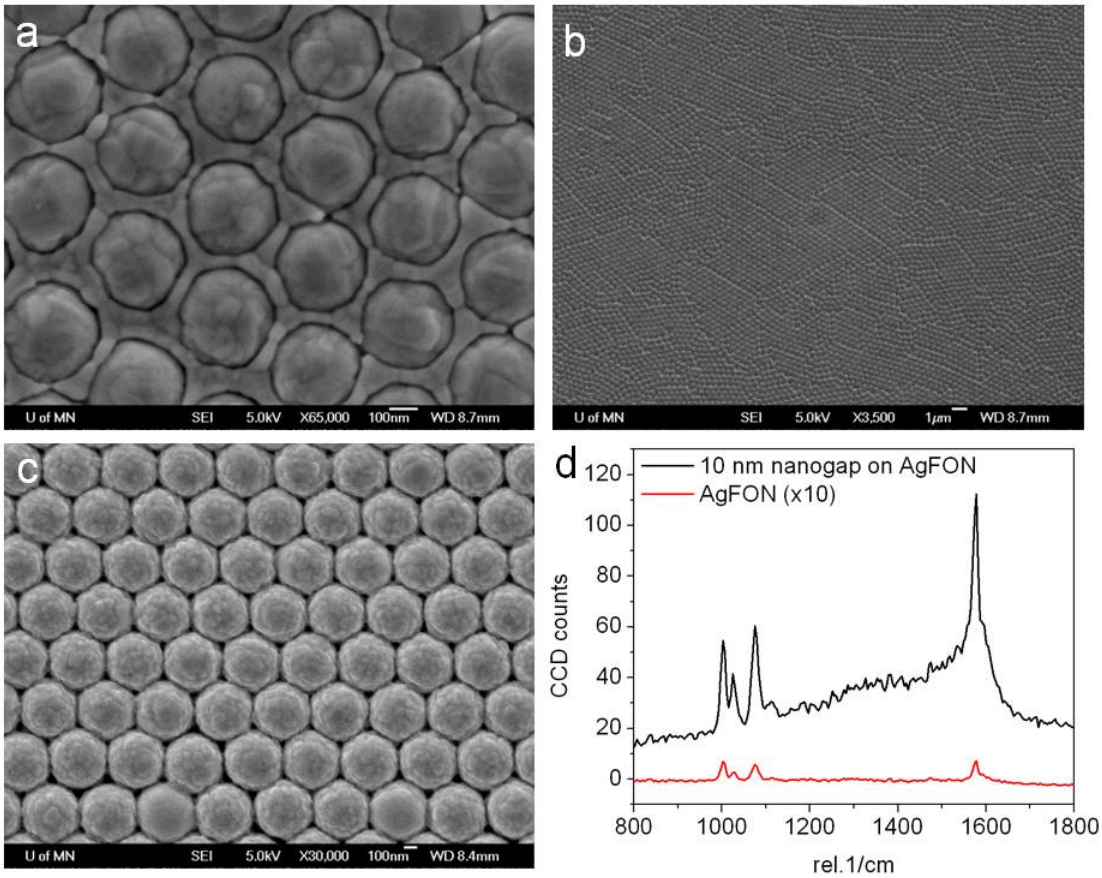

Figure 7.16: **The fabricated nanogap structures on the AgFON substrate.** SEM images of (a) 10-nm nanogap structures formed on AgFON substrate, (b) long-range order of nanogap structures on AgFON substrate, and (c) regular AgFON substrate without nanogap structures. (d) Comparison of SERS spectra of BZT with and without nanogap structures on the AgFON substrates.

Chapter 8

Conclusions and Future Directions

This chapter summarizes SPR biosensing research described in the previous chapters and presents future research directions of on-going projects along with primary data.

8.1 Dissertation Overview and Conclusion

This dissertation presented new nanostructured materials and surface plasmon resonance (SPR) devices for biosensing applications. Periodic nanohole arrays made in optically thick metallic films exploit the extraordinary optical transmission (EOT) effect, mediated by SPs excited on the metallic nanostructures. The refractive-index sensitive resonance condition and corresponding shifts in spectral peak positions due to molecular binding on the sensing surface enable label-free sensing of molecular binding interactions. Real-time measurements of binding kinetics provide essential information of binding rates and affinity between molecules for new drug discovery and quantitative proteomics research. Compared to conventional SPR instruments, which operate in reflection mode with angled incident light, the nanohole-based SPR sensors utilizes a co-linear transmission optical setup, allowing high-resolution imaging. This facilitates

high-throughput multiplexed SPR imaging, which monitors intensity changes induced by spectral shifts due to molecular binding, from a large number of sensing arrays simultaneously for protein microarray applications. Because more than a million nanohole arrays can be packed in a mm2 area, thus this high-resolution, multiplexed SPR imaging technology could significantly speed up a molecular screening process than conventional methods for pharmaceutical development. Integration of nanohole SPR devices with lipid membranes provides a versatile sensing platform to study many clinically important antibodies that associate with cellular membranes and perform therapeutic functions. The unique geometry of nanopore arrays enables the formation of pore-spanning lipid membranes. This provides a natural platform for studying transmembrane proteins without the undesirable effects caused by the presence of underlying solid substrates in conventional SPR instruments. Vesicle rupture on a silica hydrophilic layer over the nanopore array is compatible with cell plasma membranes and membrane proteins integrated therein. Therfore this platform could potentially be employed for characterizing ligand binding to transmembrane proteins such as G protein-coupled receptors (GPCRs) and ion channels associated with diseases. The fabrication of plasmonic nanohole arrays over a large area enables significant reduction in background, enabling the characterization of small molecules with a low detection limit. With a new fabrication method, called template stripping, smooth metallic nanohole arrays with the improved sensitivity are reproducibly fabricated from simple metal deposition and film stripping steps. Nanoimprint lithography followed by template stripping is scalable to high-throughput production because nanoimprint lithography can readily duplicate multiple copies of reusable Si nanohole templates, all of which can be used to produce centimeter-sized nanohole arrays in a single metal evaporation and stripping process. Additionally, encapsulating inexpensive, but optically excellent Ag nanohole arrays with a dielectric layer not only improves the chemical stability of Ag film, but also provides a robust surface that can be readily functionalized by molecular layers and lipid membranes for a wide range of biosensing applications. Combining these techniques has the potential to

enable broad dissemination of the nanohole-based sensing platform to many researchers. While SPR sensors detect molecular interactions between analyte and target molecules, surface-enhanced Raman spectroscopy (SERS) can identify molecules by detecting their chemical structures. Among several SERS substrates, nanogap structures are known to generate substantial plasmonic electromagnetic fields, leading to a large SERS signal enhancement when a SERS-active molecule is positioned within the nanogap. It is not practical to use conventional fabrication methods, *e.g.* e-beam lithography, for wafer-scale fabrication of dense nanogap arrays with a sub-10-nm resolution. Therefore, we had to develop a new fabrication method utilizing an ultrathin conformal dielectric layer grown by ALD, is demonstrated for the production of sub-10-nm gaps with precise control of the gap's size, position, shape, and orientation. The EFs arising from these structures increase up to 10^9 as the gap size decreases to 5 nm. The capability of these nanostructured materials and SPR devices for biosensing applications is tremendous in terms of their sensing ability, high-throughput screening, cost, and design flexibility.

8.2 Future Research

8.2.1 Fabrication of sharp metallic tips

Sharp metallic tips have been used in tip-enhanced Raman spectroscopy (TERS),[189,190] plasmonic nanofocusing,[150] and high-resolution near-field optical imaging.[186,187] Previously, it was demonstrated that template stripping of metallic films deposited on anisotropically etched Si templates and cured with epoxy reveals pyramid and wedge arrays with ultra-smooth surface and sharp tips with 10 nm radii.[149] It has been demonstrated that larger field enhancement occurs at the tip with smaller tip size and shallower taper angle.[193] Also the sharper tips can improve the imaging resolution when it is used as the tip of scanning probe microscope (SPM) or near-field scanning optical microscope (NSOM).[186,187] While the anisotropic etching is useful to make the sharp pyramid tip, it is difficult to reduce the tip size further, and the angle of tip is always fixed by the

angle between (100) and (111) Si crystalline planes. However, thermal oxidation of the anisotropically etched Si substrate grows non-uniform thermal oxide layer as depicted in Figure 8.1. This is due to the intrinsic stress in the silicon dioxide layer on the V-shaped trenches caused by thermal oxidation.[212] As a result, sharper tips with shallow taper angles can be made by stripping thin films from the oxidized Si templates. (Figure 8.1)

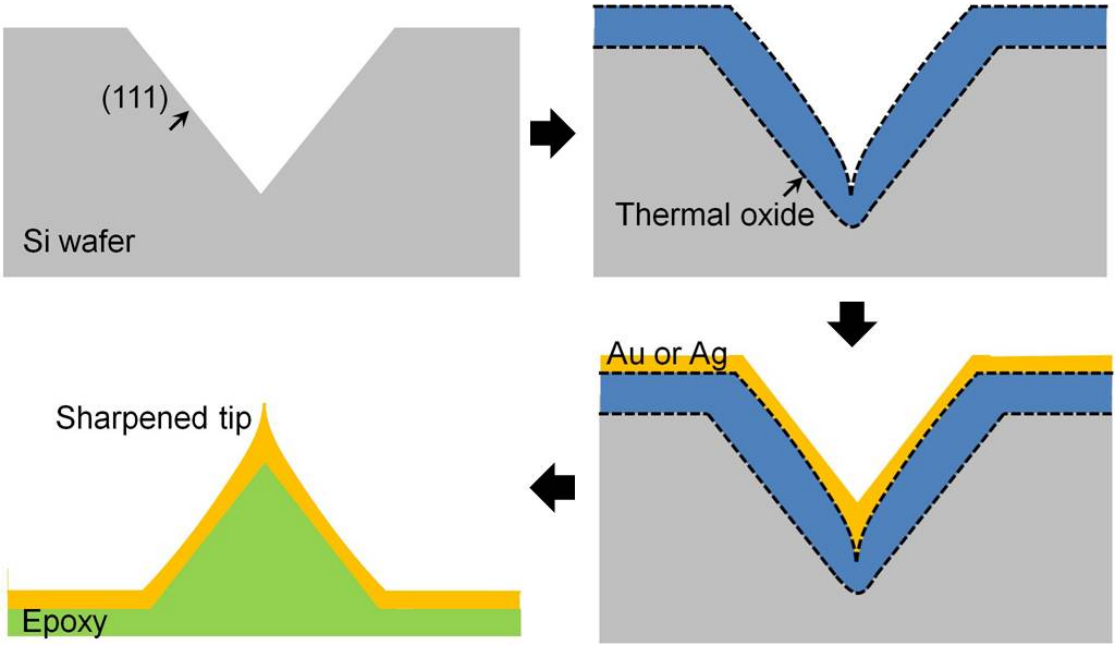

Figure 8.1: **Fabrication of sharp metal tips from oxidized Si template.** Thermal oxidation on anisotropically etched Si template forms a sharp corner at the bottom. Metal deposition and subsequent peel off of the mold with cured epoxy reveals an array of sharpened metallic tips.

Figure 8.2 shows SEM images of Au pyramids template stripped from oxidized Si templates thermally oxidized under different conditions. As the oxide layer grows thicker on the template, the template-stripped tips become sharper and narrower. Using this method, metallic tips with sub-10-nm radius and shallow angles have been successfully made. Combined with optical lithography, millions of metallic sharp tips can be made

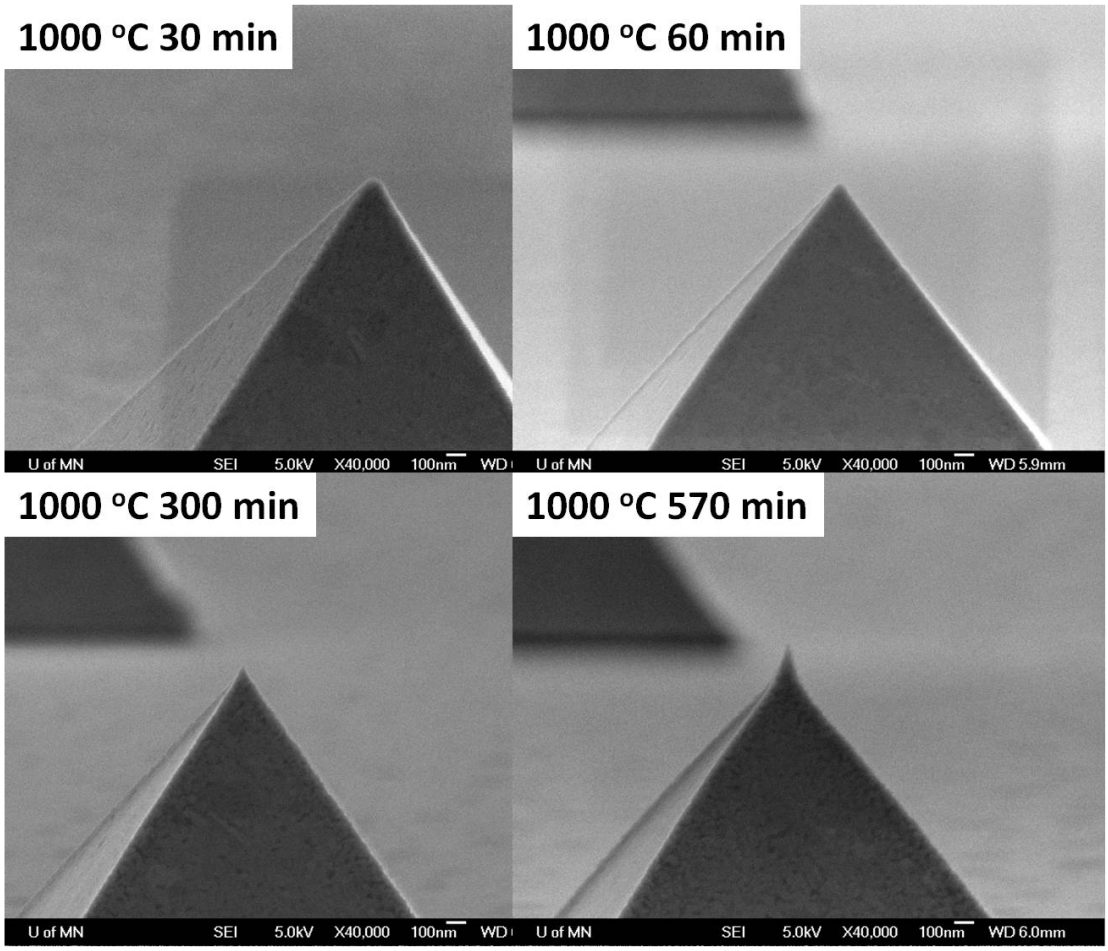

Figure 8.2: **The fabricated sharp metal tips from oxidized Si templates.** Sharpened Au tips are template stripped from the anisotropically etched Si template with different thermally grown oxides. The thermal oxidation conditions are indicated in the top-left corners.

from a single Si template, and the oxidized silicon template can be reused.

8.2.2 Stretchable plasmonics

Optical properties of plasmonic devices vary depending on their sizes, shapes, and materials. For periodically arranged grating structures, the resonance condition depends on the distance between patterns. For examples, in case of periodic nanohole arrays, the resonant peak position of transmitted light through the nanohole array can be tuned by adjusting the periodicity of nanohole array. While many stretchable electronic devices have been demonstrated for flexible and wearable circuits and devices,[213] efforts to develop stretchable plasmonic devices has started just recently. The fabrication of plasmonic nanostructures made on elastomeric substrates, such as polydimethylsiloxane (PDMS), allows reversible and active tuning of their optical properties.[214,215] Previous research focused on stretching the elastomer substrate on which meta-materials are made and actively tuning optical properties of meta-materials by adjusting the shape and distance between patterns. With template stripping, it is possible to transfer metallic patterns from a Si template to a flexible PDMS membrane as shown in Figure 8.3. Disconnected pyramids as well as continuous patterns of periodic nanohole arrays and bull's eye structures can be made on the stretchable substrate. Figure 8.4 shows changes of transmission spectra when a periodic Au nanohole array made on a PDMS membrane is stretched. Stretching increases the periodicity of the array along the direction of stretching, and thus tuning the frequency of the transmission peaks. When the incident light is polarized along the direction of stretching, it is seen that the transmission peak red-shifts as a result of increased periodicity. But when the light is polarized perpendicular to the stretching direction, the transmission peaks remain the same. This active tunability in the visible range would potentially benefit SPR imaging and SERS, wherein the resonance peak need to be placed close to the excitation laser wavelength to achieve the maximum sensitivity.

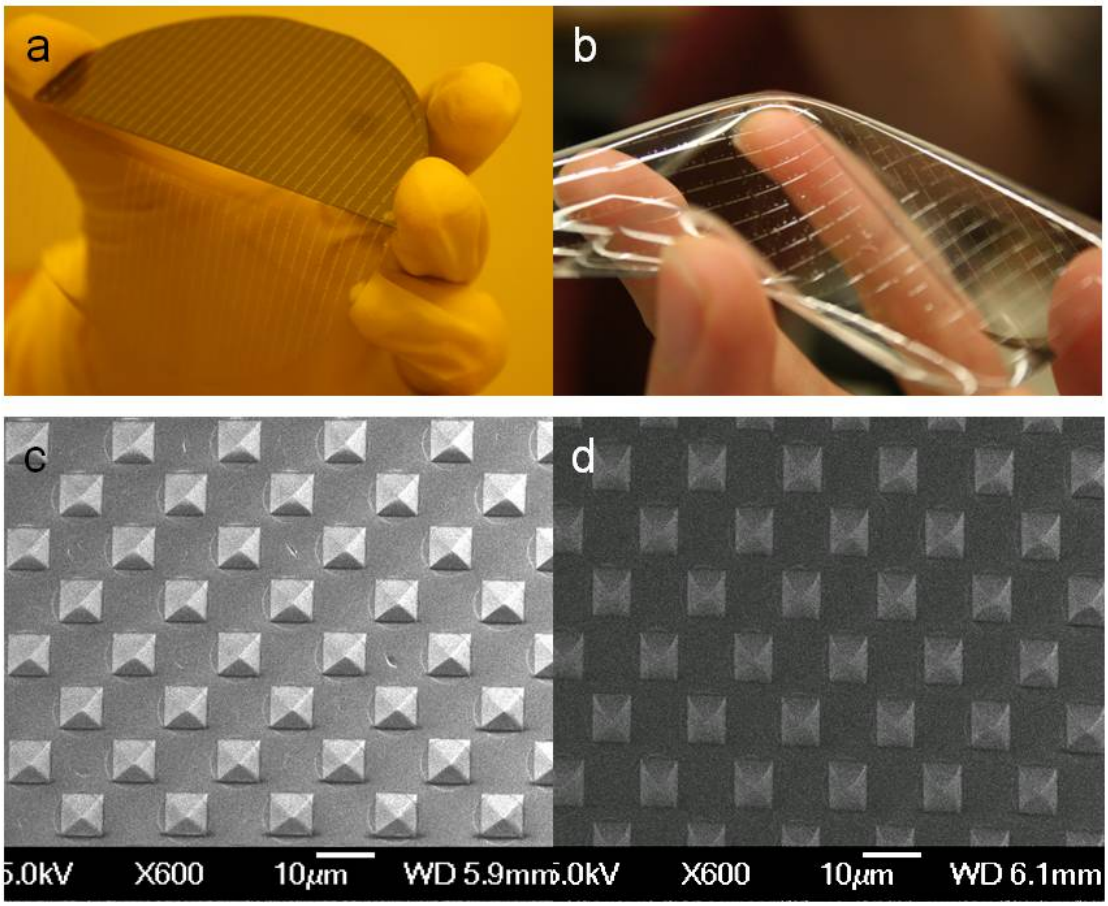

Figure 8.3: **Stretchable metallic patterns template stripped on a PDMS membrane.** Photographs of (a) Ag patterns peeled off of a Si template and transferred onto a PDMS membrane and (b) a flexible PDMS membrane with Ag patterns. SEM images of a metallic pyramid array (c) before and (d) after stretching along y-direction.

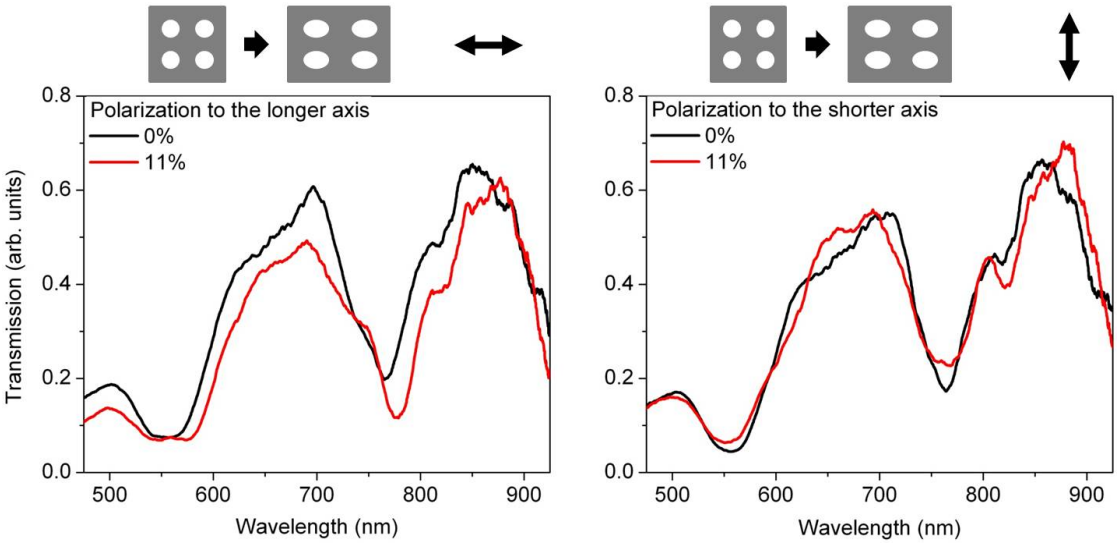

Figure 8.4: **Tuning of transmission spectra by stretching a periodic nanohole array.** Stretching the periodic nanohole array increases the periodicity along the stretch direction. As a result, when incident light is polarized the transmission peak red-shifts when the nanohole array is stretched (left), while the peaks stay when the incident light is polarized perpendicular to the direction of stretching.

References

[1] Oosterbroek, R. & Berg, A. *Lab-on-a-chip: miniaturized systems for (bio) chemical analysis and synthesis* (Elsevier Science, 2003).

[2] Lakowicz, J. & Masters, B. Principles of fluorescence spectroscopy. *Journal of Biomedical Optics* **13**, 029901 (2008).

[3] Lequin, R. Enzyme immunoassay (EIA)/enzyme-linked immunosorbent assay (ELISA). *Clinical Chemistry* **51**, 2415 (2005).

[4] Ritchie, R. Plasma losses by fast electrons in thin films. *Physical Review* **106**, 874 (1957).

[5] Homola, J., Yee, S. & Gauglitz, G. Surface plasmon resonance sensors: review. *Sensors and Actuators B: Chemical* **54**, 3–15 (1999).

[6] Cooper, M. Advances in membrane receptor screening and analysis. *Journal of Molecular Recognition* **17**, 286–315 (2004).

[7] Maynard, J. *et al.* Surface plasmon resonance for high-throughput ligand screening of membrane-bound proteins. *Biotechnology Journal* **4**, 1542–1558 (2009).

[8] Maier, S. *Plasmonics: fundamentals and applications* (Springer Verlag, 2007).

[9] Stern, E. & Ferrell, R. Surface plasma oscillations of a degenerate electron gas. *Physical Review* **120**, 130 (1960).

[10] Raether, H. *Surface plasmons* (Springer-Verlag Berlin, 1988).

[11] Johnson, P. & Christy, R. Optical constants of the noble metals. *Physical Review B* **6**, 4370–4379 (1972).

[12] Kretschmann, E. Die bestimmung optischer konstanten von metallen durch anregung von oberflächenplasmaschwingungen. *Zeitschrift für Physik A Hadrons and Nuclei* **241**, 313–324 (1971).

[13] Bethe, H. Theory of diffraction by small holes. *Physical Review* **66**, 163–182 (1944).

[14] Roberts, A. Electromagnetic theory of diffraction by a circular aperture in a thick, perfectly conducting screen. *Journal of the Optical Society of America A* **4**, 1970–1983 (1987).

[15] Ebbesen, T., Lezec, H., Ghaemi, H., Thio, T. & Wolff, P. Extraordinary optical transmission through sub-wavelength hole arrays. *Nature* **391**, 667–669 (1998).

[16] Genet, C. & Ebbesen, T. Light in tiny holes. *Nature* **445**, 39 (2007).

[17] Barnes, W., Murray, W., Dintinger, J., Devaux, E. & Ebbesen, T. Surface plasmon polaritons and their role in the enhanced transmission of light through periodic arrays of subwavelength holes in a metal film. *Physical Review Letters* **92**, 107401 (2004).

[18] Gao, H., Henzie, J. & Odom, T. Direct evidence for surface plasmon-mediated enhanced light transmission through metallic nanohole arrays. *Nano Letters* **6**, 2104–2108 (2006).

[19] Garcia-Vidal, F., Martin-Moreno, L., Ebbesen, T. & Kuipers, L. Light passing through subwavelength apertures. *Reviews of Modern Physics* **82**, 729 (2010).

[20] Ghaemi, H., Thio, T., Grupp, D., Ebbesen, T. & Lezec, H. Surface plasmons enhance optical transmission through subwavelength holes. *Physical Review B* **58**, 6779 (1998).

[21] Koerkamp, K., Enoch, S., Segerink, F., Van Hulst, N. & Kuipers, L. Strong influence of hole shape on extraordinary transmission through periodic arrays of subwavelength holes. *Physical Review Letters* **92**, 183901 (2004).

[22] Gordon, R. *et al.* Strong polarization in the optical transmission through elliptical nanohole arrays. *Physical Review Letters* **92**, 37401 (2004).

[23] Martin-Moreno, L. *et al.* Theory of extraordinary optical transmission through subwavelength hole arrays. *Physical Review Letters* **86**, 1114–1117 (2001).

[24] Chang, S., Gray, S. & Schatz, G. Surface plasmon generation and light transmission by isolated nanoholes and arrays of nanoholes in thin metal films. *Optics Express* **13**, 3150–3165 (2005).

[25] Langmuir, I. The constitution and fundamental properties of solids and liquids. part I. solids. *Journal of the American Chemical Society* **38**, 2221–2295 (1916).

[26] O'Shannessy, D. Determination of kinetic rate and equilibrium binding constants for macromolecular interactions: a critique of the surface plasmon resonance literature. *Current Opinion in Biotechnology* **5**, 65–71 (1994).

[27] Im, H., Lesuffleru, A., Lindquist, N. C., Lim, K. S. & Oh, S. H. Real-time, label-free plasmonic biosensing using periodic nanohole arrays. In *Frontiers in Nanophotonics and Plasmonics* (2007).

[28] Lesuffleur, A., Im, H., Lindquist, N. & Oh, S. Periodic nanohole arrays with shape-enhanced plasmon resonance as real-time biosensors. *Applied Physics Letters* **90**, 243110 (2007).

[29] Jung, L., Campbell, C., Chinowsky, T., Mimi, N. & Yee, S. Quantitative interpretation of the response of surface plasmon resonance sensors to adsorbed films. *Langmuir* **14**, 5636–5648 (1998).

[30] Vörös, J. The density and refractive index of adsorbing protein layers. *Biophysical Journal* **87**, 553–561 (2004).

[31] Stenberg, E., Persson, B., Roos, H. & Urbaniczky, C. Quantitative determination of surface concentration of protein with surface plasmon resonance using radiolabeled proteins. *Journal of Colloid and Interface Science* **143**, 513–526 (1991).

[32] *BIAtechnology handbook* (BIAcore AB, Uppsala, Sweden, 1998).

[33] Haes, A. & Van Duyne, R. A nanoscale optical biosensor: sensitivity and selectivity of an approach based on the localized surface plasmon resonance spectroscopy of triangular silver nanoparticles. *Journal of the American Chemical Society* **124**, 10596–10604 (2002).

[34] McFarland, A. & Van Duyne, R. Single silver nanoparticles as real-time optical sensors with zeptomole sensitivity. *Nano Letters* **3**, 1057–1062 (2003).

[35] Willets, K. & Van Duyne, R. Localized surface plasmon resonance spectroscopy and sensing. *Annual Review of Physical Chemistry* **58**, 267–297 (2007).

[36] Hall, W. *et al.* A conformation-and ion-sensitive plasmonic biosensor. *Nano Letters* (2011).

[37] Bingham, J., Anker, J., Kreno, L. & Van Duyne, R. Gas sensing with high-resolution localized surface plasmon resonance spectroscopy. *Journal of the American Chemical Society* (2010).

[38] Lindquist, N. An engineered metallic nanostructures for suface plasmon resonance biosensing. *Ph.D thesis* (2010).

[39] Brolo, A., Gordon, R., Leathem, B. & Kavanagh, K. Surface plasmon sensor based on the enhanced light transmission through arrays of nanoholes in gold films. *Langmuir* **20**, 4813–4815 (2004).

[40] Xia, Y. & Whitesides, G. Soft lithography. *Annual Review of Materials Science* **28**, 153–184 (1998).

[41] Green, N. Avidin and streptavidin. *Methods in Enzymology* **184**, 51 (1990).

[42] Lesuffleur, A., Kumar, L. & Gordon, R. Enhanced second harmonic generation from nanoscale double-hole arrays in a gold film. *Applied Physics Letters* **88**, 261104 (2006).

[43] Wang, Q. & Bohn, P. Surface composition gradients of immobilized cell signaling molecules. Epidermal growth factor on gold. *Thin Solid Films* **513**, 338–346 (2006).

[44] Im, H., Lesuffleur, A., Lindquist, N. & Oh, S. Plasmonic nanoholes in a multichannel microarray format for parallel kinetic assays and differential sensing. *Analytical Chemistry* **81**, 2854–2859 (2009).

[45] Lindquist, N., Lesuffleur, A., Im, H. & Oh, S. Sub-micron resolution surface plasmon resonance imaging enabled by nanohole arrays with surrounding Bragg mirrors for enhanced sensitivity and isolation. *Lab on a Chip* **9**, 382–387 (2009).

[46] Lesuffleur, A., Im, H., Lindquist, N., Lim, K. & Oh, S. Plasmonic nanohole arrays for real-time multiplex biosensing. In *Proceedings of SPIE*, vol. 7035, 703504 (2008).

[47] Lesuffleur, A., Im, H., Lindquist, N., Lim, K. & Oh, S. Laser-illuminated nanohole arrays for multiplex plasmonic microarray sensing. *Optics Express* **16**, 219–224 (2008).

[48] MacBeath, G. & Schreiber, S. Printing proteins as microarrays for high-throughput function determination. *Science* **289**, 1760 (2000).

[49] Ramachandran, N. *et al.* Self-assembling protein microarrays. *Science* **305**, 86 (2004).

[50] Chinowsky, T., Mactutis, T., Fu, E. & Yager, P. Optical and electronic design for a high-performance surface plasmon resonance imager. In *Proceedings of SPIE*, vol. 5261, 173 (2004).

[51] Brockman, J. & Fernández, S. Grating-coupled surface plasmon resonance for rapid, label-free, array-based sensing. *American Laboratory* **33**, 37–40 (2001).

[52] Tang, Y., Mernaugh, R. & Zeng, X. Nonregeneration protocol for surface plasmon resonance: study of high-affinity interaction with high-density biosensors. *Analytical Chemistry* **78**, 1841–1848 (2006).

[53] Im, H., Wittenberg, N., Lesuffleur, A., Lindquist, N. & Oh, S. Membrane protein biosensing with plasmonic nanopore arrays and pore-spanning lipid membranes. *Chemical Science* 688–696 (2010).

[54] Sackmann, E. Supported membranes: scientific and practical applications. *Science* **271**, 43 (1996).

[55] Brian, A. & McConnell, H. Allogeneic stimulation of cytotoxic T cells by supported planar membranes. *Proceedings of the National Academy of Sciences* **81**, 6159 (1984).

[56] Tamm, L. & McConnell, H. Supported phospholipid bilayers. *Biophysical Journal* **47**, 105–113 (1985).

[57] Cremer, P. & Boxer, S. Formation and spreading of lipid bilayers on planar glass supports. *The Journal of Physical Chemistry B* **103**, 2554–2559 (1999).

[58] Keller, C., Glasmästar, K., Zhdanov, V. & Kasemo, B. Formation of supported membranes from vesicles. *Physical Review Letters* **84**, 5443–5446 (2000).

[59] Castellana, E. & Cremer, P. Solid supported lipid bilayers: From biophysical studies to sensor design. *Surface Science Reports* **61**, 429–444 (2006).

[60] Salafsky, J., Groves, J. & Boxer, S. Architecture and function of membrane proteins in planar supported bilayers: a study with photosynthetic reaction centers. *Biochemistry* **35**, 14773–14781 (1996).

[61] Glazier, S. *et al.* Reconstitution of the pore-forming toxin α-hemolysin in phospholipid/18-octadecyl-1-thiahexa (ethylene oxide) and phospholipid/n-octadecanethiol supported bilayer membranes. *Langmuir* **16**, 10428–10435 (2000).

[62] Przybylo, M. *et al.* Lipid diffusion in giant unilamellar vesicles is more than 2 times faster than in supported phospholipid bilayers under identical conditions. *Langmuir* **22**, 9096–9099 (2006).

[63] Schoen, A. & Freire, E. Thermodynamics of intersubunit interactions in cholera toxin upon binding to the oligosaccharide portion of its cell surface receptor, ganglioside GM1. *Biochemistry* **28**, 5019–5024 (1989).

[64] Mueller, P., Rudin, D., Ti Tien, H. & Wescott, W. Reconstitution of cell membrane structure in vitro and its transformation into an excitable system. *Nature* **194**, 979–980 (1962).

[65] Römer, W. & Steinem, C. Impedance analysis and single-channel recordings on nano-black lipid membranes based on porous alumina. *Biophysical Journal* **86**, 955–965 (2004).

[66] Simon, A. *et al.* Formation and stability of a suspended biomimetic lipid bilayer on silicon submicrometer-sized pores. *Journal of Colloid and Interface Science* **308**, 337–343 (2007).

[67] White, R. *et al.* Single ion-channel recordings using glass nanopore membranes. *Journal of the American Chemical Society* **129**, 11766–11775 (2007).

[68] Hovis, J. & Boxer, S. Patterning and composition arrays of supported lipid bilayers by microcontact printing. *Langmuir* **17**, 3400–3405 (2001).

[69] Danelon, C., Perez, J., Santschi, C., Brugger, J. & Vogel, H. Cell membranes suspended across nanoaperture arrays. *Langmuir* **22**, 22–25 (2006).

[70] Mager, M. & Melosh, N. Lipid bilayer deposition and patterning via air bubble collapse. *Langmuir* **23**, 9369–9377 (2007).

[71] Anderson, T. *et al.* Formation of supported bilayers on silica substrates. *Langmuir* **25**, 6997–7005 (2009).

[72] Zhdanov, V., Dimitrievski, K. & Kasemo, B. Adsorption and spontaneous rupture of vesicles composed of two types of lipids. *Langmuir* **22**, 3477–3480 (2006).

[73] Im, H. *et al.* Template-stripped smooth ag nanohole arrays with silica shells for surface plasmon resonance biosensing. *ACS Nano* **5**, 6244–6253 (2011).

[74] Soumpasis, D. Theoretical analysis of fluorescence photobleaching recovery experiments. *Biophysical Journal* **41**, 95–97 (1983).

[75] Worsfold, O., Voelcker, N. & Nishiya, T. Biosensing using lipid bilayers suspended on porous silicon. *Langmuir* **22**, 7078–7083 (2006).

[76] Jönsson, P., Jonsson, M. & Höök, F. Sealing of submicrometer wells by a shear-driven lipid bilayer. *Nano Letters* **10**, 1900–1906 (2010).

[77] Steinem, C., Janshoff, A., Ulrich, W., Sieber, M. & Galla, H. Impedance analysis of supported lipid bilayer membranes: a scrutiny of different preparation techniques. *Biochimica et Biophysica Acta - Biomembranes* **1279**, 169–180 (1996).

[78] Wiegand, G., Arribas-Layton, N., Hillebrandt, H., Sackmann, E. & Wagner, P. Electrical properties of supported lipid bilayer membranes. *The Journal of Physical Chemistry B* **106**, 4245–4254 (2002).

[79] Steltenkamp, S. *et al.* Mechanical properties of pore-spanning lipid bilayers probed by atomic force microscopy. *Biophysical Journal* **91**, 217–226 (2006).

[80] Mey, I. *et al.* Local membrane mechanics of pore-spanning bilayers. *Journal of the American Chemical Society* **131**, 7031–7039 (2009).

[81] Korade, Z. & Kenworthy, A. Lipid rafts, cholesterol, and the brain. *Neuropharmacology* **55**, 1265–1273 (2008).

[82] Thomsen, W., Frazer, J. & Unett, D. Functional assays for screening GPCR targets. *Current Opinion in Biotechnology* **16**, 655–665 (2005).

[83] Compston, A. & Coles, A. Multiple sclerosis. *Lancet* **359**, 1221–1231 (2002).

[84] Noseworthy, J., Lucchinetti, C., Rodriguez, M. & Weinshenker, B. Medical progress: multiple sclerosis. *New England Journal of Medicine-Unbound Volume* **343**, 938–952 (2000).

[85] Asakura, K., Miller, D., Pease, L. & Rodriguez, M. Targeting of IgMκ antibodies to oligodendrocytes promotes CNS remyelination. *The Journal of Neuroscience* **18**, 7700 (1998).

[86] Warrington, A. *et al.* Human monoclonal antibodies reactive to oligodendrocytes promote remyelination in a model of multiple sclerosis. *Proceedings of the National Academy of Sciences* **97**, 6820 (2000).

[87] Bansal, R., Warrington, A., Gard, A., Ranscht, B. & Pfeiffer, S. Multiple and novel specificities of monoclonal antibodies O1, O4, and R-mAb used in the analysis of oligodendrocyte development. *Journal of Neuroscience Research* **24**, 548–557 (1989).

[88] Warrington, A., Bieber, A., Ciric, B., Pease, V., L.R. Van Keulen & Rodriguez, M. A recombinant human IgM promotes myelin repair after a single, very low dose. *Journal of Neuroscience Research* **85**, 967–976 (2007).

[89] Rodriguez, M., Warrington, A. & Pease, L. Human natural autoantibodies in the treatment of neurologic disease. *Neurology* **72**, 1269–1276 (2009).

[90] Vockenroth, I., Atanasova, P., Jenkins, A. & Köper, I. Incorporation of α-hemolysin in different tethered bilayer lipid membrane architectures. *Langmuir* **24**, 496–502 (2008).

[91] Han, X. *et al.* Nanopore arrays for stable and functional free-standing lipid bilayers. *Advanced Materials* **19**, 4466–4470 (2007).

[92] Hennesthal, C. & Steinem, C. Pore-spanning lipid bilayers visualized by scanning force microscopy. *Journal of the American Chemical Society* **122**, 8085–8086 (2000).

[93] White, R. *et al.* Ionic conductivity of the aqueous layer separating a lipid bilayer membrane and a glass support. *Langmuir* **22**, 10777–10783 (2006).

[94] Reimhult, E. & Kumar, K. Membrane biosensor platforms using nano-and microporous supports. *Trends in Biotechnology* **26**, 82–89 (2008).

[95] Liedberg, B., Nylander, C. & Lunstrom, I. Surface plasmon resonance for gas detection and biosensing. *Sensors and Actuators* **4**, 299–304 (1983).

[96] Smith, E., Thomas, W., Kiessling, L. & Robert, M. Surface plasmon resonance imaging studies of protein-carbohydrate interactions. *Journal of the American Chemical Society* **125**, 6140–6148 (2003).

[97] Shumaker-Parry, J., Aebersold, R. & Campbell, C. Parallel, quantitative measurement of protein binding to a 120-element double-stranded dna array in real time

using surface plasmon resonance microscopy. *Analytical Chemistry* **76**, 2071–2082 (2004).

[98] Ouellet, E. *et al.* Parallel microfluidic surface plasmon resonance imaging arrays. *Lab on a Chip* **10**, 581–588 (2010).

[99] Tanaka, M. *et al.* Native supported membranes on planar polymer supports and micro-particle supports. *Journal of Structural Biology* **168**, 137–142 (2009).

[100] Eftekhari, F. *et al.* Nanoholes as nanochannels: flow-through plasmonic sensing. *Analytical Chemistry* **81**, 4308–4311 (2009).

[101] Ferreira, J. *et al.* Attomolar protein detection using in-hole surface plasmon resonance. *Journal of the American Chemical Society* **131**, 436–437 (2009).

[102] Jonsson, M., Dahlin, A., Feuz, L., Petronis, S. & Ho o k, F. Locally functionalized short-range ordered nanoplasmonic pores for bioanalytical sensing. *Analytical Chemistry* **82**, 2087–2094 (2010).

[103] Yanik, A., Huang, M., Artar, A., Chang, T. & Altug, H. Integrated nanoplasmonic-nanofluidic biosensors with targeted delivery of analytes. *Applied Physics Letters* **96**, 021101 (2010).

[104] Hausmann, D., Becker, J., Wang, S. & Gordon, R. Rapid vapor deposition of highly conformal silica nanolaminates. *Science* **298**, 402 (2002).

[105] Im, H., Lindquist, N., Lesuffleur, A. & Oh, S. Atomic layer deposition of dielectric overlayers for enhancing the optical properties and chemical stability of plasmonic nanoholes. *ACS Nano* **4**, 947–954 (2010).

[106] Bhakdi, S. & Tranum-Jensen, J. Alpha-toxin of staphylococcus aureus. *Microbiology and Molecular Biology Reviews* **55**, 733 (1991).

[107] Bakás, L., Ostolaza, H. & Vaz, W. Reversible adsorption and nonreversible insertion of Escherichia coli alpha-hemolysin into lipid bilayers. *Biophysical Journal* **71**, 1869–1876 (1996).

[108] Ragle, B. & Bubeck Wardenburg, J. Anti-alpha-hemolysin monoclonal antibodies mediate protection against Staphylococcus aureus pneumonia. *Infection and Immunity* **77**, 2712 (2009).

[109] Gu, L. & Shim, J. Single molecule sensing by nanopores and nanopore devices. *Analyst* **135**, 441–451 (2009).

[110] Studer, A., Han, X., Winkler, F. & Tiefenauer, L. Formation of individual protein channels in lipid bilayers suspended in nanopores. *Colloids and Surfaces B: Biointerfaces* **73**, 325–331 (2009).

[111] Sexton, B., Feltis, B. & Davis, T. Characterisation of gold surface plasmon resonance sensor substrates. *Sensors and Actuators A: Physical* **141**, 471–475 (2008).

[112] Jiao, X., Goeckeritz, J., Blair, S. & Oldham, M. Localization of near-field resonances in bowtie antennae: influence of adhesion layers. *Plasmonics* **4**, 37–50 (2009).

[113] Aouani, H. *et al.* Crucial role of the adhesion layer on the plasmonic fluorescence enhancement. *ACS Nano* **3**, 2043–2048 (2009).

[114] Otte, M. *et al.* Improved biosensing capability with novel suspended nanodisks. *The Journal of Physical Chemistry C* **115**, 5344–5351 (2011).

[115] Haes, A. & Van Duyne, R. A unified view of propagating and localized surface plasmon resonance biosensors. *Analytical and Bioanalytical Chemistry* **379**, 920–930 (2004).

[116] Williams, S. *et al.* Use of the extraordinary infrared transmission of metallic subwavelength arrays to study the catalyzed reaction of methanol to formaldehyde on copper oxide. *The Journal of Physical Chemistry B* **108**, 11833–11837 (2004).

[117] Coe, J., Heer, J., Teeters-Kennedy, S., Tian, H. & Rodriguez, K. Extraordinary transmission of metal films with arrays of subwavelength holes. *Annual Review of Physical Chemistry* **59**, 179–202 (2008).

[118] Chan, G., Zhao, J., Schatz, G. & Duyne, R. Localized surface plasmon resonance spectroscopy of triangular aluminum nanoparticles. *The Journal of Physical Chemistry C* **112**, 13958–13963 (2008).

[119] Gao, H., Henzie, J., Lee, M. & Odom, T. Screening plasmonic materials using pyramidal gratings. *Proceedings of the National Academy of Sciences* **105**, 20146 (2008).

[120] Ferry, V., Sweatlock, L., Pacifici, D. & Atwater, H. Plasmonic nanostructure design for efficient light coupling into solar cells. *Nano Letters* **8**, 4391–4397 (2008).

[121] Lindquist, N., Luhman, W., Oh, S. & Holmes, R. Plasmonic nanocavity arrays for enhanced efficiency in organic photovoltaic cells. *Applied Physics Letters* **93**, 123308 (2008).

[122] Love, J., Estroff, L., Kriebel, J., Nuzzo, R. & Whitesides, G. Self-assembled monolayers of thiolates on metals as a form of nanotechnology. *Chemical Reviews* **105**, 1103–1170 (2005).

[123] George, S., Ott, A. & Klaus, J. Surface chemistry for atomic layer growth. *The Journal of Physical Chemistry* **100**, 13121–13131 (1996).

[124] Groner, M., Fabreguette, F., Elam, J. & George, S. Low-temperature Al_2O_3 atomic layer deposition. *Chemistry of Materials* **16**, 639–645 (2004).

[125] Groner, M., George, S., McLean, R. & Carcia, P. Gas diffusion barriers on polymers using Al_2O_3 atomic layer deposition. *Applied Physics Letters* **88**, 051907 (2006).

[126] Whitney, A. *et al.* Localized surface plasmon resonance nanosensor: A high-resolution distance-dependence study using atomic layer deposition. *The Journal of Physical Chemistry B* **109**, 20522–20528 (2005).

[127] Zhang, X., Zhao, J., Whitney, A., Elam, J. & Van Duyne, R. Ultrastable substrates for surface-enhanced Raman spectroscopy: Al_2O_3 overlayers fabricated by atomic layer deposition yield improved anthrax biomarker detection. *Journal of the American Chemical Society* **128**, 10304–10309 (2006).

[128] Przybilla, F., Degiron, A., Laluet, J., Genet, C. & Ebbesen, T. Optical transmission in perforated noble and transition metal films. *Journal of Optics A: Pure and Applied Optics* **8**, 458 (2006).

[129] Krishnan, A. *et al.* Evanescently coupled resonance in surface plasmon enhanced transmission. *Optics communications* **200**, 1–7 (2001).

[130] Rezania, A., Johnson, R., Lefkow, A. & Healy, K. Bioactivation of metal oxide surfaces. 1. surface characterization and cell response. *Langmuir* **15**, 6931–6939 (1999).

[131] Wu, X., Sun, Y. & Pelton, M. Recombination rates for single colloidal quantum dots near a smooth metal film. *Physical Chemistry Chemical Physics* **11**, 5867–5870 (2009).

[132] Yanik, A. *et al.* An optofluidic nanoplasmonic biosensor for direct detection of live viruses from biological media. *Nano Letters* (2010).

[133] Lezec, H. & Thio, T. Diffracted evanescent wave model for enhanced and suppressed optical transmission through subwavelength hole arrays. *Optics Express* **12**, 3629–3651 (2004).

[134] Kowalski, G. *et al.* Fast temperature sensing using changes in extraordinary optical transmission through an array of subwavelength apertures. *Optical Engineering* **48**, 104402 (2009).

[135] Hall, W. *et al.* A calcium-modulated plasmonic switch. *Journal of the American Chemical Society* **130**, 5836–5837 (2008).

[136] Nenninger, G., Piliarik, M. & Homola, J. Data analysis for optical sensors based on spectroscopy of surface plasmons. *Measurement Science and Technology* **13**, 2038 (2002).

[137] Dahlin, A., Tegenfeldt, J. & Höök, F. Improving the instrumental resolution of sensors based on localized surface plasmon resonance. *Analytical Chemistry* **78**, 4416–4423 (2006).

[138] Guo, L. Nanoimprint lithography: methods and material requirements. *Advanced Materials* **19**, 495–513 (2007).

[139] Xia, D., Ku, Z., Lee, S. & Brueck, S. Nanostructures and functional materials fabricated by interferometric lithography. *Advanced Materials* **23**, 147–179 (2011).

[140] Stewart, M. *et al.* Quantitative multispectral biosensing and 1D imaging using quasi-3D plasmonic crystals. *Proceedings of the National Academy of Sciences* **103**, 17143 (2006).

[141] Chen, J. *et al.* Gold nanohole arrays for biochemical sensing fabricated by soft UV nanoimprint lithography. *Microelectronic Engineering* **86**, 632–635 (2009).

[142] Yang, J. *et al.* Enhanced optical transmission mediated by localized plasmons in anisotropic, three-dimensional nanohole arrays. *Nano Letters* (2010).

[143] Tetz, K., Pang, L. & Fainman, Y. High-resolution surface plasmon resonance sensor based on linewidth-optimized nanohole array transmittance. *Optics Letters* **31**, 1528–1530 (2006).

[144] Henzie, J., Lee, M. & Odom, T. Multiscale patterning of plasmonic metamaterials. *Nature Nanotechnology* **2**, 549–554 (2007).

[145] Menezes, J., Ferreira, J., Santos, M., Cescato, L. & Brolo, A. Large-area fabrication of periodic arrays of nanoholes in metal films and their application in biosensing and plasmonic-enhanced photovoltaics. *Advanced Functional Materials* **20**, 3918–3924 (2010).

[146] Dahlin, A. *et al.* Localized surface plasmon resonance sensing of lipid-membrane-mediated biorecognition events. *Journal of the American Chemical Society* **127**, 5043–5048 (2005).

[147] Lee, S., Bantz, K., Lindquist, N., Oh, S. & Haynes, C. Self-assembled plasmonic nanohole arrays. *Langmuir* **25**, 13685–13693 (2009).

[148] Masson, J., Murray-Méthot, M. & Live, L. Nanohole arrays in chemical analysis: manufacturing methods and applications. *Analyst* **135**, 1483–1489 (2010).

[149] Nagpal, P., Lindquist, N., Oh, S. & Norris, D. Ultrasmooth patterned metals for plasmonics and metamaterials. *Science* **325**, 594 (2009).

[150] Lindquist, N., Nagpal, P., Lesuffleur, A., Norris, D. & Oh, S. Three-dimensional plasmonic nanofocusing. *Nano Letters* **10**, 1369–1373 (2010).

[151] Maynard, J. *et al.* Protection against anthrax toxin by recombinant antibody fragments correlates with antigen affinity. *Nature Biotechnology* **20**, 597–601 (2002).

[152] Murray-Me thot, M., Ratel, M. & Masson, J. Optical properties of Au, Ag, and bimetallic Au on Ag nanohole arrays. *The Journal of Physical Chemistry C* **114**, 8268–8275 (2010).

[153] Liu, H. *et al.* Enhanced surface plasmon resonance on a smooth silver film with a seed growth layer. *ACS Nano* **4**, 3139–3146 (2010).

[154] Guo, P. *et al.* Fluorescence enhancement by surface plasmon polaritons on metallic nanohole arrays. *The Journal of Physical Chemistry Letters* **1**, 315–318 (2009).

[155] Mager, M. & Melosh, N. Nanopore-spanning lipid bilayers for controlled chemical release. *Advanced Materials* **20**, 4423–4427 (2008).

[156] Yang, T., Jung, S., Mao, H. & Cremer, P. Fabrication of phospholipid bilayer-coated microchannels for on-chip immunoassays. *Analytical Chemistry* **73**, 165–169 (2001).

[157] Zielinski, O. *et al.* Detecting marine hazardous substances and organisms: sensors for pollutants, toxins, and pathogens. *Ocean Science* **5**, 329–349 (2009).

[158] Bantz, K. *et al.* Recent progress in SERS biosensing. *Physical Chemistry Chemical Physics* **13**, 11551–11567 (2011).

[159] Kneipp, J., Kneipp, H., Wittig, B. & Kneipp, K. Novel optical nanosensors for probing and imaging live cells. *Nanomedicine: Nanotechnology, Biology and Medicine* **6**, 214–226 (2010).

[160] He, L. *et al.* Detection of a foreign protein in milk using surface-enhanced raman spectroscopy coupled with antibody-modified silver dendrites. *Analytical Chemistry* **83**, 1510–1513 (2011).

[161] Yea, K. *et al.* Ultra-sensitive trace analysis of cyanide water pollutant in a PDMS microfluidic channel using surface-enhanced raman spectroscopy. *Analyst* **130**, 1009–1011 (2005).

[162] Im, H., Bantz, K., Lindquist, N., Haynes, C. & Oh, S. Vertically oriented sub-10-nm plasmonic nanogap arrays. *Nano Letters* **10**, 2231–2236 (2010).

[163] Raman, C. & Krishnan, K. A new type of secondary radiation. *Nature* **121**, 501–502 (1928).

[164] Haynes, C. & Van Duyne, R. *Encyclopedia of Physical Science and Technology.* 845–866 (Academic Press, 2001), third edition edn.

[165] Singh, R. CV raman and the discovery of the Raman effect. *Physics in Perspective* **4**, 399–420 (2002).

[166] Fleischmann, M., Hendra, P. & McQuillan, A. Raman spectra of pyridine adsorbed at a silver electrode. *Chemical Physics Letters* **26**, 163–166 (1974).

[167] Jeanmaire, D. & Van Duyne, R. Surface raman spectroelectrochemistry:: Part I. heterocyclic, aromatic, and aliphatic amines adsorbed on the anodized silver electrode. *Journal of Electroanalytical Chemistry and Interfacial Electrochemistry* **84**, 1–20 (1977).

[168] Albrecht, M. & Creighton, J. Anomalously intense Raman spectra of pyridine at a silver electrode. *Journal of the American Chemical Society* **99**, 5215–5217 (1977).

[169] McCreery, R. *Raman spectroscopy for chemical analysis*, vol. 157 (Wiley-Interscience, 2000).

[170] Kneipp, K. *et al.* Single molecule detection using surface-enhanced Raman scattering (sers). *Physical Review Letters* **78**, 1667–1670 (1997).

[171] Nie, S. & Emory, S. Probing single molecules and single nanoparticles by surface-enhanced Raman scattering. *Science* **275**, 1102 (1997).

[172] Jiang, J., Bosnick, K., Maillard, M. & Brus, L. Single molecule Raman spectroscopy at the junctions of large Ag nanocrystals. *The Journal of Physical Chemistry B* **107**, 9964–9972 (2003).

[173] McFarland, A., Young, M., Dieringer, J. & Van Duyne, R. Wavelength-scanned surface-enhanced Raman excitation spectroscopy. *The Journal of Physical Chemistry B* **109**, 11279–11285 (2005).

[174] Lyandres, O. *et al.* Real-time glucose sensing by surface-enhanced Raman spectroscopy in bovine plasma facilitated by a mixed decanethiol/mercaptohexanol partition layer. *Analytical Chemistry* **77**, 6134–6139 (2005).

[175] Zhang, X., Young, M., Lyandres, O. & Van Duyne, R. Rapid detection of an anthrax biomarker by surface-enhanced Raman spectroscopy. *Journal of the American Chemical Society* **127**, 4484–4489 (2005).

[176] Stuart, D. *et al.* In vivo glucose measurement by surface-enhanced Raman spectroscopy. *Analytical Chemistry* **78**, 7211–7215 (2006).

[177] Fang, Y., Seong, N. & Dlott, D. Measurement of the distribution of site enhancements in surface-enhanced Raman scattering. *Science* **321**, 388 (2008).

[178] Van Duyne, R., Hulteen, J. & Treichel, D. Atomic force microscopy and surface-enhanced Raman spectroscopy. I. ag island films and ag film over polymer nanosphere surfaces supported on glass. *The Journal of Chemical Physics* **99**, 2101 (1993).

[179] Bantz, K. & Haynes, C. Surface-enhanced raman scattering detection and discrimination of polychlorinated biphenyls. *Vibrational Spectroscopy* **50**, 29–35 (2009).

[180] Haynes, C. & Van Duyne, R. Nanosphere lithography: a versatile nanofabrication tool for studies of size-dependent nanoparticle optics. *The Journal of Physical Chemistry B* **105**, 5599–5611 (2001).

[181] Hao, E. & Schatz, G. Electromagnetic fields around silver nanoparticles and dimers. *The Journal of Chemical Physics* **120**, 357 (2004).

[182] Haynes, C., McFarland, A., Smith, M., Hulteen, J. & Van Duyne, R. Angle-resolved nanosphere lithography: Manipulation of nanoparticle size, shape, and interparticle spacing. *The Journal of Physical Chemistry B* **106**, 1898–1902 (2002).

[183] Haynes, C. *et al.* Nanoparticle optics: the importance of radiative dipole coupling in two-dimensional nanoparticle arrays. *The Journal of Physical Chemistry B* **107**, 7337–7342 (2003).

[184] Lal, S., Link, S. & Halas, N. Nano-optics from sensing to waveguiding. *Nature Photonics* **1**, 641–648 (2007).

[185] Ropers, C. *et al.* Light confinement at ultrasharp metallic tips. *Japanese Journal of Applied Physics* **47**, 6051–6054 (2008).

[186] Kawata, S., Inouye, Y. & Verma, P. Plasmonics for near-field nano-imaging and superlensing. *Nature Photonics* **3**, 388–394 (2009).

[187] Novotny, L. & Stranick, S. Near-field optical microscopy and spectroscopy with pointed probes*. *Annual Review of Physsical Chemistry* **57**, 303–331 (2006).

[188] Leonhardt, K. *et al.* Atomic force microscopy-scanning electrochemical microscopy: Influence of tip geometry and insulation defects on diffusion controlled currents at conical electrodes. *Analytical Chemistry* (2011).

[189] Pettinger, B. Tip-enhanced Raman spectroscopy (ters). *Surface-Enhanced Raman Scattering* 217–240 (2006).

[190] You, Y. *et al.* Tip-enhanced Raman spectroscopy using single-crystalline ag nanowire as tip. *Journal of Raman Spectroscopy* **41**, 1156–1162 (2010).

[191] Weber-Bargioni, A. *et al.* Hyperspectral nanoscale imaging on dielectric substrates with coaxial optical antenna scan probes. *Nano Letters* (2011).

[192] Scaffidi, J., Gregas, M., Seewaldt, V. & Vo-Dinh, T. SERS-based plasmonic nanobiosensing in single living cells. *Analytical and Bioanalytical Chemistry* **393**, 1135–1141 (2009).

[193] Roth, R. *et al.* Resonant-plasmon field enhancement from asymmetrically illuminated conical metallic-probe tips. *Optics Express* **14**, 2921–2931 (2006).

[194] Zhang, W. *et al.* Nanoscale roughness on metal surfaces can increase tip-enhanced Raman scattering by an order of magnitude. *Nano Letters* **7**, 1401–1405 (2007).

[195] Steidtner, J. & Pettinger, B. Tip-enhanced Raman spectroscopy and microscopy on single dye molecules with 15 nm resolution. *Physical Review Letters* **100**, 236101 (2008).

[196] Im, H., Huang, X., Gu, B. & Choi, Y. A dielectric-modulated field-effect transistor for biosensing. *Nature Nanotechnology* **2**, 430–434 (2007).

[197] Miyazaki, H. & Kurokawa, Y. Squeezing visible light waves into a 3-nm-thick and 55-nm-long plasmon cavity. *Physical Review Letters* **96**, 97401 (2006).

[198] Zhang, H., Chung, S. & Mirkin, C. Fabrication of sub-50-nm solid-state nanostructures on the basis of dip-pen nanolithography. *Nano Letters* **3**, 43–45 (2003).

[199] Salaita, K., Wang, Y. & Mirkin, C. Applications of dip-pen nanolithography. *Nature Nanotechnology* **2**, 145–155 (2007).

[200] Wang, H., Levin, C. & Halas, N. Nanosphere arrays with controlled sub-10-nm gaps as surface-enhanced raman spectroscopy substrates. *Journal of the American Chemical Society* **127**, 14992–14993 (2005).

[201] Lu, Y., Liu, G., Kim, J., Mejia, Y. & Lee, L. Nanophotonic crescent moon structures with sharp edge for ultrasensitive biomolecular detection by local electromagnetic field enhancement effect. *Nano Letters* **5**, 119–124 (2005).

[202] Hatzor, A. & Weiss, P. Molecular rulers for scaling down nanostructures. *Science* **291**, 1019 (2001).

[203] Reed, M., Zhou, C., Muller, C., Burgin, T. & Tour, J. Conductance of a molecular junction. *Science* **278**, 252 (1997).

[204] Ward, D. *et al.* Electromigrated nanoscale gaps for surface-enhanced raman spectroscopy. *Nano Letters* **7**, 1396–1400 (2007).

[205] Gopinath, A. *et al.* Plasmonic nanogalaxies: multiscale aperiodic arrays for surface-enhanced raman sensing. *Nano letters* **9**, 3922–3929 (2009).

[206] Bozhevolnyi, S., Volkov, V., Devaux, E., Laluet, J. & Ebbesen, T. Channel plasmon subwavelength waveguide components including interferometers and ring resonators. *Nature* **440**, 508–511 (2006).

[207] Dick, L., McFarland, A., Haynes, C. & Van Duyne, R. Metal film over nanosphere (MFON) electrodes for surface-enhanced raman spectroscopy (SERS): Improvements in surface nanostructure stability and suppression of irreversible loss. *The Journal of Physical Chemistry B* **106**, 853–860 (2002).

[208] Whelan, C., Smyth, M. & Barnes, C. HREELS, XPS, and electrochemical study of benzenethiol adsorption on au (111). *Langmuir* **15**, 116–126 (1999).

[209] Wan, L., Terashima, M., Noda, H. & Osawa, M. Molecular orientation and ordered structure of benzenethiol adsorbed on gold (111). *The Journal of Physical Chemistry B* **104**, 3563–3569 (2000).

[210] Xu, H. & Käll, M. Polarization-dependent surface-enhanced Raman spectroscopy of isolated silver nanoaggregates. *ChemPhysChem* **4**, 1001–1005 (2003).

[211] Baik, J., Lee, S. & Moskovits, M. Polarized surface-enhanced raman spectroscopy from molecules adsorbed in nano-gaps produced by electromigration in silver nanowires. *Nano Letters* **9**, 672–676 (2009).

[212] Vollkopf, A., Rudow, O., Müller-Wiegand, M., Georgiev, G. & Oesterschulze, E. Influence of the oxidation temperature on the fabrication process of silicon dioxide aperture tips. *Applied Physics A: Materials Science & Processing* **76**, 923–926 (2003).

[213] Rogers, J., Someya, T. & Huang, Y. Materials and mechanics for stretchable electronics. *Science* **327**, 1603 (2010).

[214] Aydin, K., Pryce, I. & Atwater, H. Symmetry breaking and strong coupling in planar optical metamaterials. *Optics Express* **18**, 13407–13417 (2010).

[215] Pryce, I., Aydin, K., Kelaita, Y., Briggs, R. & Atwater, H. Highly strained compliant optical metamaterials with large frequency tunability. *Nano Letters* (2010).

[216] Leskelä, M. & Ritala, M. Atomic layer deposition chemistry: recent developments and future challenges. *Angewandte Chemie International Edition* **42**, 5548–5554 (2003).

[217] Puurunen, R. Surface chemistry of atomic layer deposition: A case study for the trimethylaluminum/water process. *Journal of Applied Physics* **97**, 121301 (2005).

[218] George, S. Atomic layer deposition: An overview. *Chemical Reviews* **110**, 111–131 (2010).

[219] Lim, B., Rahtu, A. & Gordon, R. Atomic layer deposition of transition metals. *Nature Materials* **2**, 749–754 (2003).

Appendix A

Atomic Layer Deposition

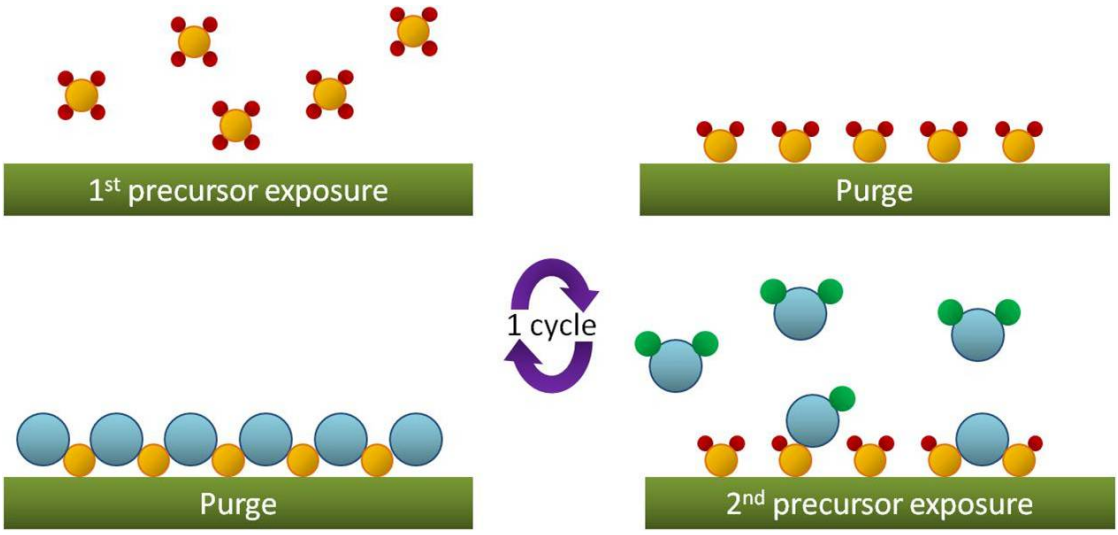

Figure A.1: **Atomic Layer Deposition (ALD).** In a typical ALD reaction for depositing a binary compound film, the two precursors are sequentially introduced into a reaction chamber with a purging step in between the first and second precursors. Each growth step self-saturates, thus the deposited film thickness after each cycle is highly reproducible. Therefore, the desired thickness can be controlled precisely by the number of deposition cycles.

Atomic layer deposition (ALD) is a variant of chemical vapor deposition (CVD) technique capable of angstrom-level resolution, layer-by-layer growth of compound films.[216–218] ALD can deposit these ultra-thin films in a conformal manner over a wide range of materials and high-aspect-ratio topography. In a typical ALD reaction for depositing a binary compound film, the precursors "A" and "B" are sequentially introduced into a reaction chamber with a purging step in between: A/purge/B/purge/A/purge, etc until the desired thickness is reached as depicted in Figure A.1. An archetypical ALD process is the deposition of Al_2O_3 from trimethylaluminum (TMA) and H_2O, which consists of four steps:[217] (1) inject the first precursor (TMA) until its binding sites on the reaction surface are saturated; (2) purge the chamber with inert gas and remove unbound precursor; (3) inject the second precursor (H_2O) and form a monolayer of hydroxyl (OH) groups on the surface; and (4) purge. Each growth step self-saturates when the surface binding sites are occupied, thus the deposited film thickness after each cycle is highly reproducible. The total film thickness can be tuned in a step-wise manner by the number of atomically thick ALD cycles. Importantly, the film thickness can be precisely controlled over a large area, regardless of the underlying topography, because the self-saturating growth mechanism will even out non-uniform local growth rates because the film growth rate is less affected by the homogeneity of precursor flux. Additionally, the chemical reactions in ALD occur only on surfaces, and not in the gas phase, because the precursors are injected alternately and do not mix with each other. This scheme prevents unwanted particle generation caused by gas-phase reactions, and also allows the use of highly reactive precursors such as TMA, which are difficult to use with CVD. By utilizing these highly reactive precursors, many ALD reactions can be performed at temperatures around 50–250 °C, well below typical CVD temperatures. Thus ALD is an ideal method to deposit dense and conformal films on polymer, plastic, or even biological samples that cannot withstand high temperatures. One drawback of ALD - although it may also be considered one of its key benefits - is its slow deposition rate, which is often an order of magnitude lower than the CVD rate. Usually a fraction

of a monolayer is grown in each cycle because of steric hindrance of precursor molecules on the surface. Fortunately, many applications in microelectronics, and now in plasmonics, require ultra-thin (*e.g.* <10 nm) films, thus throughput is not a major problem. Common materials that can be deposited via ALD are Al_2O_3, HfO_2, ZrO_2, TiO_2, SiO_2, and some metals such as Cu and Ag.[218,219] In the dissertation, ALD has been used for layer-by-layer optical characterization (Chapter 6.1.2), improving chemical stability of Ag surface (Chapter 6.1.3, facilitating lipid membrane formation (Chapter 5), and sub-10-nm nanogap fabrication (Chapter 7.3)

Appendix B

Fabrication Methods and Recipes

This section describes the detailed information of fabrication process and experimental procedures for research works presented in the dissertation. Fabrication of SPR devices, microfluidic flow cells, and other nanostructures have been done in the Nanofabrication Center (NFC) in the University of Minnesota. Scanning electron microscope (SEM) imaging and confocal Raman measurements have been done in the Characterization Facility in the University of Minnesota. Optical measurements and real-time biosensing have been performed using a standard upright microscope in Prof. Sang-Hyun Oh's research lab.

B.1 Fabrication Methods

In this section, fabrication processes for following devices are described:

1. Surface cleaning and metal deposition
2. Nanohole arrays with focused ion beam (FIB)
3. Nanohole arrays in free-standing Au/Si_3N_4 films
4. Nanohole arrays with nanoimprint lithography

5. Nanohole arrays using template stripping

6. PDMS microfluidic flow cells.

7. Nanogap arrays using atomic layer deposition (ALD)

B.1.1 Surface cleaning and metal deposition

Plasmonic nanohole arrays made in Au or Ag film deposited on standard glass slides. The metal-deposited glass slides are prepared by following procedures:

1) Sonication of glass slides at 50 W with acetone, methanol, and isopropyl alcohol (IPA) at least 5 min for each solution.

2) Rinse the glass slides with deionized (DI) water for at least 3 times.

3) Dry the glass slides first using a nitrogen gas and then a hotplate above 100 °C until the surface is perfectly dried.

4) Deposit metals using electron-beam evaporator (CHA or Temescal). In case of using Au, a 5 nm-thick Cr or Ti adhesion layer is deposited before Au deposition. The deposition rates for the adhesion layer and Au (or Ag) are around 0.5 and 1-2 Å/sec, respectively.

5) For a patterned metal layer, metal films are deposited on a photoresist layer is patterned through a standard optical lithography process. When the photoresist is removed by acetone or resist remover, the metal deposited on the resist patterns are lifted off of the substrate and the patterned metal layer is achieved.

B.1.2 Fabrication of nanohole arrays with focused ion beam (FIB)

The nanohole arrays presented in Chapter 3 and 4 are made using a focused ion beam (FIB) milling with the Au-coated glass slides. The beam voltage is set to 30 keV. The beam current varies depending on size of patterns and materials. For instance, nanohole

arrays with 16 × 16 or fewer numbers of holes are usually milled with the beam current of 30 pA and bigger arrays *e.g.* 32 × 32 nanoholes are milled with the current of 100 pA. The milling time needs to be adjusted based on ion-beam current profile shown in FIB software.

B.1.3 Fabrication of nanohole arrays in free-standing Au/Si_3N_4 films

1) Deposit a 100 nm-thick low-stressed Si_3N_4 layer using low-pressure chemical vapor deposition (LPCVD).

2) Spin-coat a front-side of wafer with a S1818 photoresist at 3000 rpm for 30 sec and bake it at 105 °C for 1 min on a hotplate. This is to protect the smooth top-surface from following steps.

3) Repeat the step 2 on a back-side of wafer with a S1813 photoresist.

4) Exposure the resist through a chrome-on-soda-lime-glass photomask for 6 sec using a MA6 or MABA6 aligner in a hard contact mode.

5) Bake the exposed resist for 105 °C for 1 min and develop the resist for 30 sec using a 351 developer 5 times diluted with DI water.

6) Remove residual resist for 30 sec with 100 sccm of O2 at 100 W (**O2CLEAN** recipe in STS etcher) and etch nitride for 2 min and 30 sec with 40 sccm of CF_4 and 4 sccm of O_2 at 50 W (**NIT1** recipe in STS etcher).

7) Strip all photoresist using acetone and a piranha solution (1:1 mixture of sulfuric acid and hydrogen peroxide) for 10 min each.

8) Etch Si in a KOH solution to form a free-standing Si_3N_4 film. The etch rate varies depending on the concentration of KOH solution and operation temperature. Be careful not to break the free-standing film during the following process.

9) Rinse the sample with DI water at least 3 times and dry the surface carefully with low-pressure of N_2 gas. Washing the surface with IPA makes easy to dry the surface. Put the sample on a hotplate above 100 °C until the surface is perfectly dried.

10) Deposit a metal film on the front-side of wafer as described in the step 4 of section B.1.1.

11) Pattern nanohole arrays using FIB from back-side of wafer. In this case, the beam current should be set to 500 pA. The conductive Cu tapes should be attached on both front and back sides of Si wafer.

12) Deposit a silica layer using atomic layer deposition (ALD) at 250 °C. The deposition rate is about 1.2 Å/cycle. (Use **slow-test1** recipe in ALD)

B.1.4 Fabrication of nanohole arrays with nanoimprint lithography

1) Deposit a 30 nm-thick Al_2O_3 layer on Au-coated slides using atomic layer deposition (ALD) at 250 °C ($\sim$ 270 cycles)

2) Spin-coat the surface with a thermal nanoimprint resist (NXR-1025 from Nanonex Corp., NJ) at 3500 rpm for 1 min and bake the resist at 150 °C for 1 min.

3) Prepare a Si imprint stamp with a 2-dimensional array of circular posts with 210 nm in diameter, 350 nm in depth, and 500 nm in periodicity and coat the Si surface with (heptadecafluoro-1,1,2,2-tetrahydrodecyl)trichlorosilane (obtained from Gelest Inc., PA) using a vacuum dessicator for 1 hr.

4) Imprint the Si stamp onto the resist with a pressure of 300 psi for 2 min at 130 °C

5) Remove residuar resist for 30 sec with 2 sccm of O_2 at 50 W (**O2NIL50W** recipe in STS etcher).

6) Etch the alumina layer with the imprint resist as a mask for 3 min with 5 sccm of Ar, 15 sccm of BCl_3 at 20 W DC power and 200 W ICP power (Run **Ti** recipe in Trion 2 twice) and wash the sample in DI water at least 1 min to remove chlorine residues.

7) Remove the imprint resist by dipping in acetone for 30 min and subsequent oxygen plasma cleaning for 15-30 min with 100 sccm of O_2 at 100 W (**O2CLEAN** recipe in STS etcher)

8) Etch the underlying Au film with the patterned alumina layer as a mask using an ion mill. Adjust the cathode current to have the beam current of 95 mA with the beam voltage of 300 W. Set to angle to be 0 deg. With the condition, the etch rates for Au and Ag are about 160 and 200 Å/min, respectively.

9) Check transmission spectrum and etch it longer if the transmission intensity is too low (¡ 1000 counts with 10 msec integration time). Confirm the hole size ($\sim$ 200 nm) with SEM.

10) Clean the surface with a piranha solution for 15 min.

11) Remove the alumina mask using the same condition as step 6, but for 1 min 30 sec. (Run **Ti** recipe in Trion only once)

12) Dip the nanohole sample in a buffered oxide etchant for less than 5 sec to remove residual alumina.

13) If necessary, deposit a silica layer using atomic layer deposition (ALD) at 250 °C . The deposition rate is about 12 Å/cycle. (Use **slow-test1** recipe in ALD)

B.1.5 Fabrication of nanohole arrays using template stripping

1) Prepare Si wafers with 100-nm-thick thermal oxide using wet oxidation at 1100 °C for 11 min.

2) Follow steps 2 $\sim$ 5 in the section B.1.4.

3) Etch the thermal oxide layer with the imprint resist as a mask for 4 min with 25 sccm of CF_4 and 50 sccm of Ar gases at 150 W (**PJSOXIDE** recipe in STS etcher)

4) Follow step 7 in the section B.1.4. Oxygen plasma cleaning with shorter time ($\sim$ 3 min) is also acceptable.

5) tch Si with the patterned oxide layer as a mask for 3 min using Si deep trench etcher (**CNF-14mT** recipe in DRIE)

6) Clean the patterned Si template with oxygen plasma for 15–30 min (**O2CLEAN** recipe in STS etcher)

7) Remove the oxide layer using a BOE solution until the surface turns into hydrophobic.

8) Clean the template using a piranha solution for 5 min. It will grow a thin chemical oxide layer on the substrate and allow peeling off metals of the Si template.

9) Rinse the Si template with DI water at least 3 times. Dry the template first using a nitrogen gas and then a hotplate above 100 °C until the surface is perfectly dried.

10) Deposit metals using the Temescal e-beam evaporator without any adhesion layer. It is crucial to reduce the metal deposition on the sidewalls, especially in order to obtain optically thick (¿ 100 nm) films, requiring the alignment of the metal evaporation source normal to the sample surface. To obtain smooth metal surface after template stripping, the deposition rate should be very slow (¡ 0.1 Å/sec) for first 10-20 nm of metal film.

11) Coat the metal with UV-curable optical epoxy (NOA 61, Norland products Inc., NJ) and cover it with a glass slide. It is crucial to use minimal amount of optical epoxy to obtain nanoholes with clean edges.

12) Cure the epoxy under UV light for 30 min and leave on a hotplate at 50 °C for several hours.

13) Peel off the metal of the Si template.

14) If necessary, the template-stripped metal can be covered by a thin silica layer using ALD at 100 °C. The deposition rate is around 16 Å/cycle. (Use **slow-test1** recipe in ALD)

15) Clean the Si template by removing remaining metals with wet etchants.

B.1.6 Fabrication of PDMS microfluidic flow cells

1) Remove a native oxide layer on a Si wafer by dipping the wafer in a BOE solution for a few seconds.

2) Make desired patterns using a SU-8 resist on the wafer. The type and spin-coating parameters should be adjusted based on the desired thickness of SU-8 mold. For instance, a SU-8 50 resist is used to make patterns with the height of around 50 $\sim$ 100 μm. For 50 μm-thick patterns,

   (i) spin coat a SU-8 50 resist at 1300 rpm for 30 sec.

   (ii) bake the resist at 65 °C for 10 min and then 95 °C for 40 min.

   (iii) expose the resist under UV light through a photomask for 50 sec.

   (iv) bake the resist at 65 °C for 1 min and then 95 °C for 5 min.

   (v) develop the resist for 10 min using a SU-8 developer.

   For 100 μm-thick patterns,

(i) spin coat a SU-8 50 resist at 2000 rpm for 30 sec.

(ii) bake the resist at 65 °C for 6 min and then 95 °C for 20 min.

(iii) expose the resist under UV light through a photomask for 30 sec.

(iv) bake the resist at 65 °C for 1 min and then 95 °C for 5 min.

(v) develop the resist for 6 min using a SU-8 developer.

3) Remove residual resist for 30 sec with 100 sccm of O_2 at 100 W (**O2CLEAN** recipe in STS etcher)

4) Coat the SU-8 mold wafer with (heptadecafluoro-1,1,2,2-tetrahydrodecyl) trichlorosilane (obtained from Gelest Inc., PA) using a vacuum dessicator for 1 hr to prevent stiction of PDMS on the Si surface.

5) Mix 30 g of PDMS with 3 g of curing agent and remove bubbles using a vacuum dessicator.

6) Pour the degassed PDMS mixture onto the SU-8 mold placed in an alumina foil basket.

7) Cure the PDMS at 60 °C for overnight. Curing at higher temperature will reduce the curing time.

8) Cut PDMS using a razor blade, punch inlets and outlets, and clean the surface with acetone, methanol, IPA, and water.

B.1.7 Fabrication of nanogap arrays using ALD

1) Deposit Au or Ag with a desired thickness with a 30 nm-thick Ti masking layer on a Si wafer with 100 – 300 nm-thick thermal oxide.

2) Make desired resist patterns through optical lithography For a positive-tone photoresist,

(i) Spin coat a SPR 220 7.0 resist at 500 rpm for 5 sec and 4000 rpm for 30 sec.

(ii) Bake the resist at 115 °C for 2 min.

(iii) Expose the resist under UV light through a photomask for 35 sec (12 mJ/cm^2 sec × 35 sec = 420 mJ/cm^2). Use a low-vacuum mode for patterns smaller than 10 μm.

(iv) Wait at least a half hour.

(v) Bake the exposed resist at 115 °C for 2 min.

(vi) Develop the resist using a MF 26A developer for 100 sec.

For a negative-tone photoresist,

(i) Spin coat a NR7-1500PY resist at 3000 rpm for 30 sec.

(ii) Bake the resist at 150 °C for 1 min 30 sec.

(iii) Expose the resist under UV light through a photomask for 14 sec.

(iv) Bake the exposed resist at 100 °C for 1 min 30 sec.

(v) Develop the resist using a MF 26A developer for 100 sec.

3) Remove residual resist for 30 sec with 100 sccm of O_2 at 100 W (**O2CLEAN** recipe in STS etcher)

4) Etch the Ti layer with the photoresist layer as a mask for 2 min with 18 sccm of Ar, 15 sccm of CF_4, and 15 sccm of Cl_2 at 65 W (Use Trion 2). After the etching process, wash the sample in DI water for at least 1 min.

5) Strip the photoresist using acetone.

6) Follow step 8 in the section B.1.4 to pattern metals.

7) Remove the Ti layer using a BOE solution

8) Deposit a thin alumina sacrificial layer with a desired thickness using ALD. The deposition temperatures and rates are 250 °C and 1.1 Å/cycle for Au patterns (**Al2O3_dep** recipe in ALD) and 50 °C and 1.8 Å/cycle for Ag patterns (**Al2O3_50deg** recipe in ALD).

9) Deposit a 200 nm-thick Ag film on the alumina-coated patterns.

10) Repeat the step 6 to anisotropically etch the Ag film.

11) Partially remove the alumina using a BOE solution. The etching time should vary depending on the thickness of alumina layer. For instance, it is etched for 16 sec with agitation followed by additional 5 sec etching without agitation for a 10 nm-thick alumina layer.

12) Rinse the sample with DI water for at least 15 min.

Appendix C

Common Acronyms

Table C.1: A listing of the common acronyms used throughout the dissertation.

Acronym	Meaning
α-HL	α-hemolysin
AFM	Atomic Force Microscopy
AgFON	Ag Film on Nanospheres
ALD	Atomic Layer Deposition
APTES	Aminopropyltriethoxysilane
biotin-PE	biotinylated-Phosphatidylethanolamine
BLM	Black Lipid Membrane
BSA	Bovine Serum Albumin
BOE	Buffered Oxide Etchant
BZT	Benzenethiol
CVD	Chemical Vapor Deposition
DOPC	1,2-dioleoyl-sn-glycero-3-phosphocholine

Continued on next page

Table C.1 – continued from previous page

Acronym	Meaning
DPPC	1,2-dipalmitoyl-sn-glycero-3-phosphocholine
EBL	Electron Beam Lithography
EDC	1-ethyl-3-(3-dimethylaminopropyl) carbodiimide)
EF	Enhancement Factor
Egg PC	L-α-phosphatidylcholine
EIS	electrochemical impedance spectroscopy
ELISA	Enzyme-Linked Immonusorbent Assays
EOT	Extraordinary Optical Transmission
FDTD	Finite-difference time-domain
FIB	Focused Ion Beam
FRAP	Fluorescence Recovery After Photobleaching
GalC	Galactocereborside
GPCR	G protein-coupled receptor
IgM	Immunoglobulin M
LOD	Limit of Detection
LSPR	Localized surface plasmon resonance
MS	Multiple Sclerosis
NBD	Nitrobenzoxadiazole
NHS	N-Hydroxysuccinimide
NIL	Nanoimprint Lithography
NSL	Nanosphere Lithography
NSOM	Near-field Scanning Optical Microscope
PDMS	Polydimethylsiloxane
PVD	Physical Vapor Deposition

Continued on next page

Table C.1 – continued from previous page

Acronym	Meaning
RIE	Reactive Ion etching
RIU	Refractive Index Unit
S/N	Signal to Noise
SAM	Self-Assembled Monolayer
SAPE	Streptavidin-R-Phycoerythrin
scFv	Single-Chain Antibody Fragment
SEM	Scanning Electron Microscope
SERS	Surface-Enhanced Raman Spectroscopy
SLB	Supported Lipid Bilayer
SP	Surface Plasmon
SPM	Scanning Probe Microscope
SPP	Surface Plasmon Polaritons
SPR	Surface Plasmon Resonance
SUL	Sulfatide
TERS	Tip-enhanced Raman spectroscopy